DEVELOPMENT OF A VERSATILE COMPUTATIONAL FLUID DYNAMICS-BASED MODEL FOR OPTIMIZATION AND IMPLEMENTATION OF VACUUM ULTRAVIOLET PHOTOREACTOR FOR DRINKING WATER TREATMENT

By

Gang SHI

English Engineering Education Program (e3) in Environmental Engineering

Graduate School of Engineering, Hokkaido University

A dissertation submitted in partial fulfillment of the requirements for the degree of Doctor of Philosophy

The Environmental Risk Engineering Laboratory, Division of Environmental Engineering, Graduate School of Engineering, Hokkaido University

September 2021

Acknowledgments

I would like to take this opportunity to thank many people who have offered invaluable assistance in the preparation of the dissertation.

For the achievements of my research and the past four years of my doctoral course, I would like to first and foremost express my sincere gratitude to my supervisor, Associate Prof. Taku MATSUSHITA, for his motivation, patience, and immense knowledge. His guidance helped me in all the time of research including the writing of this dissertation. His critical comments, constant encouragement, and guidance have greatly enlightened me on the academic pursuit. Without his consistent and illuminating instruction, this dissertation could not have reached its present stage. Besides my supervisor, I would like to thank Prof. Yoshihiko MATSUI who helped me a lot with his insightful comments, practical guide, and considerate encouragement throughout my doctoral course. Then, I would like to thank Associate Prof. Nobutaka SHIRASAKI, who is kind enough to give all the help he can offer and cultivate me to develop a good habit of being a researcher. I would like to mention that, every time before a public presentation, he was always kind to help me practice my presentation skills and analytical thinking ability when he was available. I also want to thank Prof. Naoki HIROYOSHI who attended the academic progress evaluation in my doctoral course and gave me many useful ideas and comments. What's more, I want to express my acknowledgment towards Prof. Satoshi OKABE, Prof. Katsuki KIMURA, and the rest of my dissertation committee not only for their advice, time, and patience but also for questions that incented me to widen my research from various perspectives.

Secondly, I appreciate Ms. Yuna KATO, Mr. Wataru SUGITA, Mr. Shota NISHIZAWA, Ms. Rinako KAWASHITA, and all the rest of the students in the laboratory, for their hard work together in the sleepless nights, for the valuable discussion we had, for all the fun we have had in the last years. Special thanks to Dr. Long PAN and Dr. Yoshifumi NAKAZAWA, who did not only help me to figure out my life when I came to Japan but also taught and fulfilled me with the necessary knowledge for experiments and basic knowledge working in this laboratory. Also, I thank the teachers, instructors, and engineers who instructed and cooperated with me when I used their facilities and software for research.

Third, I am grateful to my friends, Mr. Yize CHEN, Mr. Yuzhi FANG, Mr. Zihao GUAN, Mr.

Dali HUANG, Mr. Yuxiang HUANG, Mr. Jinming JIA, Dr. Long PAN, and Mr. Yuanjun ZHAO for their support for my research and daily life and they have helped me to overcome my weakness and the problem I met.

Priceless thanks are to my parents Mr. Aimin SHI and Mrs.Xiuyan ZHANG, as well as my other relatives, for all the assistance throughout my education journey.

In particular, I am grateful to the cooperation project between the China Scholarship Council (CSC, 201506010003) and the Japanese Government (Ministry of Education, Culture, Sports, Science and Technology, MEXT) Scholarship for the financial support of my doctoral course.

Abstract

To overcome the problem of organic micropollutants (OMPs) occurring in the drinking-water supply, additional purification processes especially advance oxidation processes (AOPs) have been applied to improve the conventional drinking-water-treatment processes. Vacuum ultraviolet (VUV) processes, a chemical-free AOP, have recently been found to be a promising technique for organic micropollutants removal in lab-scale research. In terms of implementation in the drinking-water-treatment plants, however, the lack of a proper simulation model for the VUV process is among the key factors hindering the implementation. Some computational models, predicting the behavior of organic micropollutants during the VUV processes, have been proposed. However, these models: 1) only assessed bicarbonate and natural organic matter (NOM) to the effects of water qualities, the other inorganic ions which are found ubiquitously in natural drinking-water sources have not been included; 2) only applied in specific reactors with limited conditions, the effects of design parameters and operating conditions have not been systematically analyzed. Overall none of them can take into account the actual water quality and simultaneously investigate the effects of operating conditions and design parameters systematically, which is exactly what must be solved in the VUV process implementation. This doctoral work attempted to fill the research vacancy: started by building a comprehensive kinetic model for different water qualities, then developing a computational fluid dynamics-based (CFD-based) model for operating conditions and design parameters analysis, finally based on the model work out a model-aid methodology for the VUV process implementation. To evaluate the performance of the VUV photoreactor in this research, the polar cyclic diether 1,4-dioxane, a typical OMP, was chosen as the target pollutant due to its ubiquitous presence, carcinogenicity, and refractoriness in the drinking-water-treatment process. According to the experimental results and CFD model simulations, some findings were concluded.

Firstly, a comprehensive kinetic model, which was set up by a series of ordinary differential equations about the rate of chemical and photochemical reactions, was developed to predict 1,4-dioxane degradation during the VUV process. Coexisting inorganic ions (i.e. carbonate/bicarbonate, chloride, and nitrate/nitrite) which are found ubiquitously in natural drinking water sources were found to have a great impact on the 1,4-dioxane degradation: the increase in these inorganic ion concentrations suppressed the degradation. The effects of these inorganic ions on the degradation were then incorporated into the kinetic model. The model was verified and validated in the 1,4-dioxane degradation in the batch mode experiments against

different water qualities. After introducing VUV and UV doses (determined by the chemical actinometry method) into the model, the kinetic model successfully predicted the 1,4-dioxane degradation in the flow-through photoreactor for contaminated groundwater. This result demonstrated that the kinetic model developed in the present research was able to predict the 1,4-dioxane degradation during the VUV process—whether in-situ or flow-through—and that the model could successfully describe the effects of inorganic ions in different raw waters on 1,4-dioxane degradation. For different water quality, the model could be simplified by sensitivity analysis to reduce the cost of computational resources.

Secondly, based on the kinetic model above, a novel CFD-based model that takes into account the effects of operating conditions (i.e. flow rate and radiation exitance) was developed for predicting 1,4-dioxane degradation during VUV treatment with flow-through photoreactors. To reduce the cost of computational resources, the kinetic model was simplified as a pseudo-first-order degradation reaction, whose reaction constant is determined in advance for the CFD-based model simulation and can be easily obtained by the kinetic model (or a simple batch mode experiment). After experimentally verified and validated the CFD-based model in a flow-through-type pilot-scale photoreactor, a virtual photoreactor was set up to precisely and systematically investigate the effects of the operating conditions on 1,4-dioxane degradation. Simulation results revealed that both increasing flow rate and decreasing radiant exitance increased the radiation efficiency (improved photoreactor performance), which agreed with the experimental results. Through EEO analysis based on these simulations, the following operations were finally recommended to be employed in actual drinking water treatment plants: VUV treatment using low-power lamps and a high flow rate was the most economical set-up. Specifically for the groundwater used in this research, treatment using high-power lamps at a high flow rate was suggested to be the most economical set-up under turbulent flow.

Thirdly, to investigate the effects of design parameters (i.e. reactor length, reactor gap, and baffles) on the performance of photoreactors, more experiment data were collected from three different flow-through photoreactors. After the CFD model was validated by the experimental data, virtual photoreactors with different design parameters were set up. Simulations in the virtual photoreactors showed that (1) both increasing reactor gap (the depth of the water path) and increasing radiant reactor length increased EEO (i.e. reduced the efficiency), and (2) performance was improved by introducing some baffles into the photoreactor under laminar flows, but was not so obvious under turbulent flows. Based on the simulation results, findings were concluded: 1) Operating under laminar flow is more economical for the small treatment plants. Short photoreactors with the thin reactor gap connected in series were recommended

(lowest EEO). Incorporating baffles is necessary in the case of using a long photoreactor. 2) Operating under turbulent flow is more economical for large treatment plants. VUV photoreactor with a thin reactor gap is recommended, and other design parameters do not significantly affect the cost-effectiveness under turbulent flow.

Overall the research, a CFD-based model for the optimization and implementation of VUV photoreactor for drinking-water treatment was developed. The model will according to the raw water quality and the treatment requirements, through a few necessary experiments and model simulations give the suitable design parameters and operating conditions for the full-scale VUV photoreactor. This model-aid methodology reduced the trial and error cost during the VUV photoreactor development from lab-scale to full-scale.

Table of Contents

List of Figures

List of Tables

Nomenclature

a, b, c, d	Generic stoichiometric coefficients of the generic species A, B, C, and D
C_A, C_B, C_C, C_D	The concentration of the generic species A, B, C, and D
C_0, C	Initial and concentration and instant concentration of the species
D	VUV dose
$\overline{D}$	Average VUV dose
h	Plank's constant, 6.626×10^{-34} J · s
I	Fluence rate
K	Conversion factor
k_x	Reaction rate constant
L	Lamp length
N_A	Avogadro's number
P	Electrical power of lamp or pump
p	Pressure
P_{VUV}	VUV power emitted from the sleeve
Q	Flowrate
r	Radial direction
$\vec{r}$	Position of vector
r_{in}, r_{out}	The inner and outer radius of the water path
r_{gap}	The radial distance of the water path, r_{out} - r_{in}
Re	Reynolds number
t	Time
$\vec{u}$	Fluid velocity vector
u_x	Fluid velocity (axial component)
$u(r)$	Fluid velocity as a function of r

Abbreviations

AOP	Advanced Oxidation Process
CFD	Computational Fluid Dynamics
DO	Dissolved oxygen
EDC	Endocrine-disrupting Chemicals
EEO	Electrical Energy per Order

OMP	Organic Micro-pollutant
PPCP	Pharmaceutical and Personal Care Product
RTE	Radiative Transport Equation
UV	Ultraviolet
VUV	Vacuum Ultraviolet

Greek letters

α_λ	The absorption coefficient of the solution at a specified wavelength λ
$\Delta C_{A,k_x}$	The relative error in predicting the scalar C_A when the reaction k_x is omitted from the kinetic model
$\varepsilon_{A,\lambda}$	The molar absorption coefficient for the generic species A at a given wavelength λ
ε	Turbulent dissipation rate
κ	Turbulent kinetic energy
λ	Wavelength
μ	Dynamic viscosity
ρ	Density
ν	Kinematic viscosity
Φ	Quantum yield

Chapter 1. Introduction

1.1 Background

1.1.1 Organic micro-pollutants removal to drinking-water-treatment

Over the past few decades, many emerging organic micro-pollutants (OMPs) including pesticides, pharmaceutical and personal care products (PPCPs), and endocrine-disrupting chemicals (EDCs) have frequently been detected in the aquatic environment. Although the occurrence of OMPs is usually in a very low concentration range (from $ng \cdot L^{-1}$ to $\mu g \cdot L^{-1}$), the emission and accumulation of these anthropogenic pollutants in nature is a potential threat to human health (Li et al., 2020; Wu et al., 2019; Xu et al., 2019) and the aquatic environment (Jeirani et al., 2017; Jiang et al., 2013).

For the drinking-water supply, however, conventional drinking-water-treatment processes (i.e. coagulation, sedimentation, and sand filtration) are generally ineffective in removing some of the OMPs presented in source water (McCleaf et al., 2017; McGuire et al., 1978; Stackelberg et al., 2007; Ternes et al., 2002; Tröger et al., 2018), and indeed some drinking-water-treatment plants in Japan and the United States have been forced to close because their water sources were contaminated with OMPs (Weimar, 1980). Therefore, an additional purification process is needed to enhance OMPs removal from conventional drinking-water-treatment processes.

Techniques such as ozonation (Adams et al., 1994; Ormad et al., 2008), activated carbon (Kim and Kang, 2008; Pan et al., 2016; Piai et al., 2019), and membrane filtration (Košutić et al., 2005; Sarkar et al., 2007) have been installed at drinking-water-treatment plants around the world to enhance OMPs removal. However, these techniques suffer from their limitation in removing OMPs. The ozonation processes, while effective at removing a range of OMPs, often produce toxic transformation products (TPs) (Benner and Ternes, 2009; Dodd et al., 2010; Mcdowell et al., 2005) and cannot remove some of the resistant OMPs (e.g. 1,4-dioxane, Adams et al., 1994). Activated carbon, while effective at removing hydrophobic OMPs, is less effective for hydrophilic OMPs (Pan et al., 2017). Membrane-based technologies, e.g. nanofiltration and reverse osmosis, have proven to be non-selective, no TPs production, and efficient in all kinds of OMPs removal, still be problematic because of the high concentration of OMPs in the

retentate that has to be treated before discharge (Nicolaisen, 2003; Radjenović et al., 2008; Sarkar et al., 2007). Overall, these limitations increase the cost of investment, operational, and energy of these enhanced techniques.

Advanced oxidation processes (AOPs), widely recognized as a highly efficient treatment, are proved to be a feasible option for OMPs removal (Matilainen and Sillanpää, 2010). AOPs are based on the in situ generations of strong oxidants for the oxidation of organic compounds. The hydroxyl radical (OH radical), known to be a powerful oxidant (oxidation potential 2.80 eV) that constitute the majority of available AOPs, reacts with the organic species non-selectively and very quickly with a reaction rate constant in the range of 10^8-10^{10} L·mol·s^{-1} (Buxton et al., 1988).

Various AOPs techniques have been investigated for OMPs removals such as O_3/H_2O_2 (Suh and Mohseni, 2004), UV/TiO_2 (Coleman et al., 2007; Hill et al., 1997), and UV/H_2O_2 (Matsushita et al., 2015). Among these techniques, full-scale applications of UV/H_2O_2 for OMPs removal have already been established for potable water reuse (Audenaert et al., 2011) and surface water treatment (Kruithof et al., 2007). The UV/H_2O_2 process, compared with the enhanced OMPs removal techniques discussed above, achieved better cost-effective results in OMPs removal (Miklos et al., 2018). However, the UV/H_2O_2 process suffers from the relatively high costs of H_2O_2 and the removal of unreacted H_2O_2 at the end of the treatment process (Cuerda-Correa et al., 2020). Moreover, for the remoteness in which small and rural communities are often located, the transportation and storing of large quantities of chemicals become a logistic challenge. Therefore, the chemical-free AOP, which is considered to be able to significantly reduce the overall cost of operation, is required to be implemented.

1.1.2 Vacuum ultraviolet for organic micro-pollutants degradation

In recent years, the vacuum ultraviolet (VUV) process has emerged as a strong candidate to fulfill the role of UV/ H_2O_2 in small drinking-water-treatment systems (Zoschke et al., 2014). The VUV radiation covers the wavelength range from 100 to 200 nm. The most common sources for VUV radiation are the low-pressure mercury-vapor lamp (Zoschke et al., 2014), whose emission spectrum is concentrated at 254 nm (UV) and 185 nm (VUV). The 185 nm photons are strongly absorbed by water with a high absorption coefficient of 1.8 cm^{-1} (Weeks et al., 1963). As a consequence of the absorption, the homolysis (Eq. 1-1) and photochemical

ionization (Eq. 1-2) of water molecules take place (Gonzalez et al., 2004) and strong oxidants OH radicals formed:

$$H_2O \xrightarrow{hv\ 185\ nm} \cdot OH + \cdot H \qquad \Phi_1 = 0.33 \tag{1-1}$$

$$H_2O \xrightarrow{hv\ 185\ nm} \cdot OH + H^+ + e^-_{aq} \qquad \Phi_2 = 0.045 \tag{1-2}$$

Due to the direct generation of OH radicals, the VUV process is considered to be AOP, and the generation rate of OH radicals is comparable to other AOPs (Legrini et al., 1993). The VUV process does not use chemical additives to generate OH radicals and is therefore considered to be a promising economical approach for OMPs removal (Imoberdorf and Mohseni, 2012; Xie et al., 2018). Indeed, laboratory-scale research has indicated that the VUV process followed by activated carbon treatment was an economical means of removing OMPs from water without inducing the formation of by-products from coexisting natural organic matter (Matsushita et al., 2015).

1.1.3 Implementation limitations of vacuum ultraviolet process

Despite the advantages of the VUV technique and the promising results obtained through lab-scale studies, however, the implementation of the VUV technique for real-world drinking-water treatment is somehow stymied. For implementing a treatment technique into a full-scale plant, the step of the traditional and entirely empirical methodology is: (1) Conducting experiments mimicking the full-scale plant in the lab-scale reactor to investigate the optimum operating conditions. (2) Scaling up the lab-scale reactor step-by-step to, and then design the full-scale plants based on the results obtained during the scale-up process. This methodology of using a lab-scale reactor has the advantages of not requiring a large amount of water, easy to control and optimize operating conditions, and low cost compared with direct full-scale experiments, as a result, it has already been applied successfully for many treatment techniques (Abu Hasan et al., 2020; Demirel et al., 2005; Deng and Englehardt, 2006).

However, this methodology cannot be effectively applied to the VUV process implementation because there are some special issues for the VUV process in each step of the above methodology. For step (1), the performance of the VUV photoreactor is highly affected by the water quality (Imoberdorf and Mohseni, 2012), which suggests that the lab-scale experiments need to be conducted with the same raw water as the full-scale plant. Moreover, seasonal

variation in the raw water quality should also be taken into consideration for this reason. These complications would reduce the superiority of the lab-scale experiments. For step (2), the scaling up for photoreactors is time-consuming and expensive (Alfano and Cassano, 2009) because the performance of VUV treatment and its influencing factors (e.g. hydrodynamics, incident radiation, optical depth, etc.) are more sensitive to the design parameters than other chemical reactors.

A successful simulation model, predicting the behavior of OMPs during the VUV process which takes into account the effects of water quality, operating condition, and design parameters, can contribute to solving the problem of implementation and obtaining the full benefit of the VUV process. However, the research on the VUV model is insufficient, and hence the lack of a proper simulation model becomes the key factor hindering the implementation (Bagheri and Mohseni, 2015, 2017).

1.1.4 Computational fluid dynamics-based model for optimization and implementation of the vacuum ultraviolet process

It is a tough task to build a simulation model for the VUV process due to the multiphysics nature inside the photoreactor. For the photoreactor used in water treatment, the simulation model should allow for the effects of fluid movement and mixing (hydrodynamics), the distribution of radiant energy (radiation field), the rate of deterioration of the chemical species (kinetic), and the interaction of these phenomena with one another (Siamak and Fariborz, 2010). A mathematical methodology, which consists of a series of differential equations that govern various phenomena in the photoreactor, can contribute to simulating the behavior of OMPs during the VUV process. Although the analytical solutions to these equations do not exist due to the complexity of the photoreactor geometry and interaction of the phenomena above, the practical approach of numerical solution can be obtained by relevant techniques such as computational fluid dynamics (CFD) (Boyjoo et al., 2013).

CFD has shown great potential as a powerful and cost-efficient tool for UV/H_2O_2 photoreactor analysis (Wols et al., 2015; Zhang et al., 2014). CFD models have been already developed for investigating the effects of operating conditions (Alpert et al., 2010; Santoro et al., 2010) and design parameters (Ghafoori et al., 2014; Mohajerani et al., 2010), which have led to improvements in the UV/H_2O_2 system implementation. Compared with UV/H_2O_2 processes,

however, modeling for the VUV process is much more difficult due to the following differences:

1) The penetration distance of VUV in water is much shorter than UV (Crapulli et al., 2014; Zoschke et al., 2014) because the absorption coefficient of pure water at VUV (1.8 cm^{-1} at 185 nm) is much greater than that at UV (less than 0.001 cm^{-1} at 254 nm). For the aqueous solutions, the penetration distances are further shortened because of the presence of ions absorbing VUV photons, such as chloride and carbonate/bicarbonate (Weeks et al., 1963). Therefore, in an annular photoreactor that is the most commonly used configuration, there is a particular mismatch (**Fig.1**) between the reactor gap (an inner gap where water resides) and the VUV penetration layer (99% VUV photons are absorbed within this layer). Taking into account the diffusion coefficient of OH radicals and its average lifetime in water, which is about 2.3×10^{-5} $cm^2\cdot s^{-1}$ (Buxton et al., 1988) and 7.7 ns to 7.7 μs (LaVerne, 1989), OH radicals are expected to react immediately at where it is generated. Therefore, the degradation of OMPs is supposed to take place mainly in the VUV penetration layer. The heterogeneity between the irradiated volume (in the penetration layer) and the non-irradiated (received a negligible amount of irradiation) volume of the water increase the difficulties of integrating the hydrodynamics, radiation field, and kinetic.

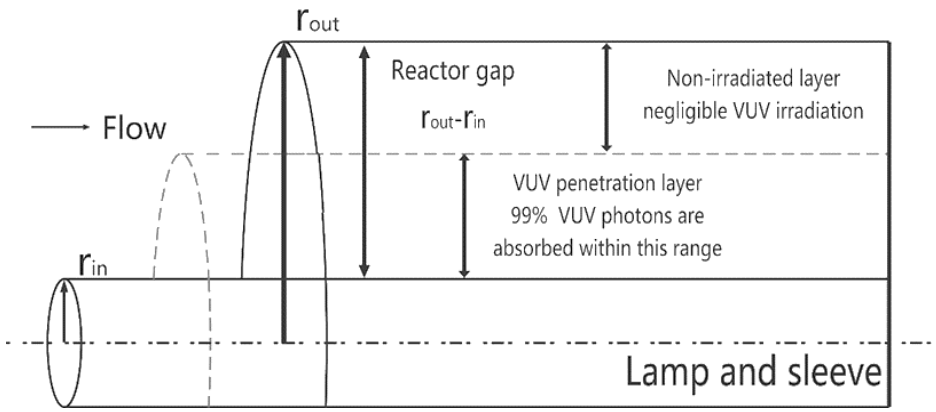

Fig. 1-1The mismatch between reactor gap and VUV radiation penetration

2) The photochemical reaction mechanism of the VUV process is more complex compared with the UV/H_2O_2 process (Bagheri and Mohseni, 2014). The VUV process and UV/H_2O_2 process generate OH radicals in different ways (Gonzalez et al., 2004; Imoberdorf and Mohseni, 2012). The generation of OH radicals in the VUV process relies on the photolysis of water at 185 nm (Eq. 1-1 and 1-2). In contrast, H_2O_2 photolysis at 254 nm (Eq. 1-3) is the predominant reaction for OH radical generation in the UV/H_2O_2 process.

$$H_2O_2 \xrightarrow{h\nu\ 254\ nm} 2\cdot OH \qquad \Phi_3 = 0.5 \tag{1-3}$$

Besides, several inorganic anions, such as chloride, are known to strongly absorb 185 nm photons due to charge-transfer-to-solvent absorption bands (Fox and Hayon, 1979; Hayon, 1967; Jortner, 1964).

$$Cl^- \xrightarrow{h\nu\ 185\ nm} \cdot Cl + e_{aq}^- \tag{1-4}$$

The formation of hydrogen radical (H radical), solvated electron (e_{aq}^-), chlorine radicals, etc. introduce a more complex radical reaction scheme for VUV processes compared with UV/H_2O_2 processes, which merely produce OH radicals.

Based on the two difficulties above, the number of models developed for the VUV processes is limited. Imoberdorf and Mohseni (2012) developed a kinetic model that investigated the effect of alkalinity and natural organic matter (NOM) on the OMPs degradation. This model took into account the propagation and absorption of radiative energy in the photoreactor, generation of hydroxyl radicals via water photolysis, and interaction between photogenerated radicals and OMPs. Xie et al. (2018) developed a simple kinetic model to describe the degradation of OMPs during the VUV process, by taking the OH radical scavenging effects of formed organic intermediates as co-existing organic matter in whole. Effects of humic acid (HA), alkalinity, and chloride on the oxidation efficiency were investigated by the model. However, there is a drawback of the models above that both of them were based on the experiments conducted in a specific cyclic mode photoreactor and cannot be applied to the photoreactors with different operating conditions and design parameters. Crapulli et al. (2014) developed a CFD-based model that assesses the role of the transport mechanism and species distributions within photoreactor, and the distribution of OH radicals in the photoreactors was investigated. Bagheri and Mohseni (2014, 2015, 2017) developed the CFD-based models that predicted the behavior of OMPs in the photoreactor during the VUV process. The operating conditions and design parameters, such as flow rate and hydraulic radius, etc. were unsystematically investigated by comparing serval specific cases. These CFD-based models (Bagheri and Mohseni, 2014, 2015, 2017; Crapulli et al., 2014) took into account bicarbonate and NOM alone in terms of the effects of water qualities, other influential ions, such as chloride and nitrate which are ubiquitous in natural waters and have significant impacts on the performance of VUV photoreactor (Furatian and Mohseni, 2018; Mack and Bolton, 1999), were not involved in the models. Therefore, their CFD-based models are not accurate when applied to actual contaminated water. Overall, none of them can take into account the actual water quality, and simultaneously investigate the effects

of operating conditions and design parameters systematically, which is precisely what must be solved in the VUV process implementation for drinking-water treatment.

1.2 Objectives and components of this research

This doctoral work attempted to fill in this research vacancy: started by building a comprehensive kinetic model for different water qualities, then developing a computational fluid dynamics-based (CFD-based) model for operating conditions and design parameters analysis, finally based on the model work out a model-aid methodology for the VUV process implementation.

1.2.1 Target pollutant in this research

To evaluate the performance of the VUV photoreactor in this research, the polar cyclic diether 1,4-dioxane was chosen as the target pollutant due to its ubiquitous presence (Stepien et al., 2014), carcinogenicity (European Communities, 2004), and refractoriness in the drinking-water-treatment process (Adams et al., 1994; McGuire et al., 1978).

1,4-Dioxane has many uses in commercial processes (European Communities, 2004; Mohr et al., 2020), and it is found in a wide range of consumer products (e.g. detergents, shampoos, and cosmetics) as a by-product of polyester synthesis (Zenker et al., 2003). After being released into natural waters, 1,4-dioxane, which is little adsorbed by sediments ($\log_{10} K_{ow} = -0.27$; Dietz and Schnoor, 2001), eventually contaminates groundwater through recharge with contaminated surface water (Stepien et al., 2014). 1,4-dioxane was first found as a groundwater contaminant in the United States nearly four decades ago (Kraybill, 1978), and the occurrence in groundwater has been well-documented in many studies (Burmaster, 1982; European Communities, 2004; Isaacson et al., 2006; Lesage et al., 1990). Extensive research on the distribution and occurrence of 1,4-dioxane has been carried out in Japan. Studies confirmed the presence of 1,4-dioxane in landfill leachate, effluents from sewage plants, surface, and groundwater (Abe, 1999; Kawata and Tanabe, 2009; Yasuhara et al., 2003).

Toxicological studies have revealed that 1,4-dioxane is a possible carcinogen, suggesting that using contaminated surface waters and groundwater as sources of drinking water may increase

the risk of cancer in end-users (European Communities, 2004; USEPA, 2013). The World Health Organization (WHO) suggested a 50 $\mu g \cdot L^{-1}$ threshold value for 1,4-dioxane in drinking-water (WHO, 2005), the Ministry of the Health, Labour and Welfare of Japan added the threshold value to water quality standard in 2003 (Ministry of the Health Labour and Welfare of Japan, 2003), and the USEPA proposed a health-based advisory level of 3.5 $\mu g \cdot L^{-1}$ in tap water (USEPA, 2013).

1.2.2 Outline of this research

According to all the above, the ultimate goal of this research was to work out a model-aid methodology for design and optimize the VUV photoreactor according to the actual requirement. To achieve this, the following steps were undertaken and discussed in the following chapters:

- In Chapter 1, a literature review was presented. The risk and recalcitrance of OMPs in conventional drinking-water-treatment processes were summarized. The chemical-free VUV process considered to be a promising AOPs technique was discussed. The limitation of the VUV process's practical implementation and a feasible solution of the CFD-based model were reviewed. Information of the target pollutant used in the present research, i.e. 1,4-dioxane, was summarized.

- In Chapter 2, a kinetic model that taking into account the effect of water quality was developed for 1,4-dioxane degradation during the VUV process. The influential inorganic ions, which were not included in the CFD-based models in the previous researches, were identified and investigated by the experiments conducted in a flow-through photoreactor. The effects of the influential inorganic ions on degradation were then incorporated into the kinetic model by a series of ordinary differential equations. Batch mode experiments with different water samples were conducted in a quasi-collimated beam photoreactor to verify and validate the kinetic model. The VUV and UV doses, determined by the chemical actinometry method in a flow-through photoreactor, were imported into the kinetic model to test whether it can be used as the basis for the Lagrangian particle-tracking approach in the subsequent chapter. For the certain water quality, to reduce the cost of computational resources in subsequent CFD calculations, unimportant reactions determined by sensitivity analysis could be eliminated from the kinetic model.

- In Chapter 3, based on the kinetic model above, a novel CFD-based model taking into account the effects of operating conditions (i.e. flow rate and radiation exitance) was developed for predicting 1,4-dioxane degradation during VUV treatment with flow-through photoreactors. The concentration of 1,4-dioxane was calculated by the Lagrangian particle-tracking approach. The CFD-based model in a flow-through pilot-scale photoreactor was experimentally verified and validated. A virtual photoreactor, built by the validated CFD-based model, was set up to systematically investigate the effects of the operating conditions on the degradation performance. General solutions for operating condition optimization that contribute to the practical implementation of the VUV process were then proposed.

- In Chapter 4, the effects of photoreactor design parameters on 1,4-dioxane degradation performance were investigated. Experimental data, collected from three types of flow-through photoreactors with different design parameters, were used to verify and validate the CFD-based model. Virtual photoreactors with different design parameters were set up by the validated CFD-based model. Simulations of 1,4-degradation in these virtual photoreactors were carried out, and the results were discussed. A model-aid methodology of design and optimize the VUV photoreactor according to the actual requirement was proposed, especially for 1,4-dioxane, the target OMP throughout this dissertation.

- In Chapter 5, the findings and conclusions of each previous chapter were summarized, and recommendations for the future work of this research were suggested.

1.3 References

Abe, A., 1999. Distribution of 1,4-dioxane in relation to possible sources in the water environment. Science of the Total Environment 227, 41–47.

Abu Hasan, H., Muhammad, M.H., Ismail, N.I., 2020. A review of biological drinking water treatment technologies for contaminants removal from polluted water resources. Journal of Water Process Engineering 33, 101035.

Adams, C.D., Scanlan, P.A., Secrist, N.D., 1994. Oxidation and biodegradability enhancement of 1, 4-dioxane using hydrogen peroxide and ozone. Environmental science & technology 28, 1812–1818.

1.3 References

Alpert, S.M., Knappe, D.R.U., Ducoste, J.J., 2010. Modeling the UV/hydrogen peroxide advanced oxidation process using computational fluid dynamics. Water Research 44, 1797–1808.

Audenaert, W.T.M., Vermeersch, Y., Van Hulle, S.W.H., Dejans, P., Dumoulin, A., Nopens, I., 2011. Application of a mechanistic UV/hydrogen peroxide model at full-scale: Sensitivity analysis, calibration and performance evaluation. Chemical Engineering Journal 171, 113–126.

Bagheri, M., Mohseni, M., 2017. Pilot-scale treatment of 1,4-dioxane contaminated waters using 185 nm radiation: Experimental and CFD modeling. Journal of Water Process Engineering 19, 185–192.

Bagheri, M., Mohseni, M., 2015. A study of enhanced performance of VUV/UV process for the degradation of micropollutants from contaminated water. Journal of Hazardous Materials 294, 1–8.

Bagheri, M., Mohseni, M., 2014. Computational fluid dynamics (CFD) modeling of VUV/UV photoreactors for water treatment. Chemical Engineering Journal 256, 51–60.

Benner, J., Ternes, T.A., 2009. Ozonation of metoprolol: Elucidation of oxidation pathways and major oxidation products. Environmental Science and Technology 43, 5472–5480.

Boyjoo, Y., Ang, M., Pareek, V., 2013. Some aspects of photocatalytic reactor modeling using computational fluid dynamics. Chemical Engineering Science 101, 764–784.

Burmaster, D.E., 1982. The New Pollution. Environment: Science and Policy for Sustainable Development 24, 6–36.

Buxton, G. V., Greenstock, C.L., Helman, W.P., Ross, A.B., 1988. Critical Review of rate constants for reactions of hydrated electrons, hydrogen atoms and hydroxyl radicals (·OH/·O− in Aqueous Solution. Journal of Physical and Chemical Reference Data 17, 513–886.

Coleman, H.M., Vimonses, V., Leslie, G., Amal, R., 2007. Degradation of 1,4-dioxane in water using TiO2 based photocatalytic and H2O2/UV processes. Journal of Hazardous Materials 146, 496–501.

Crapulli, F., Santoro, D., Sasges, M.R., Ray, A.K., 2014. Mechanistic modeling of vacuum UV advanced oxidation process in an annular photoreactor. Water Research 64, 209–225.

Cuerda-Correa, E.M., Alexandre-Franco, M.F., Fernández-González, C., 2020. Advanced oxidation processes for the removal of antibiotics from water. An overview. Water (Switzerland) 12.

Demirel, B., Yenigun, O., Onay, T.T., 2005. Anaerobic treatment of dairy wastewaters: A review. Process Biochemistry 40, 2583–2595.

Deng, Y., Englehardt, J.D., 2006. Treatment of landfill leachate by the Fenton process. Water

Research 40, 3683–3694.

Dietz, A.C., Schnoor, J.L., 2001. Advances in Phytoremediation. Environmental Health Perspectives 109, 163–168.

Dodd, M.C., Rentsch, D., Singer, H.P., Kohler, H.P.E., Gunten, U. Von, 2010. Transformation of β-Lactam antibacterial agents during aqueous ozonation: Reaction pathways and quantitative bioassay of biologically-active oxidation products. Environmental Science and Technology 44, 5940–5948.

European Communities, 2004. European Union Risk Assessment Report, Alkanes, C.

Fox, M.F., Hayon, E., 1979. Far-ultraviolet solution spectroscopy of hydrosulphide ion. Journal of the Chemical Society, Faraday Transactions 1: Physical Chemistry in Condensed Phases 75, 1380–1389.

Furatian, L., Mohseni, M., 2018. Influence of chloride on the 185 nm advanced oxidation process. Chemosphere 199, 263–268.

Ghafoori, S., Mehrvar, M., Chan, P.K., 2014. Photoreactor scale-up for degradation of aqueous poly(vinyl alcohol) using UV/H2O2 process. Chemical Engineering Journal 245, 133–142.

Gonzalez, M.G., Oliveros, E., Wörner, M., Braun, A.M., 2004. Vacuum-ultraviolet photolysis of aqueous reaction systems. Journal of Photochemistry and Photobiology C: Photochemistry Reviews 5, 225–246.

Hayon, E., 1967. Flash photolysis in the vacuum ultraviolet region of so42- CO32- and OH- ions in aqueous solutions. Journal of Physical Chemistry 71, 1472–1477.

Hill, R.R., Jeffs, G.E., Roberts, D.R., 1997. Photocatalytic degradation of 1,4-dioxane in aqueous solution. Journal of Photochemistry and Photobiology A: Chemistry 108, 55–58.

Imoberdorf, G., Mohseni, M., 2012. Kinetic study and modeling of the vacuum-UV photoinduced degradation of 2,4-D. Chemical Engineering Journal 187, 114–122.

Isaacson, C., Mohr, T.K.G., Field, J.A., 2006. Quantitative determination of 1,4-dioxane and tetrahydrofuran in groundwater by solid-phase extraction GC/MS/MS. Environmental Science and Technology 40, 7305–7311.

Jeirani, Z., Niu, C.H., Soltan, J., 2017. Adsorption of emerging pollutants on activated carbon. Reviews in Chemical Engineering 33, 491–522.

Jiang, J.Q., Zhou, Z., Sharma, V.K., 2013. Occurrence, transportation, monitoring and treatment of emerging micro-pollutants in wastewater - A review from global views. Microchemical Journal 110, 292–300.

Jortner, J., 1964. On the photochemistry of aqueous solutions of chloride, bromide, and iodide ions. Journal of Physical Chemistry 68, 247–255.

Kawata, K., Tanabe, A., 2009. Distribution and variation of 1,4-dioxane in water from rivers in Niigata including the Shinano River. Bulletin of Environmental Contamination and

Toxicology 82, 673–677.

Kim, J., Kang, B., 2008. DBPs removal in GAC filter-adsorber. Water Research 42, 145–152.

Košutić, K., Furač, L., Sipos, L., Kunst, B., 2005. Removal of arsenic and pesticides from drinking water by nanofiltration membranes. Separation and Purification Technology 42, 137–144.

Kraybill, H.F., 1978. Carcinogenesis induced by trace contaminants in potable water. Bulletin of the New York Academy of Medicine 54, 413–27.

Kruithof, J.C., Kamp, P.C., Martijn, B.J., 2007. UV/H2O2 Treatment: A Practical Solution for Organic Contaminant Control and Primary Disinfection. Ozone: Science & Engineering 29, 273–280.

LaVerne, J.A., 1989. The production of OH radicals in the radiolysis of water with 4He ions. Radiation Research 118, 201–210.

Lesage, S., Jackson, R.E., Priddle, M.W., Riemann, P.G., 1990. Occurrence and Fate of Organic Solvent Residues in Anoxic Groundwater at the Gloucester Landfill, Canada. Environmental Science and Technology 24, 559–566.

Li, X., Tian, T., Shang, X., Zhang, R., Xie, H., Wang, X., Wang, H., Xie, Q., Chen, J., Kadokami, K., 2020. Occurrence and health risks of organic micro-pollutants and metals in groundwater of chinese rural areas. Environmental Health Perspectives 128, 1–16.

Mack, J., Bolton, J.R., 1999. Photochemistry of nitrite and nitrate in aqueous solution: A review. Journal of Photochemistry and Photobiology A: Chemistry 128, 1–13.

Matilainen, A., Sillanpää, M., 2010. Removal of natural organic matter from drinking water by advanced oxidation processes. Chemosphere 80, 351–365.

Matsushita, T., Hirai, S., Ishikawa, T., Matsui, Y., Shirasaki, N., 2015. Decomposition of 1,4-dioxane by vacuum ultraviolet irradiation: Study of economic feasibility and by-product formation. Process Safety and Environmental Protection 94, 528–541.

McCleaf, P., Englund, S., Östlund, A., Lindegren, K., Wiberg, K., Ahrens, L., 2017. Removal efficiency of multiple poly- and perfluoroalkyl substances (PFASs) in drinking water using granular activated carbon (GAC) and anion exchange (AE) column tests. Water Research 120, 77–87.

Mcdowell, D.C., Huber, M.M., Wagner, M., Von Gunten, U., Ternes, T.A., 2005. Ozonation of carbamazepine in drinking water: Identification and kinetic study of major oxidation products. Environmental Science and Technology 39, 8014–8022.

McGuire, M.J., Suffet, I.H., Radziul, J. V, 1978. Assessment of Unit Processes for the Removal of Trace Organic Compounds From Drinking Water. Journal - American Water Works Association 70, 565–572.

Miklos, D.B., Remy, C., Jekel, M., Linden, K.G., Drewes, J.E., Hübner, U., 2018. Evaluation

of advanced oxidation processes for water and wastewater treatment – A critical review. Water Research 139, 118–131.

Ministry of the Health Labour and Welfare of Japan, 2003. System relating to water quality standards (2003) [WWW Document]. URL https://www.mhlw.go.jp/topics/bukyoku/kenkou/suido/kijun/seido.html

Mohajerani, M., Mehrvar, M., Ein-Mozaffari, F., 2010. CFD modeling of metronidazole degradation in water by the UV/H 2O2 process in single and multilamp photoreactors. Industrial and Engineering Chemistry Research 49, 5367–5382.

Mohr, T.K.G., DiGuiseppi, W.H., Hatton, J.W., Anderson, J.K., 2020. Environmental investigation and remediation: 1, 4-dioxane and other solvent stabilizers. CRC Press.

Nicolaisen, B., 2003. Developments in membrane technology for water treatment. Desalination 153, 355–360.

Ormad, M.P., Miguel, N., Claver, A., Matesanz, J.M., Ovelleiro, J.L., 2008. Pesticides removal in the process of drinking water production. Chemosphere 71, 97–106.

Pan, L., Matsui, Y., Matsushita, T., Shirasaki, N., 2016. Superiority of wet-milled over dry-milled superfine powdered activated carbon for adsorptive 2-methylisoborneol removal. Water Research 102, 516–523.

Pan, L., Nishimura, Y., Takaesu, H., Matsui, Y., Matsushita, T., Shirasaki, N., 2017. Effects of decreasing activated carbon particle diameter from 30 Mm to 140 nm on equilibrium adsorption capacity. Water Research 124, 425–434.

Piai, L., Dykstra, J.E., Adishakti, M.G., Blokland, M., Langenhoff, A.A.M., van der Wal, A., 2019. Diffusion of hydrophilic organic micropollutants in granular activated carbon with different pore sizes. Water Research 162, 518–527.

Radjenović, J., Petrović, M., Ventura, F., Barceló, D., 2008. Rejection of pharmaceuticals in nanofiltration and reverse osmosis membrane drinking water treatment. Water Research 42, 3601–3610.

Santoro, D., Raisee, M., Moghaddami, M., Ducoste, J., Sasges, M., Liberti, L., Notarnicola, M., 2010. Modeling hydroxyl radical distribution and trialkyl phosphates oxidation in UV - H2O2 photoreactors using computational fluid dynamics. Environmental Science and Technology 44, 6233–6241.

Sarkar, B., Venkateswralu, N., Rao, R.N., Bhattacharjee, C., Kale, V., 2007. Treatment of pesticide contaminated surface water for production of potable water by a coagulation-adsorption-nanofiltration approach. Desalination 212, 129–140.

Siamak, E., Fariborz, T., 2010. Simulation of UV photoreactor for degradation of chemical contaminants: Model development and evaluation. Environmental Science and Technology 44, 2056–2063.

1.3 References

Stackelberg, P.E., Gibs, J., Furlong, E.T., Meyer, M.T., Zaugg, S.D., Lippincott, R.L., 2007. Efficiency of conventional drinking-water-treatment processes in removal of pharmaceuticals and other organic compounds. Science of the Total Environment 377, 255–272.

Stepien, D.K., Diehl, P., Helm, J., Thoms, A., Püttmann, W., 2014. Fate of 1,4-dioxane in the aquatic environment: From sewage to drinking water. Water Research 48, 406–419.

Suh, J.H., Mohseni, M., 2004. A study on the relationship between biodegradability enhancement and oxidation of 1,4-dioxane using ozone and hydrogen peroxide. Water Research 38, 2596–2604.

Ternes, T.A., Meisenheimer, M., McDowell, D., Sacher, F., Brauch, H.J., Haist-Gulde, B., Preuss, G., Wilme, U., Zulei-Seibert, N., 2002. Removal of pharmaceuticals during drinking water treatment. Environmental Science and Technology 36, 3855–3863.

Tröger, R., Klöckner, P., Ahrens, L., Wiberg, K., 2018. Micropollutants in drinking water from source to tap - Method development and application of a multiresidue screening method. Science of the Total Environment 627, 1404–1432.

USEPA, 2013. Summary on 1,4-Dioxane (123-91-1) 1–16.

Weeks, J.L., Meaburn, G.M., Gordon, S., 1963. Absorption coefficients of liquid water and aqueous solutions in the far ultraviolet. Radiation research 19, 559–567.

Weimar, R., 1980. Prevent groundwater contamination before it's too late. Water & Waste Engineering 17, 30–33.

WHO, 2005. 1,4-Dioxane in Drinking-water.Background document for preparation of WHO Guidelines for drinking-water quality.

Wols, B.A., Harmsen, D.J.H., van Remmen, T., Beerendonk, E.F., Hofman-Caris, C.H.M., 2015. Design aspects of UV/H2O2 reactors. Chemical Engineering Science 137, 712–721.

Wu, D., Zhou, Y., Lu, G., Hu, K., Yao, J., Shen, X., Wei, L., 2019. The occurrence and risks of selected emerging pollutants in drinking water source areas in Henan, China. International Journal of Environmental Research and Public Health 16.

Xie, P., Yue, S., Ding, J., Wan, Y., Li, X., Ma, J., Wang, Z., 2018. Degradation of organic pollutants by Vacuum-Ultraviolet (VUV): Kinetic model and efficiency. Water Research 133, 69–78.

Xu, S., Zhou, S., Xing, L., Shi, P., Shi, W., Zhou, Q., Pan, Y., Song, M.Y., Li, A., 2019. Fate of organic micropollutants and their biological effects in a drinking water source treated by a field-scale constructed wetland. Science of the Total Environment 682, 756–764.

Yasuhara, A., Tanaka, Y., Tanabe, A., Kawata, K., Katami, T., 2003. Elution of 1,4-dioxane from waste landfill sites. Bulletin of Environmental Contamination and Toxicology 71, 641–647.

Zenker, M.J., Borden, R.C., Barlaz, M.A., 2003. Occurrence and Treatment of 1,4-Dioxane in Aqueous Environments. Environmental Engineering Science 20, 423–432.

Zhang, J., Tejada-Martínez, A.E., Zhang, Q., 2014. Developments in computational fluid dynamics-based modeling for disinfection technologies over the last two decades: A review. Environmental Modelling and Software 58, 71–85.

Zoschke, K., Börnick, H., Worch, E., 2014. Vacuum-UV radiation at 185nm in water treatment - A review. Water Research 52, 131–145.

Chapter 2. Kinetic modeling for the VUV process

2.1 Chapter introduction

As discussed in **Chapter 1**, this dissertation aims to develop a CFD-based simulation model involving water quality, operating conditions (i.e. flow rate and radiation exitance), and design parameters (i.e. length, reactor gap, and baffles) for the VUV process to facilitate its implementation to the drinking-water treatment. To involve all the parameters above, the model should allow for the effects of hydrodynamics, radiation field, kinetic, and the interaction of these phenomena with one another (Siamak and Fariborz, 2010). The Lagrangian approach, calculating the chemical species' concentrations along the track-lines of individual fluid elements, can be used to integrate these phenomena above and simulate the photochemical process in the photoreactor (Wols and Hofman-Caris, 2012a). The first yet important step for the Lagrangian approach is to build a comprehensive in-situ kinetic model for the individual particles.

CFD-based models using the Lagrangian approach to predict the behavior of OMPs during VUV treatment have been proposed (Bagheri and Mohseni, 2014, 2015, 2017; Crapulli et al., 2014). However, the kinetic model of their CFD models has taken into account only bicarbonate and natural organic matter (NOM) to assess the effects of water qualities. Other influential species, mainly inorganic ions, such as chloride and nitrate that are ubiquitous in natural waters and have significant impacts on the performance of the VUV photoreactor (Furatian and Mohseni, 2018; Mack and Bolton, 1999), were not involved in their models. Therefore, their CFD-based models are not accurate when applied to actual contaminated water. To the author's knowledge, no CFD-based model using the Lagrangian approach that takes into account the effect of chloride and nitrate on kinetic has been reported.

The main objective of this chapter was to develop a versatile kinetic model that took into consideration the effects of influential inorganic ions, which are found obsequiously in drinking-water sources, to predict the degradation of 1,4-dioxane during the VUV process; and develop the kinetic model as the basis for the Lagrangian approach in the subsequent chapter.

First, degradation experiments of 1,4-dioxane with different concentrations of inorganic

ions were conducted in a flow-through photoreactor to identify which inorganic ions affect the degradation. A comprehensive list of elementary reactions and their reaction rate constants was compiled, and the kinetic model was built by a set of governer equations derived from the list. To verify and validate the model, a series of experiments were conducted in a quasi-collimated beam VUV apparatus and a flow-through VUV photoreactor using different water samples. The overall effects of hydrodynamics and radiation field in the flow-through photoreactor were measured by the chemical actinometry method (Heit et al., 1998; Rahn, 1997) and the prediction results were compared to the experimental data. Finally, the model was simplified by sensitivity analysis to reduce the cost of computational resources.

2.2 Experimental set-up and procedures

2.2.1 Chemicals and water samples

All chemicals were purchased commercially and used without further purification. Reagent solutions for the experiments were prepared with guaranteed reagent grade chemicals and Milli-Q water (18.2 MΩ·cm, Milli-Q Advantage, Millipore Co., Bedford, MA, USA). Six types of waters (Table 2-1) were used for the experiments: three groundwater (GW1−3), river water (RW), dechlorinated tap water (DTW), and synthetic water (SW). The GW1−3 samples were withdrawn from the raw water inputs to full-scale drinking water treatment plants (Tachikawa, Japan) and stored at 4 °C until use. No 1,4-dioxane was artificially added to the groundwaters for the experiments because the groundwaters had already been contaminated with 1,4-dioxane. The RW was withdrawn from the raw water input to a full-scale drinking water treatment plant (Ebetsu, Japan) and stored at 4 °C until use. DTW was prepared by passing tap water withdrawn at the laboratory through an activated carbon cartridge filter (TCC-WH-T0CP, Toyo Roshi Kaisha, Ltd., Tokyo, Japan) to remove residual free chlorine. No free chlorine residue in the DTW was confirmed by using the N, N-diethyl-p-phenylenediamine colorimetric assay for residual chlorine. The pH of RW and DTW was adjusted to 7.8 with NaOH, and then adding 1,4-dioxane (Fujifilm Wako Pure Chemical Corp., Osaka, Japan) to around 100 $\mu g \cdot L^{-1}$. The SW was prepared by pure water (15 MΩ·cm, Elix® Essential 10, Merck KGaA, Darmstadt, Germany), and then adjusting the pH and alkalinity using NaOH and $NaHCO_3$ to match those values of the GW3, spiked with 100 $\mu g \cdot L^{-1}$ of 1,4-dioxane before use.

Table 2-1 Chemical properties of the natural groundwater (GW1-3, Tachikawa, Japan), river water (RW, Ebetsu, Japan), dechlorinated tap water (DTW), and synthetic water (SW) used in this research

	pH	DOC	Na^+	K^+	Mg^{2+}	Ca^{2+}	Cl^-	NO_3^-	NO_2^-	SO_4^{2-}	HCO_3^-	1,4-dioxane
		$mg \cdot L^{-1}$	$\mu mol \cdot L^{-1}$									$\mu g \cdot L^{-1}$
GW1	7.8	0.06	588	16	259	531	1008	145	0	82	440	95
GW2	7.8[a]	0.07	607	18	374	765	655	314	0	231	450	55
GW3	7.8	0.09	666	35	505	1146	605	452	0	354	1050	36
RW	7.8[a]	2.2	700	60	162	296	460	54	0	9	380	100[c]
DTW	7.8[a]	0.20	768	44	73	296	482	17	0	139	140	100[c]
SW	7.8[a]	0.04	710	0	0	293	0	0	0	0	875	100[c]

[a] Artificially adjusted with NaOH.

[b] Artificially adjusted the pH and alkalinity using NaOH and $NaHCO_3$ to match those values of the GW3.

[c] Artificially added.

*The values indicated in the table are the post-adjustment value

To roughly investigates the effects of influential anions on 1,4-dioxane degradation, $NaHCO_3$ (for HCO_3^-), $NaNO_3$ (for NO_3^-), and NaCl (for Cl^-) were serially added to DTW at concentrations equal to those found in GW1 (Table 2-1) to prepare three DTW-based water (DTW_{HCO3}, $DTW_{HCO3+NO3}$, and $DTW_{HCO3+NO3+Cl}$, respectively). To more precisely quantify the effects of the influential anions on 1,4-dioxane degradation, further experiments using phosphate buffer solution (500 μM, pH 7.8), supplemented with 100 $\mu g \cdot L^{-1}$ 1,4-dioxane and different concentrations of $NaHCO_3$ (for HCO_3^-), $NaNO_3$ (for NO_3^-), $NaNO_2$ (for NO_2^-), or NaCl (for Cl^-), were prepared.

2.2.2 Degradation of 1,4-dioxane in a flow-through photoreactor

VUV treatments were conducted with a raw water tank, a pump, and a reactor (Aqua Solutions, UPM-18548-3B, Ube Industries, Ltd., Tokyo, Japan) (**Fig. 2-1**). The reactor (14 L) was horizontally divided by walls equipped with annular vessels (0.13 L each) into 5 chambers with the same volume. VUV lamps (NNI60/35XL, Heraeus Holding Gmbh, Hanau, Germany; 65W; 185 nm VUV radiation exitance 210 $W \cdot m^{-2}$, 254 nm UV radiation exitance 510 $W \cdot m^{-2}$, measured on the surface of the lamp), which had been turned on and allowed to warm up before experiment, were inserted inside the inner wall of the annular tube vessel. The 5 chambers and 4 annular tube vessels separating them subjected the water to three types of treatment ($Zone_1$, $Zone_2$, and $Zone_3$). Both the inner and outer walls of the annular tube vessels transmitted UV and VUV radiation. $Zone_1$ was the inside of the annular tube vessels. $Zone_2$ was located before the first and after the fourth of the annular tube vessels, whereas $Zone_3$ was located after the first and before the fourth of the annular vessels. The water in $Zone_3$ was irradiated with two VUV lamps, but the water in $Zone_2$ was irradiated with only one VUV lamp.

Raw water (100 L) was stored in a water tank and pumped into the reactor at a constant flow rate of 5 $L \cdot min^{-1}$ at room temperature. The water was forced to pass through the annular tube vessels ($Zone_1$) between the inner and outer walls from the bottom to the top, then to the next chamber ($Zone_2$ or $Zone_3$), and finally discharged from Outlet 5. Samples were withdrawn from Outlets 1–5, and the residual of the 1,4-dioxane was given by the concentrations at each Outlet divided by the concentration at Outlet 1 (**Fig. 2-1**). The VUV and UV doses of the system were determined by chemical actinometry according to the methods described by Heit et al. (1998) and Rahn (1997), respectively. The VUV dose in $Zone_1$ was 41 $\mu mol \cdot L^{-1} \cdot s^{-1}$, whereas the UV photon doses in $Zone_1$, $Zone_2$, and $Zone_3$ were 86, 1.0, and 2.0 $\mu mol \cdot L^{-1} \cdot s^{-1}$, respectively.

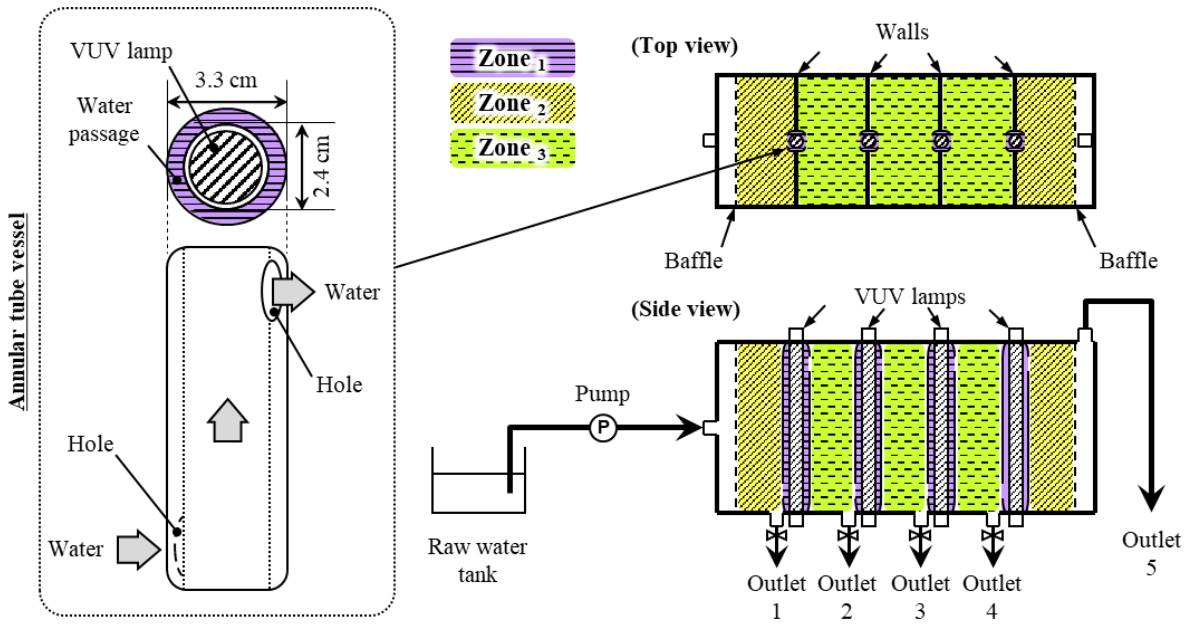

Fig. 2-1 Schematic of the flow-through VUV apparatus.

2.2.3 Batch mode experiments for model validation

A quasi-collimated beam VUV apparatus equipped was used in this research (**Fig. 2-2**). The distance between the top of the water to the radiation source was 30 cm. Milli-Q water with/without 20 mM phosphate buffer spiked with 100 μg·L^{-1} of 1,4-dioxane was used for comparison. A 100-mL glass beaker with a diameter of 4.5 cm (exposure area, 15.9 cm^2) was used as the reaction vessel. A water sample (60 mL, the path length of the quasi-collimated beam is 3.8 cm) was poured into the beaker and then covered with a wooden radiation shielding sheet until the experiment was started. To thoroughly mix the solution, a magnetic stirrer was used during the irradiation. A 65-W low-pressure mercury lamp emitting both 185 nm (VUV) and 254 nm (UV) photons was used as the radiation source (NIQ60/35XL, Heraeus Noblelight GmbH, Hanau, Germany). To suppress the absorption of VUV photons by oxygen in the gas phase, nitrogen gas was introduced into the reactor to obtain a volume fraction of oxygen of less than 2% before turning on the lamp. To ensure a steady radiation output, the lamp was turned on at least 20 min before the experiment. A calibrated radiometer (C9536/H9535, Hamamatsu Photonics K.K., Hamamatsu, Japan) was installed parallel to the surface of the irradiated water sample to determine the fluence rate during the experiments. The VUV and UV fluence rates at the center of the vessel were 1.0 and 3.2 W·m^{-2}, respectively. To observe the

change in 1,4-dioxane concentration, individual experiments with an irradiation time of 3, 6, 9, or 12 min were conducted. After the irradiation, an aliquot of the solution was withdrawn, and the 1,4-dioxane remaining in the solution was quantified.

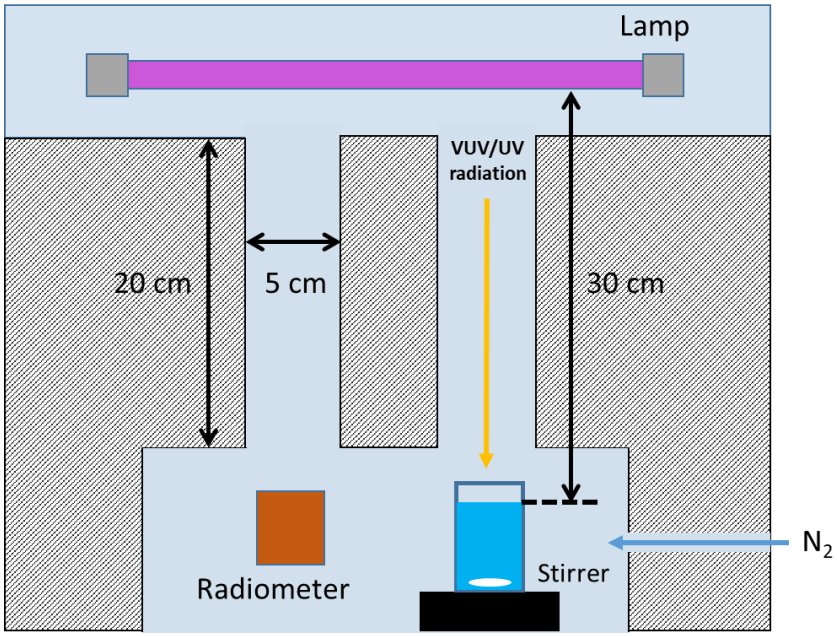

Fig. 2-2 Schematic of the quasi-collimated beam VUV apparatus.

In the presence of chloride during the VUV process, Cl-related radicals (Cl• and $Cl_2^{\bullet-}$) are generated (Dainton and Fowles, 1965). It is reported that Cl-related radicals can oxidize organics and directly contribute to OMPs degradation during the VUV process (Furatian and Mohseni, 2018). However, compared with OH radicals, Cl-related radicals are selective in oxidizing organics (Fang et al., 2014), and therefore some OMPs cannot be degraded by them. To further confirm whether the Cl-related radicals directly contributed to the degradation of 1,4-dioxane, a simple batch experiment was conducted in the apparatus. 1,4-Dioxane was dissolved at a concentration of approximately 100 $\mu g \cdot L^{-1}$ in a phosphate buffer (20 $mmol \cdot L^{-1}$, pH 7.8) containing 4000 $\mu mol \cdot L^{-1}$ of chloride (as NaCl). The solution was poured into two beakers, one of which was further supplemented with 500 $\mu mol \cdot L^{-1}$ of nitrobenzene (Fujifilm Wako Pure Chemical). Nitrobenzene, which has been reported to react only with OH radicals but not with Cl-related radicals (Fang et al., 2014; Watts and Linden, 2007), was accordingly used as the OH radical scavenger. The solutions were irradiated in the reactor simultaneously (the radiometer in **Fig. 2-1** was replaced by one of the beakers. The samples were withdrawn

from the beakers at predetermined intervals, and the 1,4-dioxane concentrations in the samples were measured.

2.2.4 Analytical methods

The concentration of 1,4-dioxane was measured by using a gas chromatograph-mass spectrometer (QP2010 Plus, Shimadzu Corporation, Kyoto, Japan) equipped with a purge and trap sample concentrator (AQUA PT 5000J Plus, GL Science Inc., Tokyo, Japan). A capillary column (HP-5MS; length 30 m, i.d. 250 μm, thickness 0.25 μm, Agilent Technologies, Palo Alto, CA, USA) was used for sample separation. The temperatures of the ion source, injector, and transfer line were controlled at 200, 180, and 180 °C, respectively. Gas chromatography-mass spectrometry was performed in the selected-ion-monitoring mode with d_8-1,4-dioxane (Fujifilm Wako Pure Chemical) as the internal standard; the fragment ions of 1,4-dioxane and d_8-1,4-dioxane were detected at *m*/*z* 88 and 96, respectively. Concentrations of cations were measured with an ion chromatograph (CS-1000, Dionex, Sunnyvale CA, USA) equipped with a separation column (IonPac CS 16, Dionex). Concentrations of anions were measured with an ion chromatograph (DX-120, Dionex) equipped with a separation column (IonPac AS14, Dionex). Dissolved organic carbon was quantified with a total organic carbon analyzer (Sievers 900, GE Analytical Instruments, Boulder, CO, USA) after passing the samples through a PTFE membrane (ϕ=0.2 μm Toyo Roshi Kaisha).

2.3 The kinetic model

2.3.1 Analytical modeling

Two mechanisms were involved in VUV processes by which OMPs can be degraded in pure water: direct photolysis and oxidation through reaction with OH radicals. Giving the relatively low concentration of OMPs (at ppb or ppt levels) in comparison with the concentration of water (55.6 $mol \cdot L^{-1}$, hence scavenging the majority of the 185 nm radiation), direct photolysis by VUV (185 nm) radiation can be assumed negligible (Crapulli et al., 2014). In contrast, since the absorption of UV (254 nm) radiation by water is relatively weak, a large amount of UV radiation is available to interact directly with the OMPs. Therefore, for a certain OMP (marked as species A) in water, its removal by the VUV process can be expressed as:

$$-\frac{dC_A}{dt} = k_{\cdot\mathrm{OH,\,A}} \cdot C_{\cdot\mathrm{OH}} \cdot C_A + k_{D,A} \cdot C_A \quad (2\text{-}1)$$

where $k_{\cdot\mathrm{OH,\,A}}$ is the second-order reaction rate constant for the OH radical and A, $k_{D,A}$ is the first-order reaction rate constants for direct photolysis of A, $C_{\cdot\mathrm{OH}}$ and C_A are the concentration of OH radicals and A, respectively. For 1,4-dioxane, the target pollutant in the research, the amount of direct UV photolysis of 1,4-dioxane observed in the experiments is limited due to its stable polar cyclic diether structure. The degradation of 1,4-dioxane in pure water occurs only by reaction with OH radicals during VUV processes (Matsushita et al., 2015; Patton et al., 2017), and its removal can be expressed as:

$$-\frac{dC}{dt} = k_{\cdot\mathrm{OH,\,dioxane}} \cdot C_{\cdot\mathrm{OH}} \cdot C \quad (2\text{-}2)$$

Therefore, the degradation rate of 1,4-dioxane in pure water is highly dependent on the concentration of the OH radicals. In the VUV process, the primary and majority OH radical generation reactions are the photochemical homolysis and ionization of water (Imoberdorf and Mohseni, 2012; Oppenländer, 2007):

$$H_2O \xrightarrow{h\nu\ 185\ \mathrm{nm}} \cdot OH + \cdot H \qquad \Phi_1 = 0.33$$

$$H_2O \xrightarrow{h\nu\ 185\ \mathrm{nm}} \cdot OH + H^+ + e^-_{aq} \qquad \Phi_2 = 0.045$$

where Φ_1 and Φ_2 are the quantum yields. The reaction of generated OH radicals and 1,4-dioxane occurs in the solution and the by-products formed:

$$1{,}4-\mathrm{dioxane} + \cdot\mathrm{OH} = \mathrm{by-products}$$

The products of the partial oxidation of 1,4-dioxane can undergo further degradation through reactions with OH radical (and/or other oxidants) potentially leading to complete mineralization. Since the by-produce reactions are complex (Zeng et al., 2017) and not the focus of this research, the equations for these reactions were not individually solved. Instead, the reactions are treated as one overall reaction with a certain rate constant (Bagheri and Mohseni, 2017):

$$\mathrm{by-products} + \cdot\mathrm{OH} \rightarrow \cdots \xrightarrow{\cdot OH} \cdots \xrightarrow{\cdot OH} \mathrm{final\ products}$$

Consistently with the natural water quality that carbonate/bicarbonate equilibrium played an important role in controlling pH, the equilibrium equations of carbonate/bicarbonate, and the reactions of carbonate/bicarbonate with OH radicals (Imoberdorf and Mohseni, 2012) must be considered in the kinetic model. Cl-related radicals that are selective in oxidizing organics (Fang et al., 2014) were reported to be generated during the VUV process in the water with chloride presence (Matthew and Anastasio, 2006). Therefore, the photochemical ionization reaction of chloride and the reaction between chloride with OH radicals must be included in the kinetic model. Under UV irradiation, the main emission of a low-pressure mercury lamp, the photolysis of nitrate leads to the formation of nitrite. The process of forming nitrite is complex and important during the VUV treatment (Mack and Bolton, 1999), which should also be added to the kinetic model.

Based on the above, a comprehensive list of elementary reactions and their rate constants in the VUV processes was made (Table 2-2). The resulting generalized kinetic model involved a total of 78 elementary reactions and 37 species: 7 radicals (·OH, ·H, $\cdot O_2H$, ·Cl, $\cdot NO_2$, ·ONOO, ·NO), 6 radical ions ($\cdot O^-$, $\cdot O_2^-$, $\cdot O_3^-$, $\cdot CO_3^-$, $\cdot OHCl^-$, $\cdot Cl_2^-$), 10 ions (H^+, OH^-, e_{aq}^-, HO_2^-, HCO_3^-, CO_3^{2-}, Cl^-, NO_3^-, NO_2^-, $ONOO^-$) and 14 molecules (H_2O, H_2O_2, H_2, O_2, CO_2, H_2CO_3, O_3, N_2O_4, N_2O_3, HOONO, $O(^3P)$,1,4-dioxane, by-products, NOM).

Table 2-2 List of the elementary reactions and the rate constants (compiled from primary and secondary sources) for the VUV processes

No.	Elementary reactions	Value	Reference
Photon-induced reactions			
1	$\mathbf{H_2O \xrightarrow{h\nu_{185nm}} \cdot OH + \cdot H}$	$\boldsymbol{\Phi_1 = 0.33}$	Imoberdorf and Mohseni, 2011
2	$\mathbf{H_2O \xrightarrow{h\nu_{185nm}} \cdot OH + H^+ + e_{aq}^-}$	$\boldsymbol{\Phi_2}$**=0.045**	Imoberdorf and Mohseni, 2011
3	$\mathbf{H_2O_2 \xrightarrow{h\nu_{185nm}} 2 \cdot OH}$	$\boldsymbol{\Phi_3 = 0.5}$	Imoberdorf and Mohseni, 2011
4	$\mathbf{H_2O_2 \xrightarrow{h\nu_{254nm}} 2 \cdot OH}$	$\boldsymbol{\Phi_4 = 0.5}$	Imoberdorf and Mohseni, 2011

Table 2-2 continued

No.	Elementary reactions	Value	Reference
5	$Cl^- \xrightarrow{h\nu_{185nm}} \cdot Cl + e_{aq}^-$	$\Phi_5 = 0.4$	Buxton et al., 1998
6	$O_3 + H_2O \xrightarrow{h\nu_{254nm}} H_2O_2 + O_2$	$\Phi_6 = 0.48$	Mack and Bolton, 1999
7	$NO_3^- \xrightarrow{h\nu_{254nm}} NO_2 \cdot + O^- \cdot$	$\Phi_7 = 0.09$	Mack and Bolton, 1999
8	$NO_2^- \xrightarrow{h\nu_{254nm}} NO \cdot + O^- \cdot$	$\Phi_8 = 0.046$	Mack and Bolton, 1999
9	$NO_3^- \xrightarrow{h\nu_{254nm}} NO_2^- + O(^3P)$	$\Phi_9 = 0.001$	Mack and Bolton, 1999
Equilibrium reactions			
10	$OH^- + H^+ \leftrightarrow H_2O$	$K_w = 10^{-14}$	Bagheri and Mohseni, 2017
11	$\cdot O_2H \leftrightarrow \cdot O_2^- + H^+$	$pK_{a11} = 4.8$	Bagheri and Mohseni, 2017
12	$H_2O_2 \leftrightarrow HO_2^- + H^+$	$pK_{a12} = 11.6$	Bagheri and Mohseni, 2017
13	$O_2 + \cdot O^- \leftrightarrow \cdot O_3^-$	$k_{13+} = 3.5 \times 10^9 L\ mol^{-1}s^{-1}$ $k_{13-} = 4.6 \times 10^3 s^{-1}$	Zvereva, 2010 NIST Database
14	$H_2CO_3 \leftrightarrow HCO_3^- + H^+$	$pK_{a14} = 6.3$	Bagheri and Mohseni, 2017
15	$HCO_3^- \leftrightarrow CO_3^{2-} + H^+$	$pK_{a15} = 10.3$	Bagheri and Mohseni, 2017
16	$\cdot OH + Cl^- \leftrightarrow \cdot ClOH$	$k_{16+} = 4.3 \times 10^9 L\ mol^{-1}s^{-1}$ $k_{16-} = 6.1 \times 10^9 s^{-1}$	Matthew and Anastasio, 2006
17	$\cdot Cl + Cl^- \leftrightarrow \cdot Cl_2^-$	$k_{17+} = 6.5 \times 10^9 L\ mol^{-1}s^{-1}$ $k_{17-} = 1.1 \times 10^5 s^{-1}$	Matthew and Anastasio, 2006
18	$\cdot ClOH + H^+ \leftrightarrow \cdot Cl + H_2O$	$k_{18+} = 2.1 \times 10^{10} L\ mol^{-1}s^{-1}$ $k_{18-} = 2.5 \times 10^8 s^{-1}$	Matthew and Anastasio, 2006 Buxton et al., 1998
19	$N_2O_4 \leftrightarrow 2NO_2 \cdot$	$k_{19+} = 6.9 \times 10^3 s^{-1}$ $k_{19-} = 4.5 \times 10^8 L\ mol^{-1}s^{-1}$	Gonzalez et al., 2004 Mack and Bolton, 1999
20	$HOONO \leftrightarrow ONOO^- + H^+$	$k_{20+} = 3.2 \times 10^{16} s^{-1}$ $k_{20-} = 1.0 \times 10^{10} L\ mol^{-1}s^{-1}$	Mack and Bolton, 1999

Table 2-2 continued

No.	Elementary reactions	Value	Reference
Degradation reactions			
21	$\mathbf{1,4-dioxane + \cdot OH = by-products}$	$\mathbf{k_{21} = 3.1 \times 10^9 L\ mol^{-1} s^{-1}}$	Patton et al., 2017
22	$\mathbf{by-products + \cdot OH \rightarrow \cdots \xrightarrow{\cdot OH} \cdots \xrightarrow{\cdot OH} final\ products}$	$\mathbf{k_{22} = 1.0 \times 10^9 L\ mol^{-1} s^{-1}}$	Bagheri and Mohseni, 2017
23	$\mathbf{NOM + \cdot OH = products}$	$\mathbf{k_{23} = 2.0 \sim 9.0 \times 10^8 L\ mol^{-1} s^{-1}}$	Westerhoff et al., 2007
Other involving reactions			
24	$\mathbf{\cdot H + OH^- \rightarrow e_{aq}^- + H_2O}$	$\mathbf{k_{24} = 3.6 \times 10^8 L\ mol^{-1} s^{-1}}$	Imoberdorf and Mohseni, 2012
25	$\mathbf{\cdot H + O_2 \rightarrow \cdot O_2H}$	$\mathbf{k_{25} = 2.1 \times 10^{10} L\ mol^{-1} s^{-1}}$	Imoberdorf and Mohseni, 2012
26	$\mathbf{e_{aq}^- + O_2 \rightarrow \cdot O_2^-}$	$\mathbf{k_{26} = 2.0 \times 10^7 L\ mol^{-1} s^{-1}}$	Imoberdorf and Mohseni, 2012
27	$\mathbf{\cdot OH + \cdot O_2H \rightarrow H_2O + O_2}$	$\mathbf{k_{27} = 6.6 \times 10^9 L\ mol^{-1} s^{-1}}$	Imoberdorf and Mohseni, 2012
28	$\mathbf{\cdot OH + \cdot O_2^- \rightarrow OH^- + O_2}$	$\mathbf{k_{28} = 7.0 \times 10^9 L\ mol^{-1} s^{-1}}$	Imoberdorf and Mohseni, 2012
29	$\mathbf{2 \cdot OH \rightarrow H_2O_2}$	$\mathbf{k_{29} = 4.0 \times 10^9 L\ mol^{-1} s^{-1}}$	Imoberdorf and Mohseni, 2012
30	$\mathbf{2 \cdot O_2H \rightarrow H_2O_2 + O_2}$	$\mathbf{k_{30} = 2.6 \times 10^6 L\ mol^{-1} s^{-1}}$	Imoberdorf and Mohseni, 2012
31	$\mathbf{\cdot O_2^- + \cdot O_2H \rightarrow HO_2^- + O_2}$	$\mathbf{k_{31} = 9.7 \times 10^7 L\ mol^{-1} s^{-1}}$	Imoberdorf and Mohseni, 2012
32	$\mathbf{\cdot OH + H_2 \rightarrow \cdot H + H_2O}$	$\mathbf{k_{32} = 6.0 \times 10^7 L\ mol^{-1} s^{-1}}$	Imoberdorf and Mohseni, 2011
33	$\mathbf{\cdot OH + \cdot H \rightarrow H_2O}$	$\mathbf{k_{33} = 7.0 \times 10^9 L\ mol^{-1} s^{-1}}$	Imoberdorf and Mohseni, 2011
34	$\mathbf{\cdot OH + OH^- \rightarrow \cdot O^- + H_2O}$	$\mathbf{k_{34} = 3.9 \times 10^8 L\ mol^{-1} s^{-1}}$	Imoberdorf and Mohseni, 2011
35	$\mathbf{\cdot OH + H_2O_2 \rightarrow \cdot O_2H + H_2O}$	$\mathbf{k_{35} = 2.7 \times 10^7 L\ mol^{-1} s^{-1}}$	Imoberdorf and Mohseni, 2011
36	$\mathbf{\cdot OH + e \rightarrow OH^-}$	$\mathbf{k_{36} = 3.0 \times 10^{10} L\ mol^{-1} s^{-1}}$	Imoberdorf and Mohseni, 2011
37	$\mathbf{\cdot OH + HO_2^- \rightarrow OH^- + \cdot O_2H}$	$\mathbf{k_{37} = 7.5 \times 10^9 L\ mol^{-1} s^{-1}}$	Imoberdorf and Mohseni, 2011

Table 2-2 continued

No.	Elementary reactions	Value	Reference
38	$\cdot OH + \cdot O^- \rightarrow HO_2^-$	$k_{38} = 2.0 \times 10^9 L\ mol^{-1} s^{-1}$	Zvereva, 2010
39	$\cdot H + H_2O \rightarrow \cdot OH + H_2$	$k_{39} = 0.55\ s^{-1}$	Zvereva, 2010
40	$2 \cdot H \rightarrow H_2$	$k_{40} = 1.0 \times 10^{10} L\ mol^{-1} s^{-1}$	Imoberdorf and Mohseni, 2011
41	$\cdot H + \cdot O_2H \rightarrow H_2O_2$	$k_{41} = 1.0 \times 10^{10} L\ mol^{-1} s^{-1}$	Imoberdorf and Mohseni, 2012
42	$\cdot H + \cdot O_2^- \rightarrow HO_2^-$	$k_{42} = 2.0 \times 10^{10} L\ mol^{-1} s^{-1}$	Imoberdorf and Mohseni, 2011
43	$\cdot H + H_2O_2 \rightarrow H_2O + \cdot OH$	$k_{43} = 9.0 \times 10^7 L\ mol^{-1} s^{-1}$	Imoberdorf and Mohseni, 2012
44	$e_{aq}^- + H^+ \rightarrow \cdot OH$	$k_{44} = 2.3 \times 10^{10} L\ mol^{-1} s^{-1}$	Imoberdorf and Mohseni, 2012
45	$e_{aq}^- + H_2O_2 \rightarrow OH^- + \cdot OH$	$k_{45} = 1.1 \times 10^{10} L\ mol^{-1} s^{-1}$	Imoberdorf and Mohseni, 2012
46	$\cdot O_2^- + H_2O_2 \rightarrow OH^- + \cdot OH + O_2$	$k_{46} = 1.6 \times 10\ L\ mol^{-1} s^{-1}$	Imoberdorf and Mohseni, 2012
47	$\cdot O^- + \cdot O_3^- \rightarrow 2 \cdot O_2^-$	$k_{47} = 7.0 \times 10^9\ L\ mol^{-1} s^{-1}$	Zvereva, 2010
48	$\cdot OH + CO_3^{2-} \rightarrow \cdot CO_3^{2-} + OH^-$	$k_{48} = 3.9 \times 10^8\ L\ mol^{-1} s^{-1}$	Crittenden et al., 1999
49	$\cdot OH + HCO_3^{2-} \rightarrow \cdot CO_3^{2-} + H_2O$	$k_{49} = 8.5 \times 10^6\ L\ mol^{-1} s^{-1}$	Crittenden et al., 1999
50	$H_2O_2 + \cdot CO_3^{2-} \rightarrow HCO_3^- + \cdot O_2H$	$k_{50} = 4.3 \times 10^5\ L\ mol^{-1} s^{-1}$	Crittenden et al., 1999
51	$HO_2^- + \cdot CO_3^{2-} \rightarrow CO_3^{2-} + \cdot O_2H$	$k_{51} = 3.0 \times 10^7\ L\ mol^{-1} s^{-1}$	Crittenden et al., 1999
52	$\cdot O_2^- + \cdot CO_3^{2-} \rightarrow CO_3^{2-} + O_2$	$k_{52} = 7.0 \times 10^8\ L\ mol^{-1} s^{-1}$	Bagheri and Mohseni, 2017
53	$\cdot O^- + H^+ \rightarrow \cdot OH$	$k_{53} = 1.0 \times 10^{10}\ L\ mol^{-1} s^{-1}$	Zvereva, 2010
54	$\cdot O_3^- + \cdot CO_3^{2-} \rightarrow CO_3^{2-} + O_3$	$k_{54} = 6.0 \times 10^7\ L\ mol^{-1} s^{-1}$	Buxton et al., 1988
55	$e_{aq}^- + O_3 \rightarrow \cdot O_3^-$	$k_{55} = 3.6 \times 10^{10}\ L\ mol^{-1} s^{-1}$	Sehested et al., 1983
56	$\cdot H + O_3 \rightarrow \cdot OH + O_2$	$k_{56} = 3.6 \times 10^{10}\ L\ mol^{-1} s^{-1}$	Sehested et al., 1983
57	$\cdot Cl_2^- + \cdot O_2H \rightarrow 2Cl^- + O_2 + H^+$	$k_{57} = 3.0 \times 10^9\ L\ mol^{-1} s^{-1}$	Matthew and Anastasio, 2006
58	$\cdot Cl_2^- + \cdot O_2^- \rightarrow 2Cl^- + O_2$	$k_{58} = 1.0 \times 10^9\ L\ mol^{-1} s^{-1}$	Matthew and Anastasio, 2006

Table 2-2 continued

No.	Elementary reactions	Value	Reference
59	$\cdot Cl_2^- + H_2O_2 \rightarrow 2Cl^- + \cdot O_2H + H^+$	$k_{59} = 1.4 \times 10^5\ L\ mol^{-1}s^{-1}$	Matthew and Anastasio, 2006
60	$\cdot Cl + CO_3^{2-} \rightarrow \cdot CO_3^{2-} + Cl^-$	$k_{60} = 5.0 \times 10^8\ L\ mol^{-1}s^{-1}$	Matthew and Anastasio, 2006
61	$\cdot Cl + HCO_3^- \rightarrow \cdot CO_3^{2-} + Cl^- + H^+$	$k_{61} = 2.2 \times 10^8\ L\ mol^{-1}s^{-1}$	Matthew and Anastasio, 2006
62	$\cdot Cl_2^- + CO_3^{2-} \rightarrow 2Cl^- + \cdot CO_3^{2-}$	$k_{62} = 8.0 \times 10^7\ L\ mol^{-1}s^{-1}$	Matthew and Anastasio, 2006
63	$\cdot Cl_2^- + HCO_3^- \rightarrow 2Cl^- + \cdot CO_3^{2-} + H^+$	$k_{63} = 1.6 \times 10^8\ L\ mol^{-1}s^{-1}$	Matthew and Anastasio, 2006
64	$\cdot OH + \cdot NO_2 \rightarrow HOONO$	$k_{64} = 1.3 \times 10^9\ L\ mol^{-1}s^{-1}$	Mack and Bolton, 1999
65	$\cdot OH + ONOO^- \rightarrow \cdot ONOO + OH^-$	$k_{65} = 5.0 \times 10^9\ L\ mol^{-1}s^{-1}$	Mack and Bolton, 1999
66	$\cdot ONOO \rightarrow \cdot NO + O_2$	$k_{66} = 1.0 \times 10^{10}\ s^{-1}$	Mack and Bolton, 1999
67	$\cdot NO_2 + \cdot ONOO + H_2O \rightarrow 2NO_3^- + 2H^+$	$k_{67} = 1.0 \times 10^{10}\ L\ mol^{-1}s^{-1}$	Mack and Bolton, 1999
68	$\cdot NO_2 + \cdot H \rightarrow NO_2^- + H^+$	$k_{68} = 6.0 \times 10^8\ L\ mol^{-1}s^{-1}$	Gonzalez and Braun, 1995
69	$NO_2^- + \cdot OH \rightarrow \cdot NO_2 + OH^-$	$k_{69} = 1.0 \times 10^{10}\ L\ mol^{-1}s^{-1}$	Gonzalez and Braun, 1995
70	$N_2O_4 + H_2O \rightarrow NO_2^- + NO_3^- + 2H^+$	$k_{70} = 1.0 \times 10^3\ s^{-1}$	Mack and Bolton, 1999
71	$\cdot NO_2 + \cdot O_2^- \rightarrow NO_2^- + O_2$	$k_{71} = 1.0 \times 10^8\ L\ mol^{-1}s^{-1}$	Mack and Bolton, 1999
72	$\cdot NO + \cdot OH \rightarrow NO_2^- + H^+$	$k_{72} = 1.0 \times 10^{10}\ L\ mol^{-1}s^{-1}$	Mack and Bolton, 1999
73	$\cdot NO_2 + e_{aq}^- \rightarrow NO_2^-$	$k_{73} = 4.6 \times 10^8\ L\ mol^{-1}s^{-1}$	Mack and Bolton, 1999
74	$\cdot NO + \cdot NO_2 \rightarrow N_2O_3$	$k_{74} = 1.1 \times 10^9\ L\ mol^{-1}s^{-1}$	Mack and Bolton, 1999
75	$N_2O_3 + H_2O \rightarrow 2NO_2^- + 2H^+$	$k_{75} = 5.3 \times 10^2\ s^{-1}$	Mack and Bolton, 1999
76	$NO_3^- + \cdot OH \rightarrow \cdot ONOO + OH^-$	$k_{76} = 1.1 \times 10^5\ L\ mol^{-1}s^{-1}$	Mack and Bolton, 1999
77	$NO_3^- + O(^3P) \rightarrow NO_2^- + O_2$	$k_{77} = 3.0 \times 10^8\ L\ mol^{-1}s^{-1}$	Mack and Bolton, 1999
78	$NO_2^- + O(^3P) \rightarrow NO_3^-$	$k_{78} = 3.0 \times 10^9\ L\ mol^{-1}s^{-1}$	Mack and Bolton, 1999

2.3 The kinetic model

For each species involved in the VUV processes, differential mass-balance equations were set where radiation-independent rate terms for a generic reaction, $aA + bB \rightarrow cC + dD$, were taken into account and mathematically formulated as:

$$R = -\frac{1}{a}\frac{dC_A}{dt} = -\frac{1}{b}\frac{dC_B}{dt} = \frac{1}{c}\frac{dC_C}{dt} = \frac{1}{d}\frac{dC_D}{dt} = k_{A,B}C_A^a C_B^b \quad (2\text{-}3)$$

where A, B, C, and D represent generic species involved in the reaction with their stoichiometric coefficients *a*, *b*, *c*, and *d*, $k_{A,B}$ was the second-order kinetic rate constant, and C_A, C_B, C_C, and C_D were the concentration of the species A, B, C, and D, respectively. Using the same symbolism, the rate of the radiation-dependent reactions in the generic form of $aA \xrightarrow{h\nu} bB + cC + dD$ was formulated for each radiation-initiated reaction, giving a reaction rate (Oppenlander, 2007):

$$R = -\frac{1}{a}\frac{dC_A}{dt} = \frac{1}{b}\frac{dC_B}{dt} = \frac{1}{c}\frac{dC_C}{dt} = \frac{1}{d}\frac{dC_D}{dt} = \Phi\frac{1}{N_A}\frac{\lambda}{hc}\frac{E}{V}C_A^a \quad (2\text{-}4)$$

where A, B, C, and D represent generic species with their stoichiometric coefficients *a*, *b*, *c*, and *d*, Φ represent the specific quantum yield, N_A the Avogadro's constant, λ the wavelength, *h* the Planck's constant, *c* the speed of light, *E* represents the power of radiation absorbed by A, *V* the volume of the irradiated solution.

In this research, the absorbed radiation power was estimated using the average fluence rate (E_{avg}) obtained from the quasi-collimated beam VUV apparatus, which can be corrected by using the radiometer reading (E_0) and four other parameters (Bolton and Stefan, 2002):

$$E_{avg} = E_0 \cdot RF \cdot PF \cdot WF \cdot DF \quad (2\text{-}5)$$

where *RF* is the reflection factor with the approximate value of 0.975 at the interface of water and air. *PF*, *DF* stands for Petri factor and divergence factor of the quasi-collimated beam VUV apparatus, with the value of 0.70 (PF_{VUV}), 0.95 (PF_{UV}), and 0.89, respectively. *WF* corrects for attenuation of the incident fluence rate due to absorption in the irradiated column:

$$WF = (1 - 10^{-\alpha l}) \cdot \frac{\varepsilon_A C_A}{\alpha} \quad (2\text{-}6)$$

where l is the depth of the solution, α is the absorption coefficient of the solution at the wavelength λ (common logarithm), $\varepsilon_{A,\lambda}$ represent s the molar absorption coefficient of the species at the wavelength λ. In this research, the absorption coefficient of the solution at a given wavelength was defined as follows:

$$\alpha_{185} = \varepsilon_{H_2O,185} C_{H_2O} + \varepsilon_{H_2O_2,185} C_{H_2O_2} + \varepsilon_{SO_4^{2-},185} C_{SO_4^{2-}} + \varepsilon_{Cl^-,185} C_{Cl^-}$$

$$+\varepsilon_{HCO_3^-,185} C_{HCO_3^-} + \varepsilon_{CO_3^{2-},185} C_{CO_3^{2-}} \quad (2\text{-}7)$$

$$\alpha_{254} = \varepsilon_{H_2O_2,254} C_{H_2O_2} + \varepsilon_{NO_3^-,254} C_{NO_3^-} + \varepsilon_{NO_2^-,254} C_{NO_2^-} \quad (2\text{-}8)$$

In particular, the values of ε equal to 3.24×10^{-2} and 0 L·mol^{-1}·cm^{-1} (base 10) were considered for water at the wavelengths of 185 and 254 nm (J. L. Weeks et al., 1963), respectively; for H_2O_2, the values of ε equal to 289 and 18.4 L·mol^{-1}·cm^{-1} (base 10) were chosen for the wavelengths at 185 and 254 nm (Oppenländer, 2007), respectively; the values ε equal to 1.28×10^1 and 3.98 L·mol^{-1}·cm^{-1} (base 10) at 254 nm for NO_2^- and NO_3^- (Bayliss and Bucat, 1975), respectively. The molar absorption coefficients of the SO_4^{2-}, Cl^-, CO_3^{2-}, and HCO_3^- were 1.86×10^2, 3.6×10^3, 1.75×10^3, and 1.1×10^3 L·mol^{-1}·cm^{-1} (base 10) at 185 nm (Imoberdorf and Mohseni, 2011; J L Weeks et al., 1963), respectively.

Based on the all above, for each species in the system, an ordinary differential equation (ODE) can be formed:

$$\frac{dC_A}{dt} = \sum_i a_{g,i} R_{g,i} - \sum_j a_{c,j} R_{c,j} \quad (2\text{-}9)$$

where C_A represents the concentration of spices A, $R_{g,i}$ and $R_{c,j}$ represent the specific generation and consumption reaction rate of spices A with their stoichiometric coefficients $a_{g,i}$ and $a_{c,j}$, respectively. The system of the obtained ODEs was solved (**Appendix 1**) in MATLAB by using the stiff solver ODE15s with relative and absolute tolerance set to 10^{-10} and 10^{-30}, respectively. Simulation representing different water qualities was conducted by prescribing as initial conditions included in the profiles.

2.3.2 Sensitivity analysis of the kinetic model

A sensitivity analysis (Crapulli et al., 2014) was conducted to determine the impact of reaction rate constants on the model simulations. In case of disagreement among published values, the values, that the experimental condition was similar to this research, were used in the sensitivity analysis. The relative importance of a given elementary reaction k_x was estimated by quantifying the change in the time-dependent concentration $\Delta C_{A,k_x}$ of a generic species A (e.g. OH radicals) obtained when all elementary reactions $k_1 + k_2 + \cdots + k_n$ were considered versus the case when all elementary reactions minus the one of concern k_x was used in the simulations.

$$\Delta C_{A,k_x} = \frac{\sum_{i=1}^{T}\left(C_{A,k_1+k_2+\cdots+k_n,i} - C_{A,k_1+k_2+\cdots+k_n-k_x,i}\right)}{T} \quad (2.10)$$

The sensitivity analysis and elimination of unimportant reactions were deemed necessary because a minimum number of reactions is needed to obtain a relevant steady-state solution and reduce the cost of computational resources.

2.3.3 Model application for the flow-through photoreactor

To test whether the model could be correctly applied to the particles in the Lagrangian approach after adding the information of the hydrodynamics and radiation field, the model was applied to predict the 1,4-dioxane degradation in the flow-through photoreactor (**Fig. 2-1**) by dividing it into 9 calculation units connected in series (**Fig. 2-3**), in which the radiation dose and hydraulic residence time were set up as described in **Section 2.2.2**.

The first calculation unit took the concentration of each species in the raw water as the initial boundary condition to begin the calculation, and the subsequent units took the calculation result of the concentrations of the species for its previous unit as the initial boundary condition to calculate the degradation in the current unit, then repeat this operation until the outlet. The concentration of 1,4-dioxane output by the first unit was used as C_0, the same as the experimental procedure described in **Section2.2.2**. The output concentrations of C_1, C_2, C_3, and C_4 were the predicted values against the experimental measured valued at the corresponding outlet in **Fig. 2-1**.

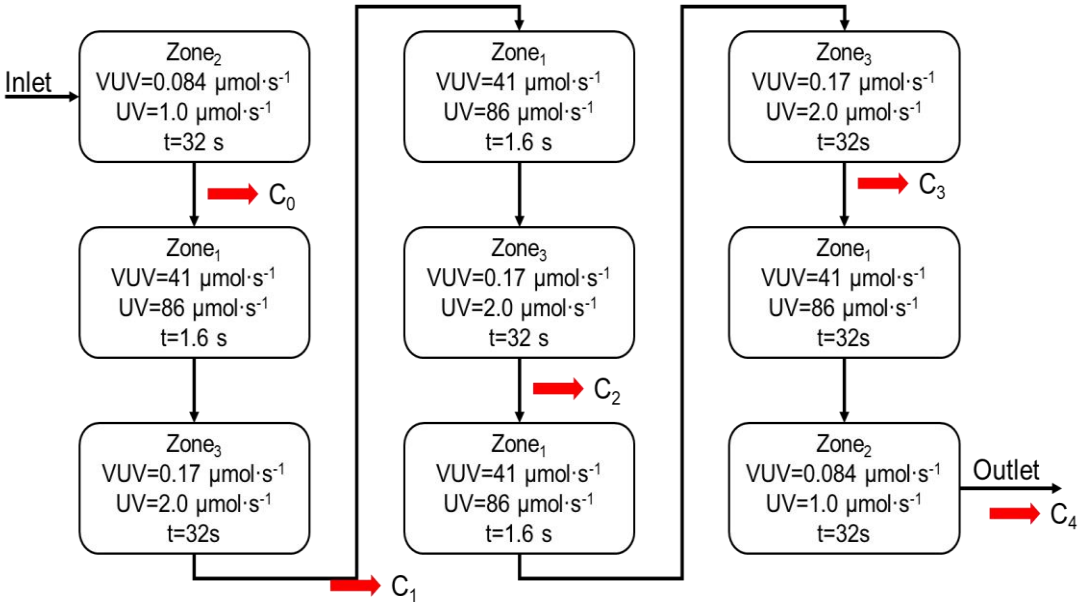

Fig. 2-3 Schematic of the calculation process by using the kinetic model for the flow-through photoreactor.

2.4 Results and discussion

2.4.1 The influential ions on 1,4-dioxane degradation

Experiments were conducted in the flow-through VUV photoreactor (**Fig. 2-1**) using actual contaminated GW 1 and DTW-based waters, the results were shown in **Fig. 2-4**. 1,4-dioxane was rapidly degraded with VUV treatment in DTW (**Fig.2-4**, black), and the residual ratio finally reached approximately 0.02 at a VUV photon dose of 270 μmol·L^{-1}. At the same VUV dose, in contrast, the residual ratio was 0.22 in GW1 (**Fig. 2-4**, red), which was much higher than the residual ratio in DTW. As a result, 1,4-dioxane degradation by the VUV process was suppressed in GW1 compared with the degradation in DTW.

Degradation of OMPs during the VUV process is reportedly influenced by water quality parameters (Zoschke et al., 2014). Dissolved oxygen (DO) has been reported to affect the degradation of OMPs in the VUV process (Alapi and Dombi, 2007; Kutschera et al., 2009; Shirayama et al., 2001), whereas the DO was almost the same in GW 1 (8.9 mg·L^{-1}) and DTW (9.0 mg·L^{-1}). The pH also affects the degradation of OMPs (Imoberdorf and Mohseni, 2012; Kutschera et al., 2009), whereas the pH of DTW was adjusted to the same as the GW 1 before the experiment. Therefore, the suppression was mainly caused by the different concentrations

of inorganic ions and NOM between GW 1 and DTW (**Table 2-1)**.

To identify the causes of the suppression in 1,4-dioxane degradation in GW1, experiments were conducted while inorganic ions were serially added to DTW to make the ion concentration equivalent to GW 1. The degradation of 1,4-dioxane was suppressed when $NaHCO_3$ was added to DTW (DTW_{HCO3}, **Fig. 2-4**, blue), indicating that one or both of sodium and bicarbonate was the suppressor to the 1,4-dioxane degradation. Further experiments of adding $NaNO_3$ to DTW_{HCO3} ($DTW_{HCO3+NO3}$, **Fig. 2-4**, pink) were conducted, the suppression result of 1,4-dioxane degradation compared DTW_{HCO3} indicated that one or both of sodium and nitrate was the suppressor to the degradation. The degradation of 1,4-dioxane was further suppressed after added NaCl to $DTW_{HCO3+NO3}$ ($DTW_{HCO3+NO3+Cl}$, **Fig. 2-4**, green), indicating that one or both of sodium and chloride was the suppressor to the degradation.

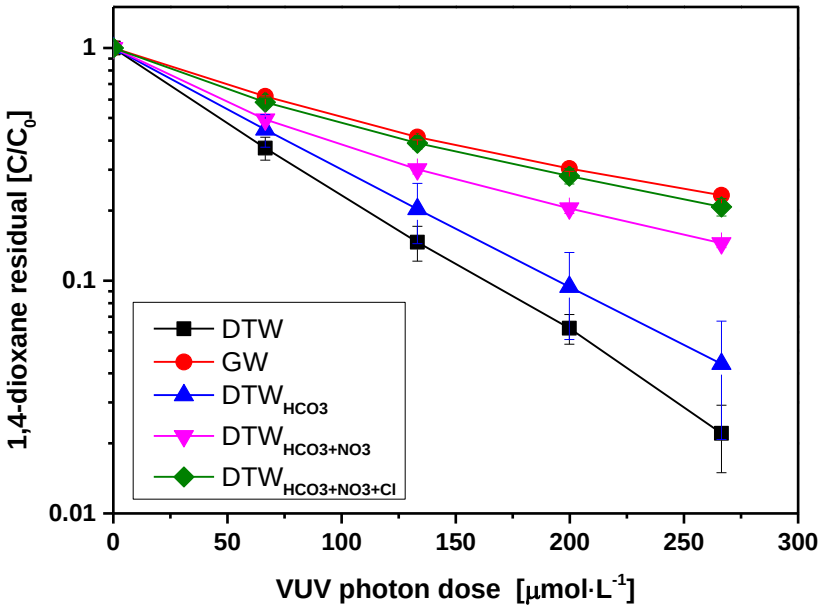

Fig. 2-4 Change in 1,4-dioxane residual with VUV irradiation. Error bars indicate standard deviations of at least three experiments.

To determine whether sodium ions suppressed the degradation of 1,4-dioxane, DTW was supplemented with either NaCl, $CaCl_2$, or $MgCl_2$ at similar chloride concentrations (800–1000 $\mu mol \cdot L^{-1}$) and then subjected to VUV treatment. The degradation rates of 1,4-dioxane were almost the same (**Fig. 2-5** (A)), even though the cation concentrations were different from each other (**Fig. 2-5** (B)). These results suggested that the degradation of 1,4-dioxane was affected by the anion rather than the cations. Moreover, the degradation rater of 1,4-dioxane was almost

the same in $DTW_{HCO3+NO3+Cl}$ and GW1 (**Fig. 2-4**), indicating that the suppression was completely explained by these three anions. NOM has been reported to reduce the degradations of OMPs by VUV irradiation (Imoberdorf and Mohseni, 2012; Kutschera et al., 2009; Wols et al., 2015), the contribution of NOM to the suppression was negligibly small in the GW1 and DTW based waters, probably because the concentrations of DOC in both of them were very small (<0.2 $mg \cdot L^{-1}$, Table 2-1). Therefore, the suppressions observed in the experiments with the DTW-based waters were probably due to the anions, namely bicarbonate, nitrate, and chloride. The result also shows that the kinetic model that only taking into account bicarbonate and natural organic matter (NOM) to assess the effects of water qualities (Bagheri and Mohseni, 2014, 2015, 2017; Crapulli et al., 2014) is insufficient to accurately describe the 1,4-dioxane degradation in actual raw water.

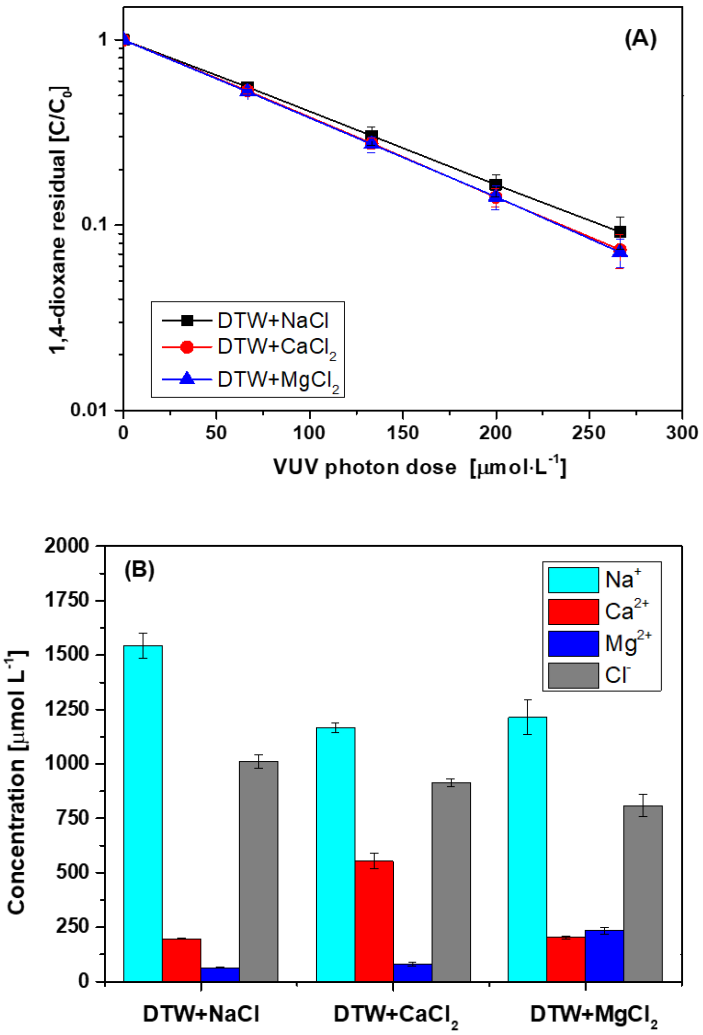

Fig. 2-5 Comparison of 1,4-dioxane degradation among buffered DTW: (A) 1,4-dioxane residual; (B) ion concentrations in buffered DTW. Error bars indicate standard deviations of at least two experiments.

To more precisely quantify the effects of these three anions on 1,4-dioxane degradation during VUV treatment, further experiments on Milli-Q-based waters containing each anion at different concentrations were conducted (**Fig. 2-6**). The decrease of the apparent pseudo-first-order degradation rate constant of 1,4-dioxane with increasing bicarbonate concentration (**Fig. 2-6** (A)) when $NaHCO_3$ was added to the buffered Milli-Q water indicated that bicarbonate contributed to the suppression. Bicarbonate has been reported (Imoberdorf and Mohseni, 2012) to react with the OH radical to form a carbonate radical ($\bullet CO_3^-$) (Eq. 48). $\bullet CO_3^-$ is approximately 1000 times less reactive than OH radical (Mazellier et al., 2007), the contribution of $\bullet CO_3^-$ to the degradations of target OMPs is expected to be negligible. Bicarbonate, therefore, reduces the degradation rates of OMPs during VUV treatment (Kutschera et al., 2009).

The decrease of the apparent pseudo-first-order degradation rate constant with increasing nitrate concentration (**Fig. 2-6** (B)) when $NaNO_3$ was added to the buffered Milli-Q water suggested that nitrate contributed to the suppression. Nitrate is transformed to a nitrite radical ($NO_2\bullet$) by UV light irradiation (Eq. 7). Two molecules of $NO_2\bullet$ generate one molecule of N_2O_4 (Eq. 19), which are then hydrolyzed to one mole of nitrite and nitrate (Eq. 70). These reactions have been reported to be very fast (Zoschke et al., 2014). Some of the nitrates are transformed via these reactions into nitrite by the UV irradiation that occurs concomitantly during VUV treatment. The nitrite concentration, therefore, increased in the solution supplemented with nitrate during the VUV treatment in this research. The consumption of OH radical is therefore expected to be negligibly small for nitrate compared with nitrite. Accordingly, 1,4-dioxane degradation is suppressed by nitrite rather than nitrate. The concentration dependence of the suppression of 1,4-dioxane degradation was confirmed by the experiments with solutions containing different initial nitrite concentrations (**Fig. 2-5** (C)).

The degradation of 1,4-dioxane was increasingly suppressed by higher chloride concentrations (**Fig. 2-5** (D)). Chloride reacts with OH radicals to form $ClHO\bullet^-$ (Eq. 16), and then Cl-related radicals are generated in subsequent reactions (Eqs. 17 and 18). In UV/free chlorine treatment, Cl-related radicals have been reported to play a partial role in OMPs degradation (Fang et al., 2014; Guo et al., 2017). However, in the VUV process of this research, Cl-related radicals probably did not contribute to the degradation of 1,4-dioxane because the expected concentrations of Cl-related radicals were much lower than those expected in UV/free chlorine treatment.

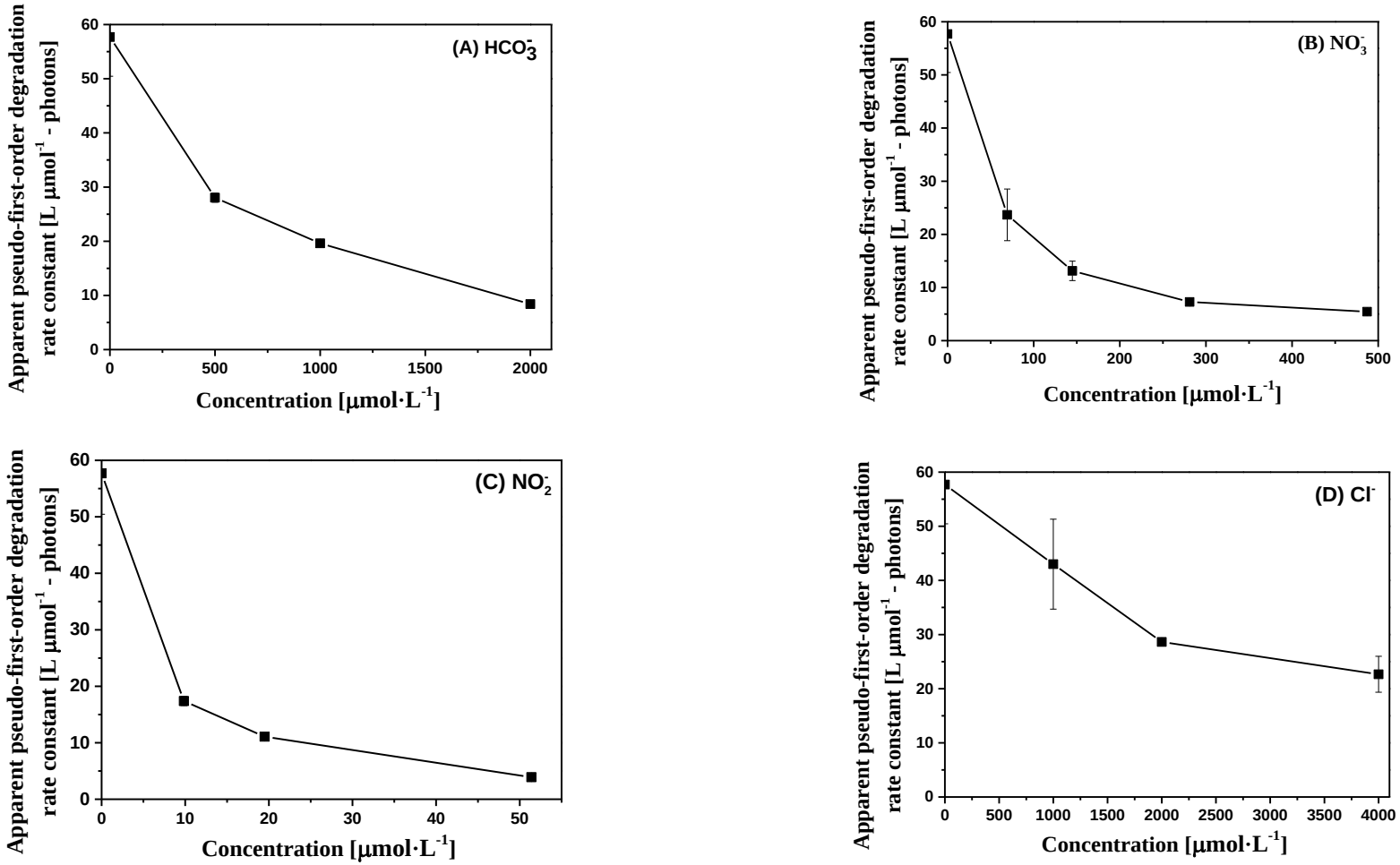

Fig. 2-6 Effects of concentrations of (A) HCO_3^-, (B) NO_3^-, (C) NO_2^-, and (D) Cl^- in buffered Milli-Q water on apparent pseudo-first-order degradation rate constant of 1,4-dioxane during VUV treatment.

To investigate whether the Cl-related radicals contributed to the degradation of 1,4-dioxane, batch mode degradation experiments with nitrobenzene (OH radicals scavenger) were conducted, and the result was shown in **Fig. 2-7**. Although 1,4-dioxane degradation occurred in the absence of nitrobenzene under VUV irradiation (**Fig. 2-7**), it did not degrade in the presence of nitrobenzene. The observation clearly showed that the degradation of 1,4-dioxane resulted in the reaction with OH radicals alone, reactions with Cl-related radicals (as well as direct photolysis by UV and VUV light) did not result in the degradation of 1,4-dioxane directly, even in the presence of the highest concentration of chloride (4000 μM) used in the flow-through experiments. Li et al. (2017) reported that the contribution of Cl-related radicals to the degradation of 1,4-dioxane was limited, even in a UV/free chlorine treatment in which the concentrations of Cl-related radicals were much higher than this research. They concluded that the major chemical species responsible for the degradation was OH radical. Chloride, therefore, suppressed the degradation of 1,4-dioxane by competitive consumption of OH radicals. In this research, the reactions of 1,4-dioxane with Cl-related radicals and 1,4-dioxane direct photolysis by UV and VUV light were both omitted from the model; 1,4-dioxane was assumed to react only with OH radical. The order of the extent of suppression of 1,4-dioxane degradation per mole was nitrite >> bicarbonate > chloride.

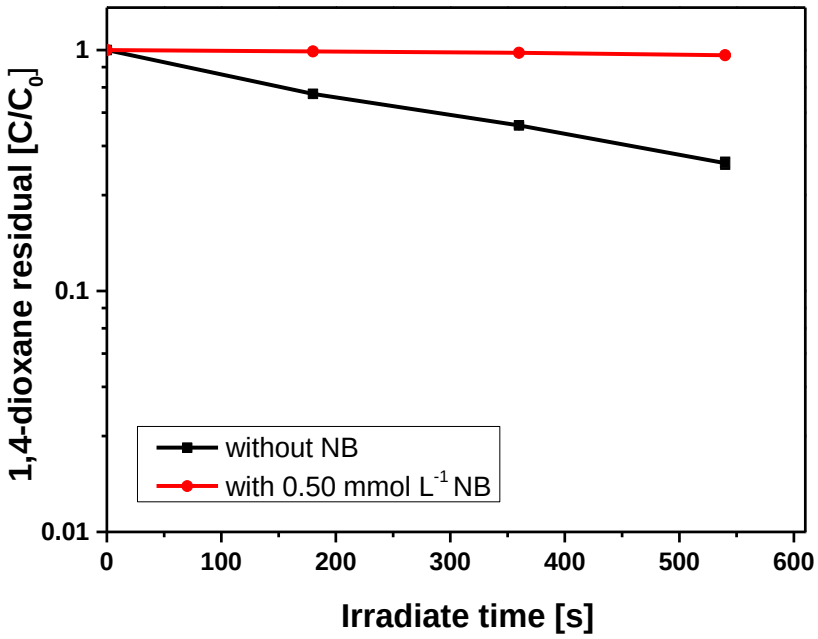

Fig. 2-7 Complete suppression of 1,4-dioxane decomposition during VUV irradiation by adding OH radical scavenger (nitrobenzene, 0.50 mmol·L^{-1}).

2.4.2 Model verification and validation

The validation experiments were conducted in the quasi-collimated beam radiation reactor. The effect of pH and self-ionization of water were validated by comparing the degradation in Milli-Q water and phosphate-buffered Milli-Q (PB). Synthetic water (SW, Table 2-1) and PB were compared to validate the effects of carbonate/bicarbonate. $DTW_{buffered}$ in this experiment was prepared by adjusting the pH and alkalinity of DTW using NaOH and $NaHCO_3$ to match those values of the GW3, to validate the effects of chloride (by comparing SW and DTW) and nitrate (by comparing GW3 and $DTW_{buffered}$). The kinetic model successfully predicted the degradation of 1,4-dioxane for all waters tested in the in-situ degradation experiments (**Fig. 2-8**).

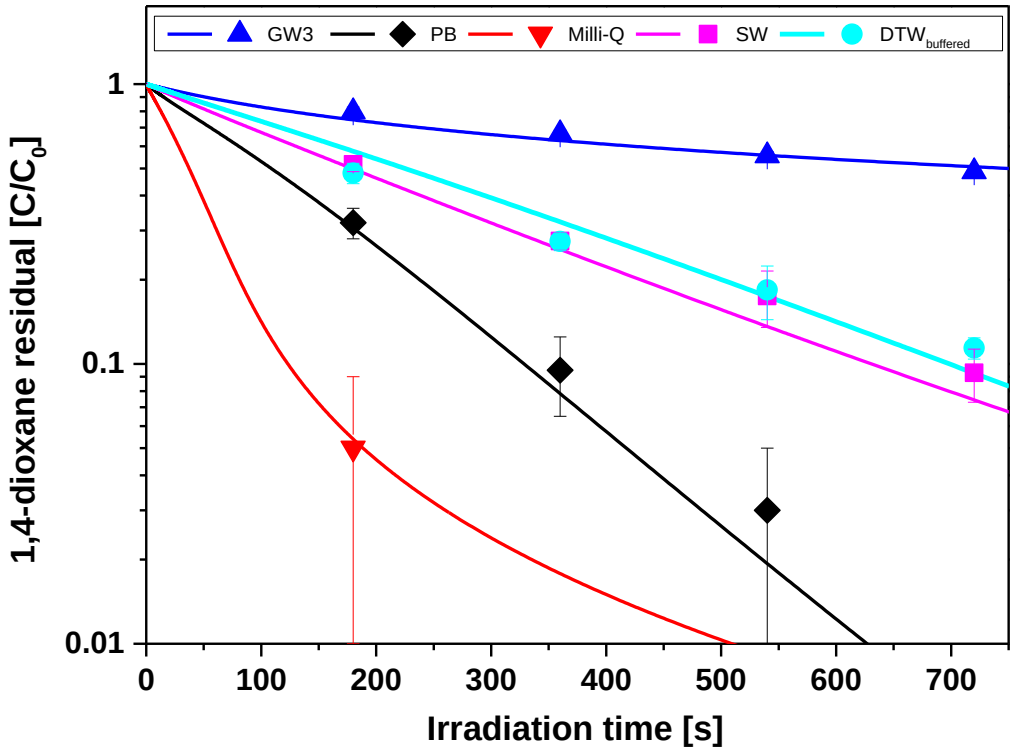

Fig. 2-8 Comparison of predicted (lines) and experimental (scatters) 1,4-dioxane degradation in the quasi-collimated beam radiation reactor for Milli-Q. phosphate-buffered Milli-Q (PB), synthetic-water(SW), buffered dechlorinated tap water ($DTW_{buffered}$), and natural groundwater (GW3).

The results clearly showed that the kinetic model developed in this research was able to describe the effects of all the influential inorganic ions (discussed in 2.4.1) and NOM on the reactions expected during VUV treatment and that the kinetic model could successfully predict 1,4-dioxane degradation in the waters containing different concentrations of inorganic ions.

2.4.3 Model prediction in flow-through photoreactor

To preliminary test whether the kinetic model could be correctly applied to the particles in the Lagrangian approach after adding the information of the hydrodynamics and radiation field, the model was applied to predict 1,4-dioxane degradation in the flow-through photoreactor as the procedure described in **Section 2.2.3**. Experiments were conducted in the flow-through photoreactor using naturally contaminated groundwaters (GW1~3) and the river water artificially supplemented with 1,4-dioxane (RW). The water flowing through the reactor was assumed to be a particle irradiated in the zones (**Fig. 2-3**), and the overall hydrodynamics and radiation field effects were induced by VUV and UV dose, which were determined by chemical actinometry according to the methods described by Heit et al. (1998) and Rahn (1997), respectively.

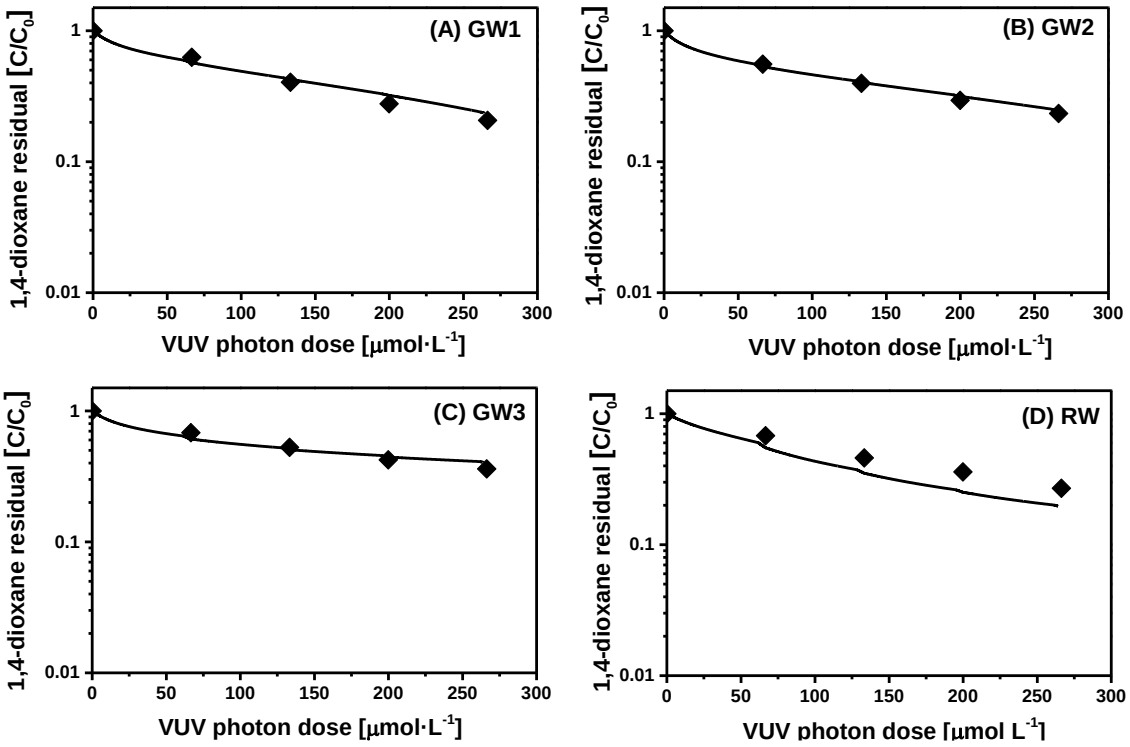

Fig. 2-9 Prediction of 1,4-dioxane degradation in real groundwater (GW1~3) and river water (RW) during the VUV processes in the flow-through photoreactor. Symbols and lines represent observed and predicted values, respectively.

The model simulation successfully predicted the behavior of 1,4-dioxane as a function of VUV dose for all the groundwaters tested (**Fig. 2-9** (A)~(C)). The results clearly showed that the kinetic model developed in this research was able to predict the 1,4-dioxane degradation during

the VUV process—whether in-situ or flow-through—and that the model could successfully describe the effects of inorganic ions in different raw waters on 1,4-dioxane degradation. However, the model overestimated the degradation of 1,4-dioxane in RW. The concentration of DOC in RW was more than one order of magnitude larger than those in the other waters (Table 1). NOM has been reported to reduce the degradation of OMPs by VUV irradiation (Imoberdorf and Mohseni, 2012; Kutschera et al., 2009; Wols and Hofman-Caris, 2012b), although the model included the simplified reaction about NOM (Eq. 23) with reaction rate constant referenced the literature value (Westerhoff et al., 2007), the obtained value in **Section 2.4.2** may low than the actual value in RW. After adjusting the reaction rate constant of Eq. 23 from 1.7×10^4 L·(mg-carbon)$^{-1}$·s^{-1} to 7.5×10^4 L·(mg-carbon)$^{-1}$·s^{-1}, the predicted value for the RW matched the experimental value (**Fig. 2-10**).

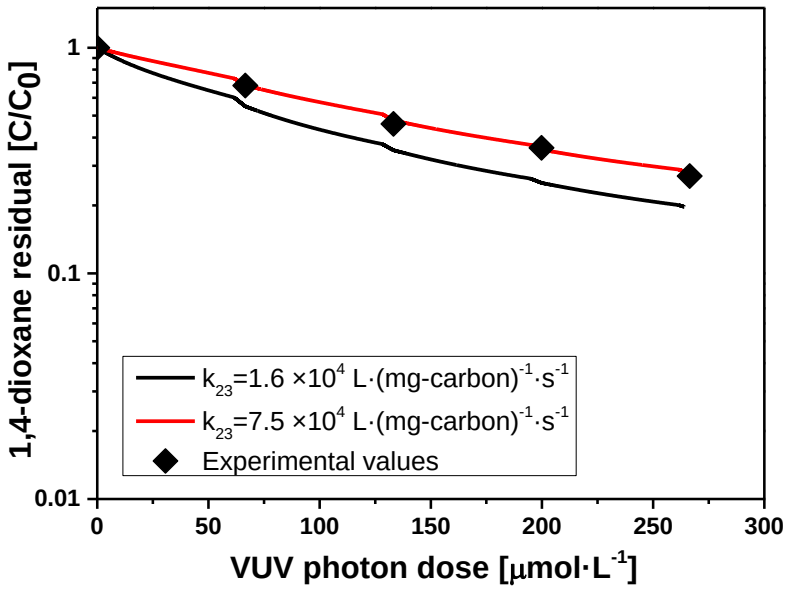

Fig. 2-10 Prediction of 1,4-dioxane degradation in river water (RW) with different reaction rate constant of Eq. 23. Symbols and lines represent observed and predicted values, respectively.

The reaction rate constant of Eq.23 (k_{23}) varies with the exact NOM presented in the water, and the value is generally different for different raw waters. Currently, the original model was able to predict in water that containing very low DOC (such as GW1~3, DTW-based waters, and SW). For high DOC water (such as RW), k_{23} needs to be adjusted based on the original model. To better use the model, a database may need to establish to store the information of the raw water that has been applied to the model, so that when the model is applied to new raw water, a reasonable range of k_{23} can be gotten refer to the database. Since the 1,4-dioxane mainly

pollutes groundwater rather than surface water, and the subsequent chapters mainly use GW3 as the typical contaminated natural groundwater, so the original model was still used in the subsequent discussions.

2.4.4 Sensitivity analysis of the kinetic model

To reduce the usage of the computational resources in the subsequent CFD model, sensitivity analysis was conduct for GW3 (**Fig. 2-11**, Y-axes represent the elementary reaction number in Table 2-2). The suppression of 1,4-dioxane was mostly affected by the scavenging reaction between OH radical and nitrite (Eq. 69, **Fig. 2-9 (**B)), which is also suggested by the experiment result in 2.4.1. Reactions of OH radical with HCO_3^- and CO_3^{2-} (Eq. 49 and 48) were also affected but was one order of magnitude smaller than nitrite. In GW3, chloride showed the suppressing effect on the degradation of 1,4-dioxane by competitive consumption of OH radicals (Eq. 16) but is negligible compared with nitrite, HCO_3^- and CO_3^{2-}.

The reactions which error less than 10^{-7} μmol·L^{-1} (less than around 10^{-6} of the most significant reaction) could be eliminated from the model since the single-precision versions of ANSYS® FLUENT (CFD software used in this research) retain 7 digits (ANSYS FLUENT User's Guide), these errors will be discarded as truncation error. After eliminated the reactions (Eq.16, 18 reverse, 20 reverse, 27, 29, 30, 32, 33, 36, 39, 40, 41, 43, 44, 46, 57, 58, 59, 67, 68, and 73) with relative errors (the ratio of error of the elementary reaction to the error of the most significant elementary reaction) less than 10^{-6}, no significant difference was induce compared with the original model (**Fig. 12** blue and red lines). For the calculation with low precision requirements, more reactions (Eq. 3, 8, 11 reverse, 20, 31, 35, 38, 42, 45, 50, 55, 56, 60, 61, 62, 64, 65, 72, and 74) that the relative error was less than 10^{-3} could be eliminated to reduce the usage of the computational resources.

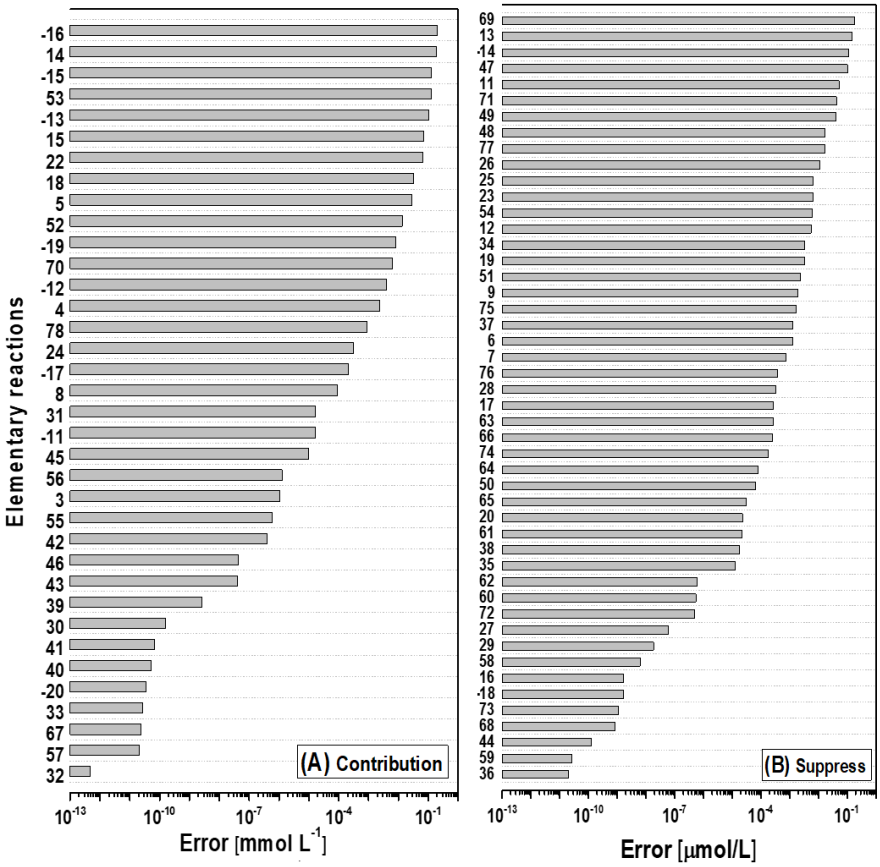

Fig. 2-11 Kinetic constant ordered from most significant to least significant according to sensitivity analysis for the GW3 reaction that (A) contributes to 1,4-dioxane degradation, and (B) suppresses to 1,4-dioxane degradation.

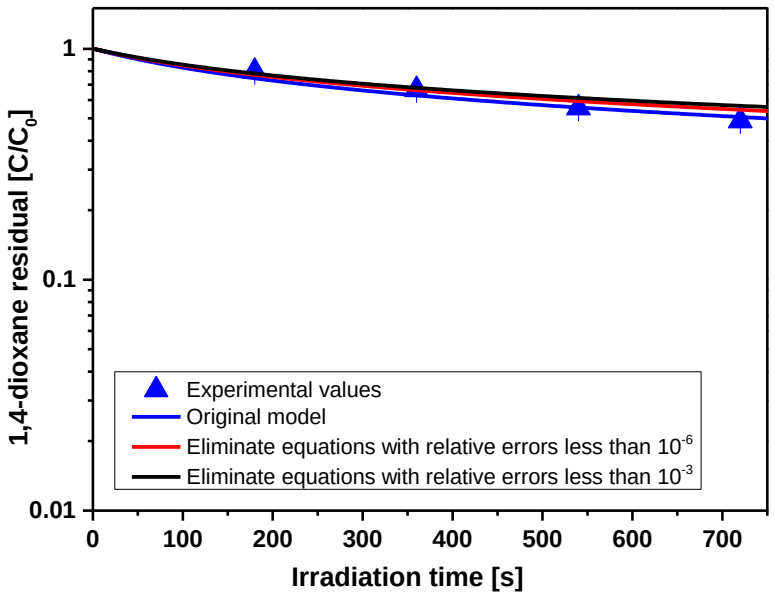

Fig. 2-12 Prediction of 1,4-dioxane degradation in GW3 with/without eliminating unimportant reactions. Symbols and lines represent observed and predicted values, respectively.

2.5 Conclusions

1. Degradation of 1,4-dioxane during VUV treatment is suppressed by inorganic ions (i.e. carbonate/bicarbonate, chloride, and nitrate) ubiquitously found in natural groundwaters. Carbonate/bicarbonate and chloride directly suppress the degradation of 1,4-dioxane, whereas nitrate becomes influential after it is transformed into nitrite during the VUV process. The order of the extent of suppression per mole is nitrite >> bicarbonate > chloride.

2. A kinetic model for 1,4-dioxane degradation during the VUV process that takes into account the effect of inorganic ions and NOM was successfully developed and validated against different water qualities in batch mode degradation experiments.

3. By combining the chemical actinometry method, the model successfully predicted the 1,4-dioxane degradation in actual groundwater in a flow-through VUV photoreactor. This result demonstrated that the model was accurate enough to predict the 1,4-dioxane degradation during VUV treatment of contaminated waters, and can be incorporated into the Lagrangian approach for the CFD model.

4. The kinetic model was simplified based on the sensitivity analysis to reduce its computation resource in a further application to the CFD model.

2.6 Reference

Alapi, T., Dombi, A., 2007. Comparative study of the UV and UV/VUV-induced photolysis of phenol in aqueous solution. Journal of Photochemistry and Photobiology A: Chemistry 188, 409–418.

Bagheri, M., Mohseni, M., 2017. Pilot-scale treatment of 1,4-dioxane contaminated waters using 185 nm radiation: Experimental and CFD modeling. Journal of Water Process Engineering 19, 185–192.

Bagheri, M., Mohseni, M., 2015. A study of enhanced performance of VUV/UV process for the degradation of micropollutants from contaminated water. Journal of Hazardous Materials 294, 1–8.

Bagheri, M., Mohseni, M., 2014. Computational fluid dynamics (CFD) modeling of VUV/UV photoreactors for water treatment. Chemical Engineering Journal 256, 51–60.

Bayliss, N.S., Bucat, R.B., 1975. The photolysis of aqueous nitrate solutions. Australian Journal of Chemistry 28, 1865–1878.

Bolton, J.R., Stefan, M.I., 2002. Fundamental photochemical approach to the concepts of fluence (UV dose) and electrical energy efficiency in photochemical degradation reactions. Research on Chemical Intermediates 28, 857–870.

Buxton, G. V., Bydder, M., Salmon, G.A., 1998. Reactivity of chlorine atoms in aqueous solution: Part 1. The equilibrium Cl. + Cl- ⇌ Cl2.-. Journal of the Chemical Society - Faraday Transactions 94, 653–657.

Buxton, G. V., Greenstock, C.L., Helman, W.P., Ross, A.B., 1988. Critical Review of rate constants for reactions of hydrated electrons, hydrogen atoms and hydroxyl radicals (·OH/·O− in Aqueous Solution. Journal of Physical and Chemical Reference Data 17, 513–886.

Crapulli, F., Santoro, D., Sasges, M.R., Ray, A.K., 2014. Mechanistic modeling of vacuum UV advanced oxidation process in an annular photoreactor. Water Research 64, 209–225.

Crittenden, J.C., Hu, S., Hand, D.W., Green, S.A., 1999. A kinetic model for H2O2/UV process in a completely mixed batch reactor. Water Research 33, 2315–2328.

Dainton, F., Fowles, P., 1965. The photolysis of aqueous systems at 1849 Å II. Solutions containing Cl - , Br - , SO 2- 4 or OH - ions. Proceedings of the Royal Society of London. Series A. Mathematical and Physical Sciences 287, 312–327.

Fang, J., Fu, Y., Shang, C., 2014. The roles of reactive species in micropollutant degradation in the UV/free chlorine system. Environmental Science and Technology 48, 1859–1868.

Furatian, L., Mohseni, M., 2018. Influence of chloride on the 185 nm advanced oxidation process. Chemosphere 199, 263–268.

Gonzalez, M.C., Braun, A.M., 1995. VUV photolysis of aqueous solutions of nitrate and nitrite. Research on Chemical Intermediates 21, 837–859.

Gonzalez, M.G., Oliveros, E., Wörner, M., Braun, A.M., 2004. Vacuum-ultraviolet photolysis of aqueous reaction systems. Journal of Photochemistry and Photobiology C: Photochemistry Reviews 5, 225–246.

Guo, K., Wu, Z., Shang, C., Yao, B., Hou, S., Yang, X., Song, W., Fang, J., 2017. Radical Chemistry and Structural Relationships of PPCP Degradation by UV/Chlorine Treatment in Simulated Drinking Water. Environmental Science and Technology 51, 10431–10439.

Heit, G., Neuner, A., Saugy, P.Y., Braun, A.M., 1998. Vacuum-UV (172 nm) actinometry. The quantum yield of the photolysis of water. Journal of Physical Chemistry A 102, 5551–5561.

Imoberdorf, G., Mohseni, M., 2012. Kinetic study and modeling of the vacuum-UV photoinduced degradation of 2,4-D. Chemical Engineering Journal 187, 114–122.

2.6 Reference

Imoberdorf, G., Mohseni, M., 2011. Degradation of natural organic matter in surface water using vacuum-UV irradiation. Journal of Hazardous Materials 186, 240–246.

Kutschera, K., Börnick, H., Worch, E., 2009. Photoinitiated oxidation of geosmin and 2-methylisoborneol by irradiation with 254 nm and 185 nm UV light. Water Research 43, 2224–2232.

Li, W., Jain, T., Ishida, K., Liu, H., 2017. A mechanistic understanding of the degradation of trace organic contaminants by UV/hydrogen peroxide, UV/persulfate and UV/free chlorine for water reuse. Environmental Science: Water Research and Technology 3, 128–138.

Mack, J., Bolton, J.R., 1999. Photochemistry of nitrite and nitrate in aqueous solution: A review. Journal of Photochemistry and Photobiology A: Chemistry 128, 1–13.

Matsushita, T., Hirai, S., Ishikawa, T., Matsui, Y., Shirasaki, N., 2015. Decomposition of 1,4-dioxane by vacuum ultraviolet irradiation: Study of economic feasibility and by-product formation. Process Safety and Environmental Protection 94, 528–541.

Matthew, B.M., Anastasio, C., 2006. A chemical probe technique for the determination of reactive halogen species in aqueous solution: Part 1 - Bromide solutions. Atmospheric Chemistry and Physics 6, 2423–2437.

Mazellier, P., Busset, C., Delmont, A., De Laat, J., 2007. A comparison of fenuron degradation by hydroxyl and carbonate radicals in aqueous solution. Water Research 41, 4585–4594.

Oppenlander, T., 2007. Process Engineering and Reactor Concepts, in: Photochemical Purification of Water and Air. John Wiley & Sons, Ltd, pp. 239–277.

Oppenländer, T., 2007. Photochemical purification of water and air: advanced oxidation processes (AOPs)-principles, reaction mechanisms, reactor concepts. John Wiley & Sons.

Patton, S., Li, W., Couch, K.D., Mezyk, S.P., Ishida, K.P., Liu, H., 2017. Impact of the ultraviolet photolysis of monochloramine on 1,4-dioxane removal: New insights into potable water reuse. Environmental Science and Technology Letters 4, 26–30.

Rahn, R.O., 1997. Potassium Iodide as a Chemical Actinometer for 254 nm Radiation: Use of Iodate as an Electron Scavenger. Photochemistry and Photobiology 66, 450–455.

Sehested, K., Holcman, J., Hart, E.J., 1983. Rate constants and products of the reactions of e-aq, dioxide(1-) (O2-) and proton with ozone in aqueous solutions. The Journal of Physical Chemistry 87, 1951–1954.

Shirayama, H., Tohezo, Y., Taguchi, S., 2001. Photodegradation of chlorinated hydrocarbons in the presence and absence of dissolved oxygen in water. Water Research 35, 1941–1950.

Siamak, E., Fariborz, T., 2010. Simulation of UV photoreactor for degradation of chemical contaminants: Model development and evaluation. Environmental Science and Technology 44, 2056–2063.

Watts, M.J., Linden, K.G., 2007. Chlorine photolysis and subsequent OH radical production during UV treatment of chlorinated water. Water Research 41, 2871–2878.

Weeks, J.L., Meaburn, G.M., Gordon, S., 1963. Absorption coefficients of liquid water and aqueous solutions in the far ultraviolet. Radiation research 19, 559–567.

Westerhoff, P., Mezyk, S.P., Cooper, W.J., Minakata, D., 2007. Electron pulse radiolysis determination of hydroxyl radical rate constants with Suwannee river fulvic acid and other dissolved organic matter isolates. Environmental Science and Technology 41, 4640–4646.

Wols, B.A., Harmsen, D.J.H., van Remmen, T., Beerendonk, E.F., Hofman-Caris, C.H.M., 2015. Design aspects of UV/H2O2 reactors. Chemical Engineering Science 137, 712–721.

Wols, B.A., Hofman-Caris, C.H.M., 2012a. Modelling micropollutant degradation in UV/H 2O 2 systems: Lagrangian versus Eulerian method. Chemical Engineering Journal 210, 289–297.

Wols, B.A., Hofman-Caris, C.H.M., 2012b. Review of photochemical reaction constants of organic micropollutants required for UV advanced oxidation processes in water. Water Research 46, 2815–2827.

Zeng, Q., Dong, H., Wang, X., Yu, T., Cui, W., 2017. Degradation of 1, 4-dioxane by hydroxyl radicals produced from clay minerals. Journal of Hazardous Materials 331, 88–98.

Zoschke, K., Börnick, H., Worch, E., 2014. Vacuum-UV radiation at 185nm in water treatment - A review. Water Research 52, 131–145.

Zvereva, G.N., 2010. Investigation of water decomposition by vacuum ultraviolet radiation. Optics and Spectroscopy 108, 915–922.

Chapter 3. The effects of flow rate and radiation exitance on the performance of VUV photoreactor - CFD model analysis

3.1 Chapter introduction

For a given photoreactor of the VUV process, an optimized model for its operating conditions allows us to obtain the full benefit of the photoreactors and contribute to implementation (Bagheri and Mohseni, 2015; Imoberdorf and Mohseni, 2012; Xie et al., 2018). Researches in UV processes have shown that flow rate and radiant exitance (changed by sleeve and lamp) are the operating conditions that have significant effects on photoreactor performance (Siamak and Fariborz, 2010; Wols et al., 2015). Accordingly, a CFD model that systematically optimizes the flow rate and VUV radiant exitance is required for the VUV process implementation.

In **Chapter 2**, a kinetic model for 1,4-dioxane degradation during the VUV process that takes into account the effect of inorganic ions and NOM was successfully developed. The model works well on the prediction of 1,4-dioxane degradation in batch mode (in-situ) experiments. After incorporating the overall hydrodynamics and radiation flow field information obtained by the chemical actinnmetry method (Heit et al., 1998; Rahn, 1997) in a flow-through photoreactor, the kinetic model successfully predicted the 1,4-dioxane degradation in actual source waters by the photoreactor, which indicated that the kinetic model could be correctly applied to the Lagrangian approach in the CFD model. Compare with the chemical actinnmetry method used in the **Chapter 2** which limited the kinetic model prediction for the given VUV photoreactor must under a given operating condition as the irradiation measured, the CFD model incorporated with the kinetic model can predict the degradation under different operating conditions by simulations.

Based on the above, the main objective of this chapter was to develop a CFD model to systematically investigate the effect of the operating conditions of a given VUV photoreactor for 1,4-dioxane degradation, and work out the general solutions for operating condition optimization that contribute to the practical implementation of VUV process.

The degradation of 1,4-dioxane highly depended on the water quality as discussed in **Chapter 2**. To take into account the effect of water quality, the whole kinetic model should be incorporated into the CFD model according to the original modeling plan. However, the CFD model built by the original plan took up a lot of computer memory in calculating species concentration change in each time-step for all the particles, and the workstation used in the present research cannot provide this computational resource even after excluding the reactions that the relative error was less than 10^{-3} (**Chapter 2 Section 2.4.4**). Accordingly, the kinetic model was simplified and assumed to be a pseudo-first-order degradation constant depending on the water quality, which could be calculated by the kinetic model through simulation or directly obtained from a simple batch mode experiment with the water to be treated using the quasi-collimated beam apparatus, to reduce the computational resource usage. In this chapter, the pseudo-first-order degradation rate constants were obtained from batch mode experiments.

Then the CFD model was built by the pseudo-first-order degradation rate constant and Lagrangian particle-tracking approach. A series of experiments were conducted using a pilot-scale flow-through annular photoreactor to verify and validate the effects of flow rate and radiant exitance on 1,4-dioxane degradation for the CFD model. Second, simulations were set up in a virtual annular photoreactor by the validated model to systematically investigate the general conclusion on operating conditions optimization. The effects of flow rate and radiant exitance were examined by the simulated results. Radiation efficiency, which was defined as the ratio of the logarithmic residual to the theoretical minimum logarithmic residual (best possible performance) under the given condition, was calculated as an energy-based index of cost-effectiveness.

3.2 Experimental set-up and procedures

3.2.1 Chemicals and water samples

All chemicals were purchased commercially and used without further purification. Reagent solutions for the experiments were prepared with guaranteed reagent grade chemicals and Milli-Q water (18.2 MΩ·cm, Milli-Q Advantage, Millipore Co., Bedford, MA, USA). Two types of water were used for the experiments: actual groundwater (GW3, **Table 2-1**) and dechlorinated tap water (DTW, **Table 2-1**) adjusting the pH and alkalinity using NaOH and $NaHCO_3$ to match those values of the GW3, and then spiked with 100 $\mu g \cdot L^{-1}$ of 1,4-dioxane before use (DTW_{buffer}). Analytical methods were the same as described in **Chapter 2 Section 2.2.4**.

3.2.2 Batch experiment for determining reaction rate constant

The quasi-collimated beam VUV apparatus described in **Chapter 2 Section 2.2.3** was used to determine the pseudo-first-order degradation rate constant for 1,4-dioxane in GW3 and DTW_{buffer} for the CFD model. The pseudo-first-order degradation rate constant was determined for the waters from the ratio of and the slope of the relationship of the natural logarithm of the residual ratio against the mean VUV dose, assuming that the irradiation was uniform because of stirring (Bolton and Stefan, 2002).

3.2.3 Pilot-scale experiment for model validation

Experiments were conducted using a pilot-scale flow-through VUV photoreactor made of stainless steel (**Fig. 3-1**). The internal radius of the reactor and the external radius of the quartz sleeve were 23.9 and 11.5 mm, respectively, resulting in a radial gap of 12.4 mm, which corresponded to a hydraulic diameter of 24.8 mm for the water flowing through the reactor. To provide a large range of radiation exitance and investigate its effect in the pilot-scale photoreactor, two types of low-pressure mercury lamps (65 and 240 W, Heraeus Noblelight GmbH, Hanau, Germany) and two types of quartz sleeves with different VUV radiation transmittance were used. To mimic lower-power lamps, a 65-W lamp was coated with a synthetic fluororesin film reducing the VUV radiation exitance (Iwasaki Electric Co., Ltd., Tokyo, Japan). The lamps provided a 1.4-m-long cylindrical radiation zone within the 1.6-m photoreactor. The stable VUV and UV photon emissions on the external surface of the quartz sleeve were measured for each lamp (**Table 3-1**) by the same radiometer use in **Chapter 2 Section 2.2.3**.

Table 3-1 Lamp and quartz sleeves used in this chapter.

low-pressure mercury lamp	Quartz sleeve	VUV exitance on the external surface of the quartz sleeve ($W \cdot m^{-2}$)	
		185 nm	254 nm
240W	Low transmittance	60.1±1.3	497±31
65W		25.6±1.8	229±8
65W with coating		7.3±0.9	161±14
240W	High transmittance	105±4.0	548±27
65W		40.3±2.2	247±9
65W with coating		13.9±1.2	173±16

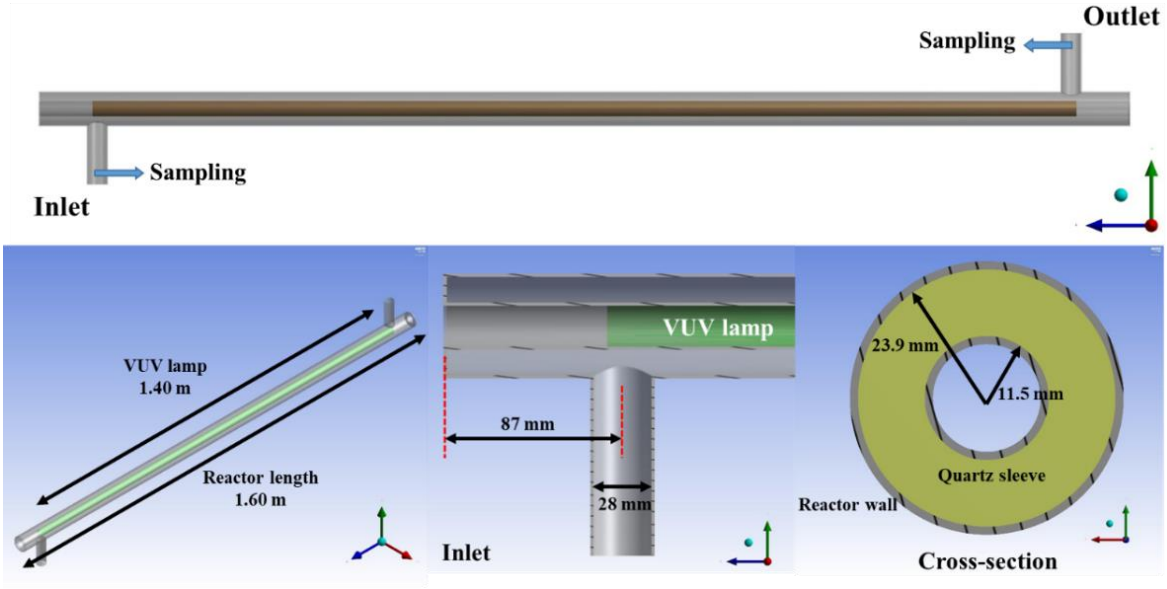

Fig. 3-1 Schematic of the pilot-scale flow-through annular photoreactor.

To validate the model with the respect to the effect of flow rate on 1,4-dioxane degradation, flow-through experiments were conducted with the photoreactor equipped with the 240-W lamp at room temperature using GW3 at flow rates ranging from 1.5 to 10.5 L • min^{-1}. To validate the model concerning the effect of radiant exitance on 1,4-dioxane degradation, similar experiments were conducted with the photoreactor equipped with different lamps and different quartz sleeves (**Table 3-1**) at room temperature using DTW_{buffer} at a flow rate of 6.9 L·min^{-1}. Samples were withdrawn from the sampling points at the inlet and the outlet, and the concentrations of 1,4-dioxane in the samples were measured.

3.3 CFD modeling

3.3.1 CFD model set up

On the first trial to build the CFD model, the original kinetic model and simplified model discussed in **Chapter 2 Section 2.4.4** were compiled into the program, respectively, but both of them were resulted in out of memory. Therefore further simplified method is required in this research. Based on the profile of the kinetic model in **Chapter 2**, the concentration of OH radical significantly increased at irradiation begins and then tended to be stable within a certain range (**Fig. 3-2**), which was determined by the water quality.

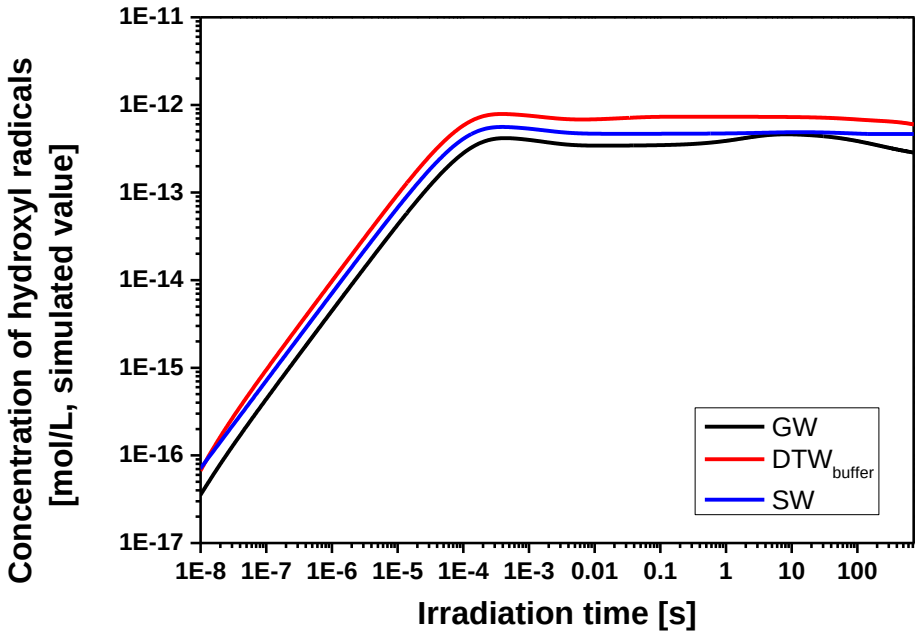

Fig. 3-2 Simulated concentration of hydroxyl radical in the quasi-collimated beam radiation reactor for synthetic-water(SW), buffered dechlorinated tap water (DTW_{buffer}), and natural groundwater (GW3).

This result showed in **Fig. 3-2** agreed with the previous research (De Laat et al., 1999; Sharpless and Linden, 2003). Therefore, the OH radical was at a steady-state in the majority of reaction time, and the equilibrium concentration of the OH radicals ($C_{OH,\,st}$) can be calculated using

$$C_{OH,\,st} = \frac{\Phi_1+\Phi_2}{\sum(k_i \cdot C_i)} \cdot \frac{I}{N_A E_{185}} \tag{3-1}$$

where k_i is the rate constant for the reaction between OH-radical-consuming species i and OH radicals, C_i is the concentration of OH-radical-consuming species i, I is the VUV fluence rate, E_{185} is the energy of a photon, and N_A is Avogadro's constant. The factor k_iC_i describes the reactions of all of the OH-radical-consuming species in the water. Since the equations for the reactions of each species were individually solved in the kinetic model, resulting in a steady state of OH radicals, these reactions can be treated as an overall reaction with a certain rate constant (Wols et al., 2011). Accordingly, the coefficient of I is a constant determined by the background species present in the water (water quality):

$$C_{OH,\,st} = K \cdot I \tag{3-2}$$

then gives the following expression for the rate of 1,4-dioxane degradation:

$$R_d = -k_{OH} \cdot C_{OH,\,st} \cdot C = -k_{OH} \cdot K \cdot I \cdot C \quad (3\text{-}3)$$

According to this equation, a simple relationship was established between VUV irradiation and 1,4-dioxane degradation rate, which could be further used for developing the CFD-base model without excessive computing resource consumption.

The Lagrangian particle-tracking approach is appropriate for the prediction of micropollutant degradation by UV treatment (Wols and Hofman-Caris, 2012). In this approach, the term "particle" refers to a small volume of water in which VUV photon-induced reactions take place. The motion of these particles comprises an advection displacement induced by the computed velocity field, and a diffusion displacement induced by turbulent fluctuation. Both the velocity field and the diffusion are calculated by the viscous models provided by CFD software. The VUV dose (D [J·m^{-2}]) experienced by a particle is calculated by integrating the fluence rate over the particle trajectory:

$$D = \int_0^T I(\vec{r}(t))dt \quad (3\text{-}4)$$

where T is irradiation time, and $\vec{r}(t)$ is the position vector along the trajectory. For predicting 1,4-dioxane degradation within a particle, Eq. 3-3 is solved using $I(\vec{r}(t))$ of the particle trajectory from the inlet to the outlet of the reactor. The concentration at the outlet of the reactor (C) calculated using the Lagrangian approach can be simplified by using the initial concentration at the inlet (C_0) and the VUV dose (D) at the outlet:

$$C = C_0 \exp(-kD) \quad (3\text{-}5)$$

The concentration at the outlet ($\bar{C}$) is calculated by using the mass-flow-weighted (w_i weight of particle i, $\sum w_i = 1$) average of the concentration in each fluid particle (C_i) irradiated with the respective VUV dose (D_i) as follows:

$$\bar{C} = \sum(w_i C_i) = \sum(w_i C_0 \exp(-kD_i)) \quad (3\text{-}6)$$

3.3.2 CFD programing

ANSYS® Workbench 2019R was used to build and discretize a 1.6-m-long pilot-scale flow-through VUV photoreactor with an annular configuration. Two viscosity models in ANSYS® Fluent were used: the laminar model was used for Reynolds numbers (*Re*) <2000, and the realizable κ-ε model coupled with standard wall function was used for *Re* ≥2000. The radiation field for VUV photons was computed by solving the radiative transfer equation using a non-gray discrete ordinate sub-model. The VUV inputs are summarized in **Table 3-1**. Using the Lagrangian approach, 4000 evenly distributed particles were released at the inlet. A user-defined function (UDF, **Appendix 2**) was used to record the VUV fluence rate along the trajectory of each particle and to integrate it into the VUV dose. The concentration of 1,4-dioxane in each particle at the outlet was calculated by using Eq. 3-5, and the concentration of 1,4-dioxane in the whole fluid was then calculated by using Eq. 3-6. The computational domain of the photoreactor was divided into 2.5 million cells constituting an unstructured mesh. To guarantee proper resolution of the boundary layer, a 2-mm-layer with 10 layers of inflated prisms was placed close to the sleeve.

To investigate the effect of flow rate and radiant exitance on 1,4-dioxane degradation, a simple virtual annular photoreactor, which is a common photoreactor arrangement, was constructed by using the same model set-up procedure described above (**Fig. 3-3**). The virtual photoreactor had the same cross-section as the pilot-scale flow-through annular photoreactor, although the length was set at 1.0 m and the whole of the photoreactor was assumed to be irradiated. Assuming fully developed laminar or turbulent flow, inlet velocity distributions at different flow rates and a given *Re* were set by using the appropriate profile in ANSYS® Fluent. Radiant exitance was defined as the direct irradiation on the external surface of the quartz sleeve. The computational domain of the photoreactor was divided into 4 million cells constituting a structured hexahedral/prism mesh. To ensure accurate results of hydraulics and radiation, a radial division of 30 uniform elements in the water domain was applied. The axial direction was discretized into a uniform distribution of nodes with an interval of 1.0 mm. Mesh dependency studies indicated that the grid was fine enough to give grid-independent results.

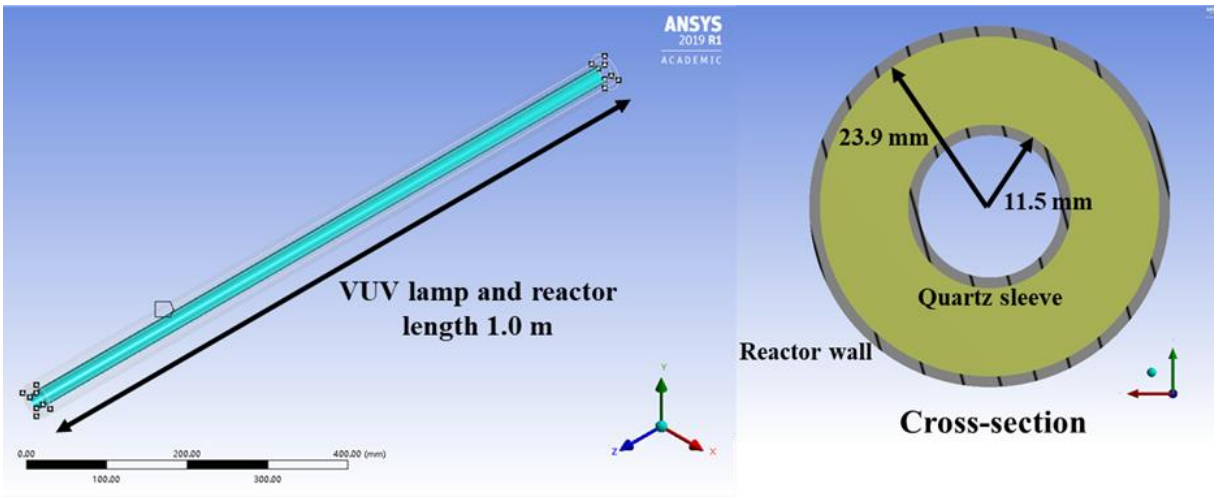

Fig. 3-3 Schematic of the virtual annular photoreactor.

3.4 Evaluation method

3.4.1 Radiation efficiency

According to Jensen's inequality (**Appendix 3**), $\bar{C}$ in Eq. 3-6 has a minimum value $\bar{C}_{min}$ (maximum degradation ratio) at which all the particles receive the same VUV dose $\bar{D}$ (mass-flow-weighted average VUV dose):

$$\bar{C} = \sum (w_i C_0 \exp(-kD_i)) \geq C_0 \exp\left(-k \cdot \sum w_i D_i\right)$$

$$= C_0 \exp(-k\bar{D}) = \bar{C}_{min} \quad (3\text{-}7)$$

In practical terms, $\bar{D}$ can be determined as a function of VUV power input (P_{VUV}), flow rate (Q), VUV absorption coefficient (α), and water layer thickness (h). Since an annular photoreactor is considered an axisymmetric system where the water is flowing parallel to the lamp, the three dimensions (3D) system can be simplified to two dimensions (r-z). In the very limited interval of the z-direction (dz), the instantaneous velocity ($u_z(r)$) in the z-direction and the fluence rate ($I(r)$) are considered to be constant, which means that the VUV dose (dD) in this limited interval of the z-direction can be calculated as:

$$\mathrm{d}D(\mathrm{r}) = I(\mathrm{r}) \cdot \frac{\mathrm{d}z}{u_z(\mathrm{r})} \tag{3-8}$$

Then the mass-flow averaged VUV dose in this limited interval is

$$\Delta\overline{\mathrm{D}} = \frac{\int_0^{2\pi}\int_{\mathrm{r_q}}^{\mathrm{R}} \mathrm{dD(r)}\cdot \mathrm{u_z(r)drd\theta}}{\int_0^{2\pi}\int_{\mathrm{r_q}}^{\mathrm{R}} \mathrm{u_z(r)drd\theta}} = \frac{\int_0^{2\pi}\int_{\mathrm{r_q}}^{\mathrm{R}} \mathrm{dD(r)}\cdot \mathrm{u_z(r)drd\theta}}{\mathrm{Q}} \tag{3-9}$$

where r_q is the external radius of the quart sleeve, R is the internal radius of the photoreactor, and Q is the flow rate. $I(r)$ can be calculated by the Beer-Lambert law:

$$\mathrm{I(r)} = \mathrm{I_0} \cdot \frac{\mathrm{r_q}}{\mathrm{r}} \cdot 10^{-\alpha(\mathrm{r}-\mathrm{r_q})} \tag{3-10}$$

where I_0 is the radiant exitance on the external surface of the quartz sleeve, and α is the absorption coefficient of water calculated by

$$\alpha = \frac{\log_{10}(\mathrm{T_{10,w}})}{0.01\ \mathrm{m}} \tag{3-11}$$

where $T_{w,10}$ is the 10-mm transmittance of water. If L is the length of the VUV lamp, then the mass-flow average VUV dose for the water flow through the photoreactor is

$$\overline{\mathrm{D}} = \int_0^{\mathrm{L}} \frac{\int_0^{2\pi}\int_{\mathrm{r_q}}^{\mathrm{R}} \mathrm{dD(r)}\cdot \mathrm{u(r)drd\theta}}{\mathrm{Q}} = \frac{2\pi \mathrm{r_q L I_0}}{\mathrm{Q}\alpha}\left(1 - 10^{-\alpha(\mathrm{R}-\mathrm{r_q})}\right) \tag{3-12}$$

If $\mathrm{h} = \mathrm{R} - \mathrm{r_q}$ is the thickness of the water layer, $1 - 10^{-\alpha(\mathrm{R}-\mathrm{r_q})}$ is very close to 1, and $2\pi \mathrm{r_q L I_0}$ is the total VUV radiation input from the surface of the quartz sleeve to the system (P_{VUV}), then the mass-flow averaged VUV dose becomes

$$\overline{\mathrm{D}} = \frac{\mathrm{P_{VUV}}}{\mathrm{Q}\alpha} \cdot \left(1 - 10^{-\alpha \mathrm{h}}\right) \approx \frac{\mathrm{P_{VUV}}}{\mathrm{Q}\alpha} \tag{3-13}$$

From a practical point of view, however, it is impossible to achieve $\overline{\mathrm{C}}_{\mathrm{min}}$, because the particles

do not receive a uniform VUV dose. The radiation efficiency (η) as a metric of energy-based efficiency is therefore determined as follows (Wols et al., 2015):

$$\eta \equiv \frac{\ln\left(\frac{C}{C_0}\right)}{\ln\left(\frac{\bar{C}_{min}}{C_0}\right)} = \frac{\ln\left(\frac{C}{C_0}\right)}{-k\bar{D}} = \frac{\ln\left(\frac{C}{C_0}\right)}{-k\cdot\frac{P_{VUV}}{Q\alpha}} \quad (3\text{-}14)$$

where $\ln(C/C_0)$ is the actual log degradation. In this research, radiation efficiency was determined as the ratio of the observed log-degradation to the theoretical maximum achievable log-degradation, which assuming no variation in VUV dose among the particles.

3.4.2 Electrical Energy per Order

In practical applications, Electrical Energy per Order (EEO, $kWh\cdot m^{-3}\cdot order^{-1}$)) has been widely used for comparing cost-effectiveness among advanced oxidation processes and operating conditions (Bolton and Stefan, 2002):

$$EEO = \frac{W_p + P_l}{Q\cdot\log_{10}(C_{in}/C_{out})} \quad (3\text{-}15)$$

where W_p and P_l are the electrical energy input (kW) of the pump and lamp, respectively; Q is the volumetric flow rate ($m^3\cdot h^{-1}$); and C_{in} and C_{out} are concentrations of 1,4-dioxane at the inlet and outlet of the reactor, respectively. The required pump input can be calculated by using (Bagheri and Mohseni, 2015):

$$W_p\ [W] = \frac{Q\ [m^3\cdot s^{-1}]\cdot\Delta P[Pa]}{\epsilon} \quad (3\text{-}16)$$

where Q is the flow rate, ΔP is the pressure loss, and ϵ is the pump electrical efficiency (normally 50%–75%). To determine P_l in the virtual photoreactor, the ratio of VUV radiation output on the surface of the quartz sleeve to VUV lamp electricity input was assumed to be a constant (ε, power conversion efficiency). In the pilot-scale reactor, the external surface of the sleeve can be expressed as:

$$S = 2\pi rL = 0.101\ m^2 \tag{3-17}$$

For the 240-W VUV lamp, the radiation exitance on the sleeve is 105 $W \cdot m^{-2}$, giving a VUV output of

$$P_{VUV} = \gamma \cdot S = 105 \times 0.101\ W = 10.6\ W \tag{3-18}$$

Thus, the power conversion efficiency for the 240-W VUV lamp is

$$\varepsilon = \frac{P_{VUV}}{P_{input}} \times 100\% = \frac{10.6}{240} \times 100\% = 4.4\% \tag{3-19}$$

For the 65-W VUV lamp, the radiation exitance on the sleeve is 40.3 $W \cdot m^{-2}$, giving a VUV output of

$$P_{VUV} = \gamma \cdot S = 40.3 \times 0.101\ W = 4.07\ W \tag{3-20}$$

Thus, the power conversion efficiency for the 65-W VUV lamp is

$$\varepsilon = \frac{P_{VUV}}{P_{input}} \times 100\% = \frac{4.07}{65} \times 100\% = 6.3\% \tag{3-21}$$

Plotting P_{input} on the X-axis and P_{VUV} on the Y-axis and then fitting a straight line through the coordinate origin affords $\varepsilon \approx 4.5\%$ (**Fig. 3-4**).

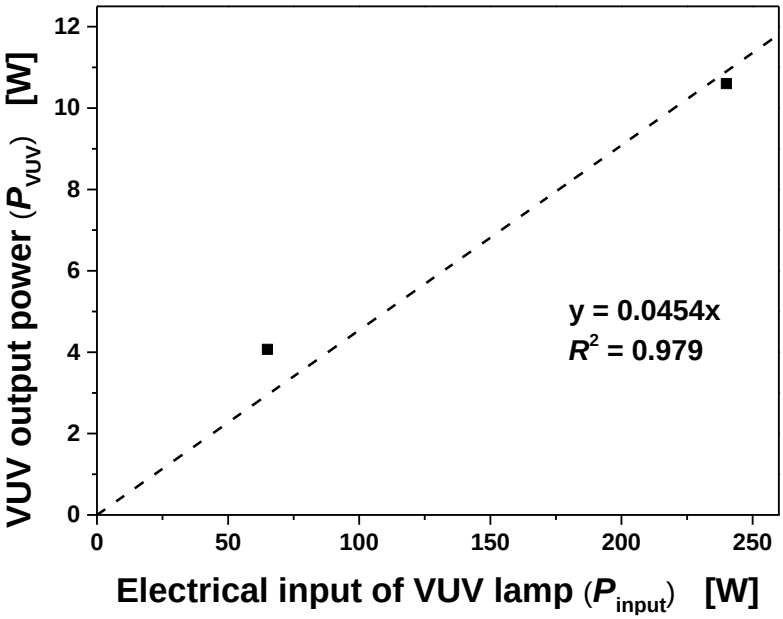

Fig. 3-4 Linear fitting between electrical input and vacuum ultraviolet (VUV) energy output for the VUV lamp.

The VUV radiant exitance (γ) in the simulation and equivalent electrical power input (*P*) were calculated and are shown in **Table 3-2**.

Table 3-2 VUV radiant exitance (γ) in the simulation and equivalent electrical power input (*P*) calculated by using power conversion efficiency of the lamps

γ ($W \cdot m^{-2}$)	20	40	60	80	100
P (W)	31	63	94	126	157

*γ - radiant exitance on the external surface of the sleeve.

3.5 Results and discussion

3.5.1 Determination of degradation rate constant

The pseudo-first-order degradation rate constant was used to simplify the reaction of OH radicals with background OH-radical-consuming species (**Chapter 2 Section 2.3.1**). The pseudo-first-order degradation rate constant of 1,4-dioxane in each water could be calculated

by the kinetic model (**Chapter 2**) through simulation or directly obtained from a simple batch mode experiment with the water to be treated using the quasi-collimated beam apparatus. In this chapter, the pseudo-first-order degradation rate constants were obtained from batch mode experiments described in **Section 3.2.2**. In Milli-Q water (**Fig. 3-5**), 1,4-dioxane rapidly degraded to a residual ratio of approximately 5% at a volume-averaged VUV dose of 100 $J \cdot m^{-2}$. In contrast, at the similar VUV dose absorbed by water, the residual of 1,4dioxane in DTW_{buffer} and GW3 were 0.49 and 0.79, respectively, values which are much higher than that in Milli-Q water, indicating that 1,4-dioxane degradation was suppressed in DTW_{buffer} and GW3 as discussed in **Chapter 2**. The reaction rate constants in DTW_{buffer} and GW3 were determined to be 1.4×10^{-2} and 5.2×10^{-3} $m^2 \cdot J^{-1}$, respectively, and these values were used in the CFD model simulation.

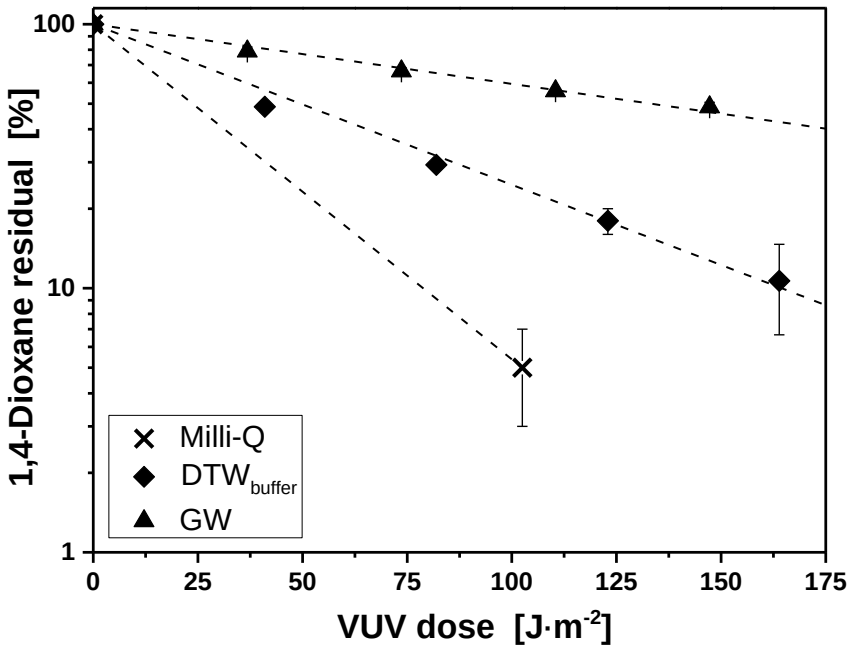

Fig. 3-5 Degradation of 1,4-dioxane in DTW_{buffer} and GW3 in batch experiments using the quasi-collimated beam radiation reactor. Error bars indicate standard deviations of three experiments.

3.5.2 Model validation in a pilot-scale flow-through photoreactor

Two sets of experiments were carried out using the pilot-scale flow-through annular photoreactor: one set using different flow rates (1.5–10.5 $L \cdot min^{-1}$), a radiant exitance of 105

W·m^{-2}, and GW3; and one set using different radiant exitance (7.3–105 W·m^{-2}), a flow rate of 6.96 L·min^{-1}, and DTW_{buffer}.

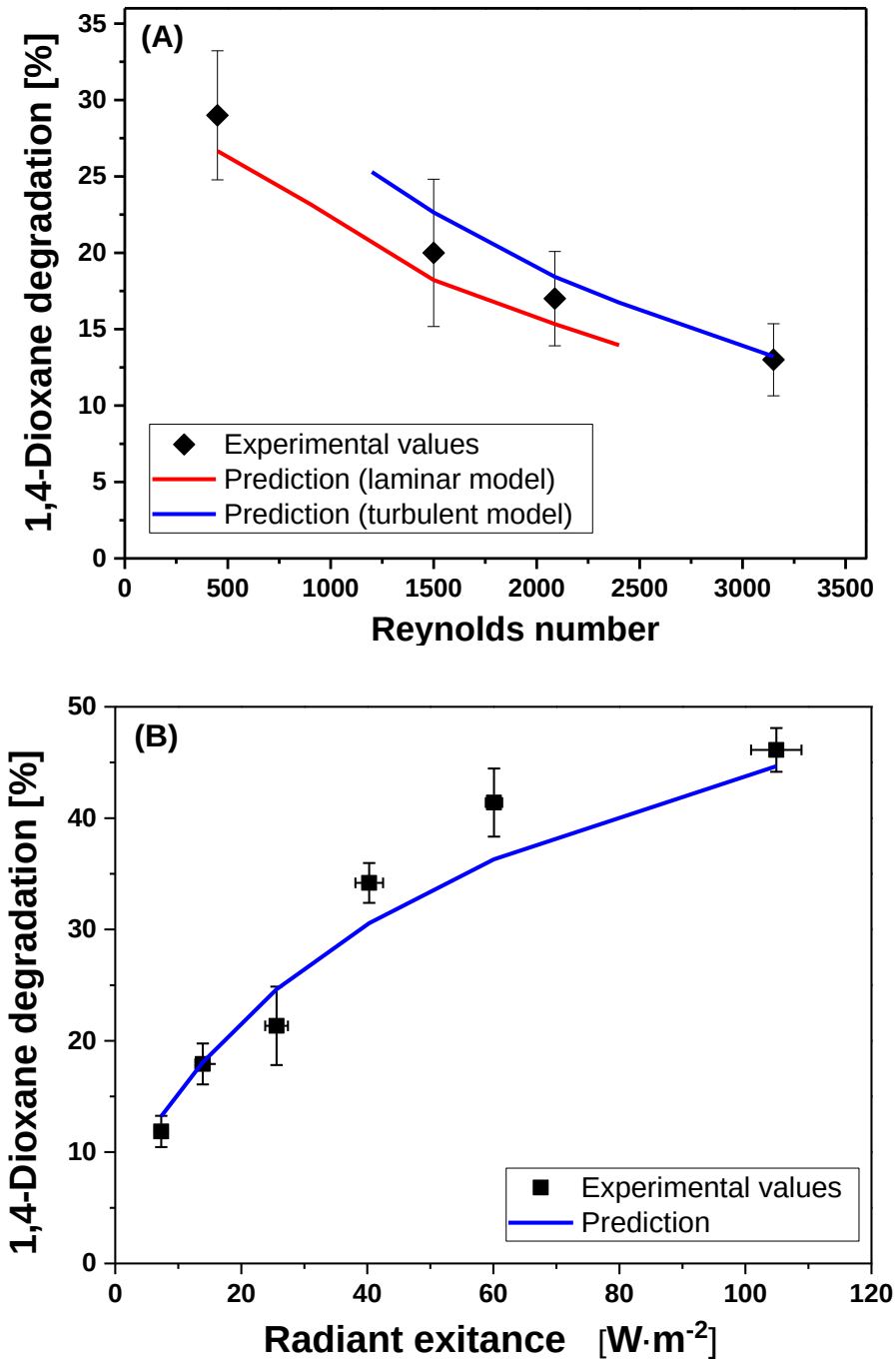

Fig. 3-6 Comparison of predicted and experimental 1,4-dioxane degradation in the pilot-scale flow-through annular photoreactor (A) at different flow rates and a radiant exitance of 105 W·m^{-2} using sampled groundwater and (B) at a flow rate of 6.96 L·m^{-1} (*Re* 2100) at different radiant exitance using synthetic water.

Because laminar-turbulent transitional flow occurs at *Re* values between 1800 and 2800 (Darbyshire and Mullin, 2005), a fully developed laminar or turbulent model may have introduced errors into the result within this *Re* range. However, the laminar model closely predicted the experimental degradation obtained at *Re* smaller than 2000, and the turbulent model closely predicted the experimental degradation at *Re* greater than 2000 (**Fig. 3-6 (**A)). Thus, we excluded the need for any parameter fitting. Likewise, the predicted and experimental values under different radiant exitances were also similar (**Fig. 3-6** (B)). Overall, the model provided degradation ratios that followed the same trend as the experimental data as flow rate (*Re*) and radiant exitance were changed. Thus, we concluded that the model was valid for predicting the effects of flow rate and radiant exitance on 1,4-dioxane degradation in the pilot-scale photoreactor.

Compared with the kinetic model developed in **Chapter 2**, the simplified method of using the pseudo-first-order degradation rate constant for the Lagrangian particles in the CFD model may be relatively coarse. However, the results confirm that the CFD model using the simplified method was able to predict 1,4-dioxane degradation with sufficient engineering accuracy under different flow rates and different radiant exitance.

To ensure the simulation results in the virtual photoreactor were reliable, the Lagrangian approach used in the CFD model was further validated in the virtual photoreactor. The averaged retention time of all the particles ($\frac{1}{n}\sum t_i$) versus the hydraulic retention time ($T = \frac{V}{Q}$), and the average VUV dose of all the particles ($\frac{1}{n}\sum d_i$) versus the mass-flow-weighted average VUV dose (Eq.3-13) of each simulation was compared, respectively. In each group of comparisons, the former one is the simulated values while the latter is the theoretical values at the current operating condition in the virtual photoreactor. Good agreement between the simulation results and the theoretical values confirmed the reliability of the CFD model simulation results in the virtual photoreactor (**Fig. 3-7**).

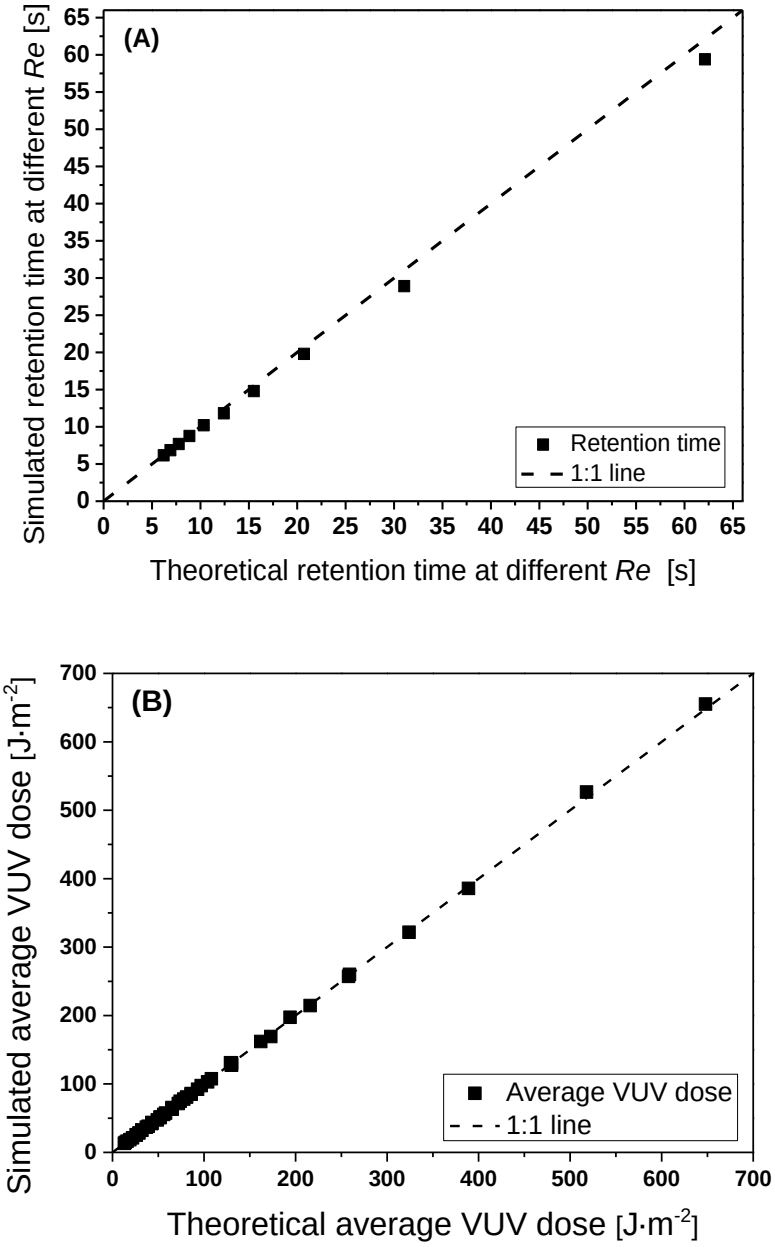

Fig. 3-7 Comparison of simulated and theoretical values of retention time (A) and average vacuum ultraviolet (VUV) dose (B) in the virtual photoreactor. The simulated values were obtained by computational fluid dynamics particle-based simulation.

3.5.3 Effects of flow rate on 1,4-dioxane degradation

To investigate the effect of flow rate on 1,4-dioxane degradation, simulations with different flow rates from laminar to turbulent flow and a fixed radiant exitance of 100 $W \cdot m^{-2}$ using GW3 were set up in the virtual photoreactor. The simulated results of 1,4-dioxane degradation in the

virtual photoreactor followed the same trend as that experimental values obtained in the pilot-scale photoreactor, that is, the degradation ratio of 1,4-dioxane decreased with the increasing flow rate (*Re*) under the same flow regime (**Fig. 3-8**), which was attributed to the retention time of water in the reactor decreasing with increasing flow rate.

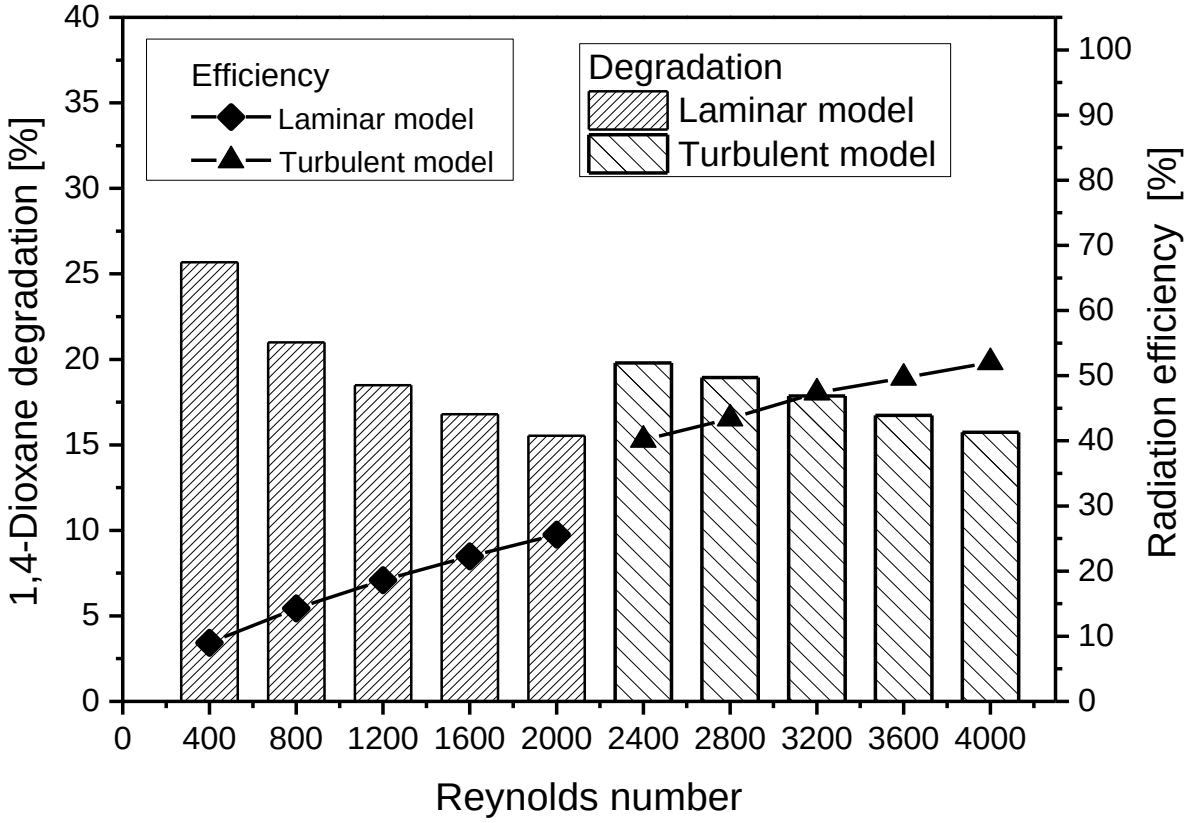

Fig. 3-8 Effect of flow rate (i.e., Reynolds number) on 1,4-dioxane degradation and radiation efficiency in the virtual photoreactor.

In contrast, radiation efficiency was found to increase with increasing flow rate irrespective of flow regime. The VUV radiation field in the photoreactor was non-uniform: the fluence rate decreased exponentially with distance from the lamp; therefore, the VUV dose of each particle varied according to its trajectory. Under laminar flow, because water migrates in parallel layers that do not mix, the VUV fluence rate of the particle does not change along its trajectory. Thus, the VUV dose range of the particles was large (**Fig. 3-9 (**A)) because particles close to the quartz sleeve received high VUV doses (high fluence rate and long retention time), whereas those far from the quartz sleeve received low VUV doses (low fluence rate or short retention time or both). In contrast, under turbulent flow, chaotic changes in pressure and velocity occur

while the particles pass through the photoreactor, resulting in a relatively narrow dose distribution (**Fig. 3-9** (B)).

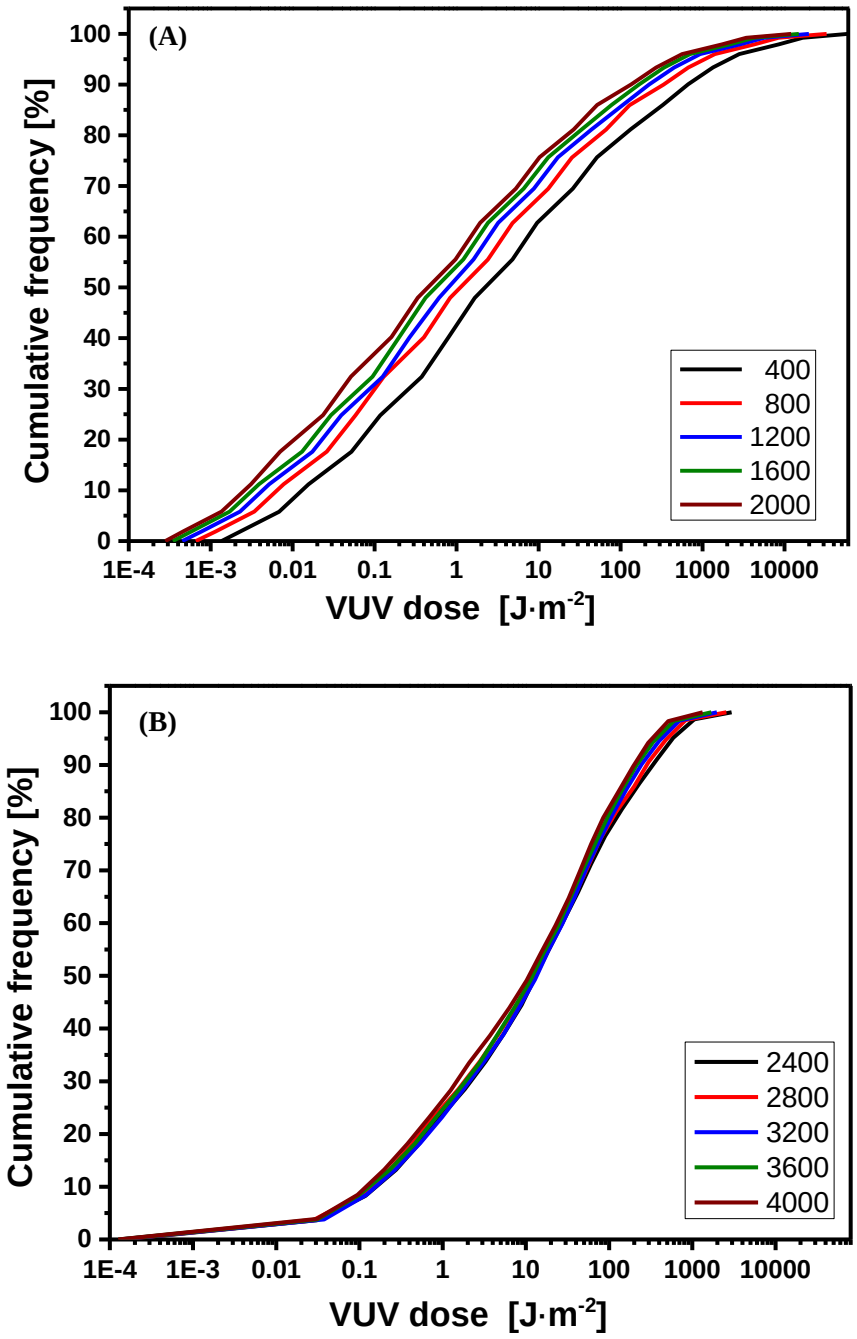

Fig. 3-9 Cumulative vacuum ultraviolet (VUV) dose distribution under laminar flow (A) or turbulent flow (B). The numbers in the legends are Reynolds numbers.

Under both flow regimes, increasing the flow rate (*Re*) did not change the shape of the cumulative VUV dose curve, but did shift it to the left, which means that the VUV doses of all

the particles decreased by the same ratio. These decreases resulted in an increase in radiation efficiency according to Jensen's inequality (**Appendix 3**).

Although the model provided values that showed the same trends as those found in the validation experiments, discontinuous changes in degradation ratio and radiation efficiency were observed as the *Re* was increased from 2000 to 2400. This was attributed to the use of different models for the two flow regimes (laminar model for *Re* ≤2000; turbulent model for *Re* ≥2400). The actual degradation ratio was expected to be between the values predicted by the laminar and the turbulent models in the *Re* range of 1800–2800 because the real flow in this *Re* range was laminar-turbulent transitional flow. Such transitional flow results in more physical modeling uncertainty than does fully developed laminar or turbulent flow (Versteeg and Malalasekera, 2007). To accurately predict the result for every flow rate in this range, high-resolution experiments consisting of several runs at different flow rates and a deep understanding of fluid dynamics for transitional flows would be required. However, this research aim at investigating the changes in degradation ratio and radiation efficiency for optimizing the operating conditions under fully developed laminar or turbulent flow; therefore, this discontinuity is not discussed in detail here.

3.5.4 Effect of radiant exitance on 1,4-dioxane degradation

To investigate the effect of radiant exitance on 1,4-dioxane degradation, simulations using DTW_{buffer} with different radiation exitance (from 20 to 100 $W \cdot m^{-2}$) on the surface of the sleeve in the virtual photoreactor were set up under laminar flow (*Re* 800) and turbulent flow (*Re* 4000), and the results were shown in **Fig. 3-10**.

As the radiant exitance increased, the degradation ratio increased under both flow regimes, which was consistent with the observations of the validation experiments in the pilot-scale photoreactor. These results were attributed to the overall VUV dose absorbed by solution increased because increasing the radiant exitance proportionally increases the VUV fluence rate at every position in the photoreactor.

In contrast, as the radiant exitance increased, the radiation efficiency decreased under both flow regimes. Since increasing the radiant exitance proportionally increases the VUV fluence rate at every position in the photoreactor regardless of flow type, the VUV doses of the particles were

increased by the same ratio along its trajectory as the radiant exitance was increased, resulting in a decrease of radiation efficiency according to Jensen's inequality (**Appendix 3**). VUV dose distribution is the key factor to improving degradation and radiation efficiency.

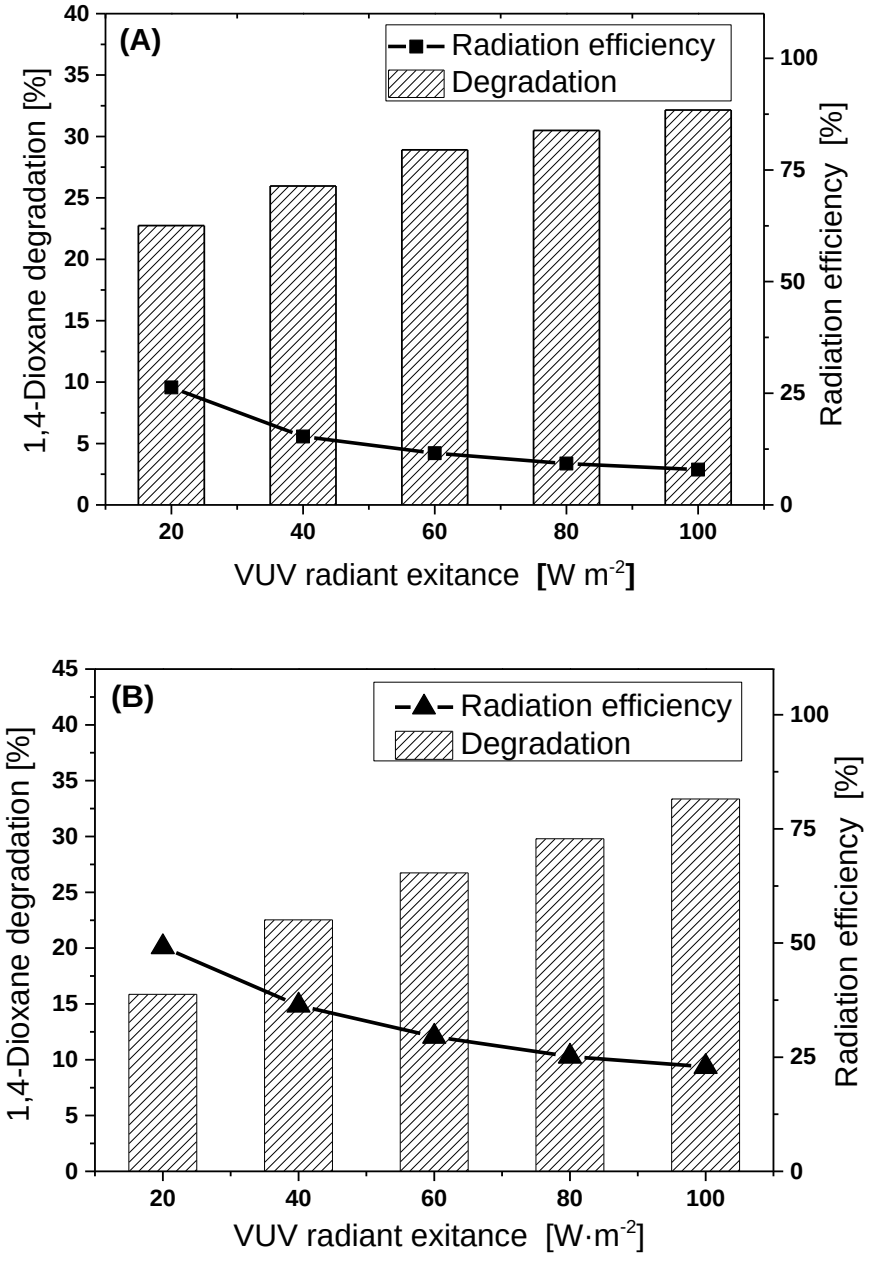

Fig. 3-10 Effect of radiant exitance on 1,4-dioxane degradation ratio and radiation efficiency in the virtual photoreactor operated under laminar flow (*Re*, 800) (A) or turbulent flow (*Re*, 4000) (B).

3.5.5 Optimization of operating conditions based on EEO analysis

The results of **Section 3.5.3** and **3.4.5** showed that the degradation ratio and the radiation efficiency showed opposite trends with the changes in operating conditions under the same flow regime in the virtual photoreactor: increasing the flow rate decreased the degradation ratio but increased the radiation efficiency, whereas increasing the radiant exitance increased the degradation ratio but decreased the radiation efficiency. As a consequence, degradation ratio and radiation efficiency could not be improved simultaneously (i.e. the highest removal ratio at the highest efficiency) by adjusting these operating conditions under the same flow regime. Therefore, optimization to find the most cost-effective operating condition is required.

For the EEO value that evaluating the cost-effectiveness in this research, the maximum pressure loss among all the simulations in the virtual photoreactor was 42 Pa at *Re* 4000, meaning that the maximum required pump input is

$$W_p = \frac{2.2 \times 10^{-4} \mathrm{m^3/s} \times 42\ \mathrm{Pa}}{50\%} \approx 0.02\ \mathrm{W} \tag{3-20}$$

Compared with the VUV lamp power (>30 W, **Table 3-2**), W_p in Eq. 3-15 is considered to be negligible. Based on Eqs. 3-12 and 3-13, a connection between radiation efficiency and EEO can be established through the actual log degradation ratio:

$$\mathrm{EEO} = A \cdot \frac{1}{\eta} \cdot \frac{\alpha}{k} \cdot \frac{P_l}{P_{VUV}} \tag{3-21}$$

where *A* is the conversion factor to convert watts to kilowatts, the natural logarithm to the common logarithm, and seconds to hours. Assuming the fourth term in Eq. 3-21 is a constant, EEO is a monotonic function of radiation efficiency. Thus, the results of radiation efficiency in 3.4.3 and 3.4.4 can be used to examine EEO with changes in operating conditions. In this research, the average power conversion efficiency of the VUV lamp with the transmittance sleeve (the reciprocal of the fourth term in Eq. 3-21) was assumed at 4.5% (**Section 3.3.2**). As a consequence, the EEO value will decrease as the flow rate increase (under the same flow regime) or the radiation exitance decrease.

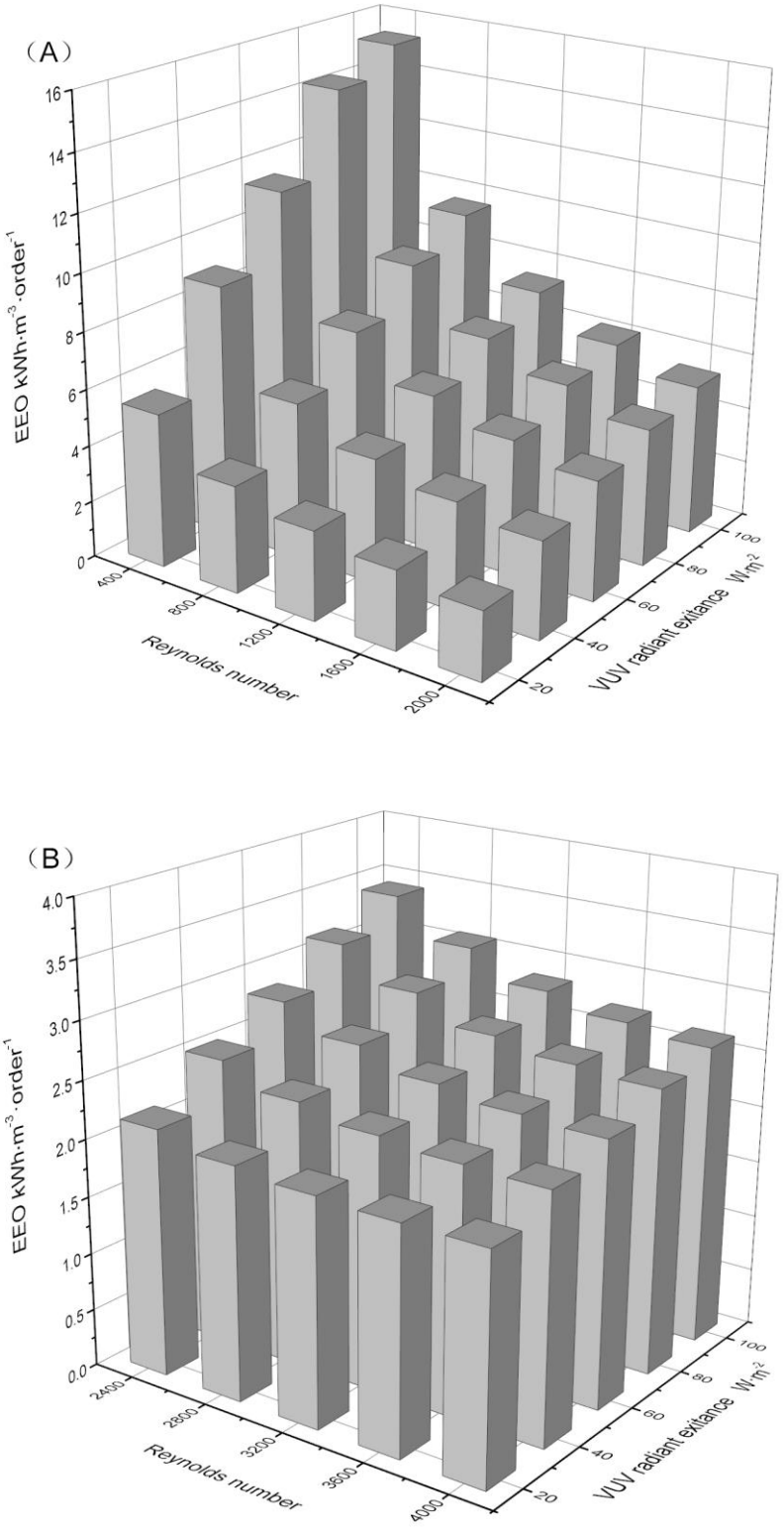

Fig. 3-11 Effects of flow rate (i.e., Reynolds number) and radiant exitance on electrical energy per order (EEO) in the virtual annular photoreactor operated under laminar flow (A) or turbulent flow (B).

Figure 3-11 shows EEO values calculated by using the radiation efficiencies obtained in the simulations under different flow rates (*Re* 400–4000) and radiant exitances (20–100 $W \cdot m^{-2}$) for GW3 in the virtual photoreactor. Under laminar flow (**Fig. 3-11** (A)), EEO was highly sensitive to both flow rate and radiant exitance. EEO decreased with both increasing flow rate, which is in agreement with previous research (Bagheri and Mohseni, 2015), and decreasing radiant exitance, suggesting that VUV treatment using low-power lamps and a high flow rate would be the most economical set-up under the laminar flow conditions.

Under turbulent flow (**Fig. 3-11** (B)), EEO was less sensitive to flow rate and radiant exitance compared with under laminar flow. Although the change was limited, EEO decreased with increasing flow rate, which is in agreement with previous research (Bagheri and Mohseni, 2017). Likewise, EEO slightly decreased with decreasing radiant exitance. This result suggested that VUV treatment using low-power lamps and a high flow rate would be the most economical set-up under the turbulent flow conditions

For the GW3 used in this research, EEO was insensitive to the changes in radiant exitance at the high flow rate. In contrast, the degradation ratio markedly increased with the increasing radiant exitance (**Fig. 3-12**). Therefore, some specific conclusions for GW3 can be obtained.

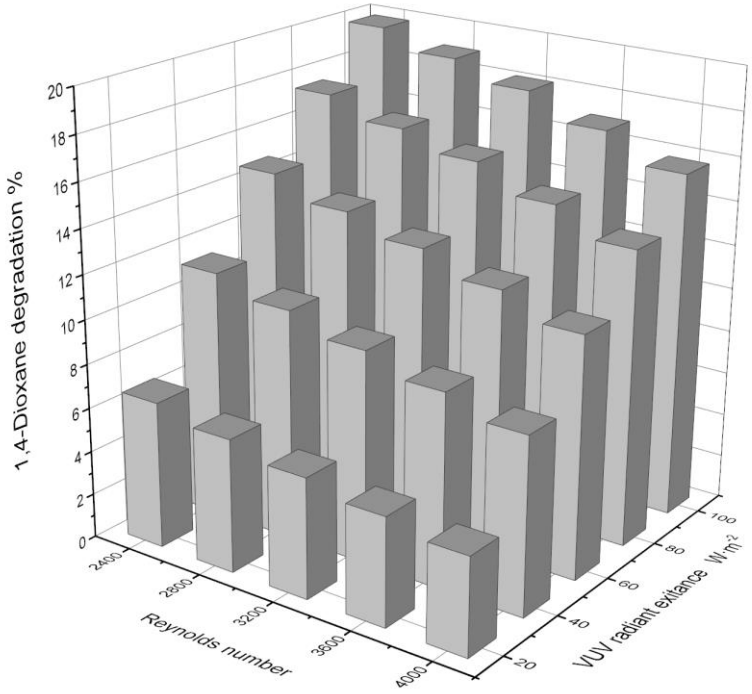

Fig. 3-12 Degradation of 1,4-dioxane under turbulent flow in the virtual photoreactor, as determined by computational fluid dynamics simulation.

At *Re* 4000 with the same desired degradation ratio of 50%, 17 virtual photoreactors with radiant exitance of 20 $W \cdot m^{-2}$ in series can achieve (0.96^{17}, **Fig. 3-13**), whereas 4 virtual photoreactors with radiant exitance of 100 $W \cdot m^{-2}$ in series can achieve (0.84^{4}, **Fig. 3-13**). Compare the two systems: the total electrical energy for lamps was 527 W (31×17, **Table 3-2**) versus 628 W (157×4, **Table 3-2**), and the number of the reactors was 17 versus 4. Although the former has low energy consumption in VUV lamps, the actual cost after including the costs of investment, operating, and maintenance will be higher than the latter. As a consequence, VUV treatment using high-power lamps and at a high flow rate is recommended for GW3 under turbulent flow, because the increase in acceptable energy cost will result in a significant reduction in the costs of investment, operating, and maintenance.

3.6 Conclusions

1. A CFD-based model that takes into account the effects of operating conditions on 1,4-dioxane was developed based on the kinetic model developed in Chapter 2. To reduce the cost of computational resources, the kinetic model was simplified as a pseudo-first-order degradation reaction, whose reaction constant is determined in advance for the CFD-based model simulation and can be easily obtained by the kinetic model (or a simple batch experiment conducted in the quasi-collimated beam photoreactor). The model successfully predicted 1,4-dioxane degradation in a pilot-scale flow-through annular photoreactor operated at different flow rates and radiant exitances, confirming the reliability of the model.

2. Model simulation in a virtual photoreactor revealed that both increasing flow rate and decreasing radiant exitance increased radiation efficiency (improved the radiant energy efficiency), which was findings that agreed with those from the experiments using the pilot-scale photoreactor.

3. EEO analysis suggested that VUV treatment using low-power lamps and a high flow rate was the most economical set-up. Specifically for the groundwater used in this research, treatment using high-power lamps at a high flow rate was suggested to be the most economical set-up under turbulent flow.

3.7 References:

Bagheri, M., Mohseni, M., 2017. Pilot-scale treatment of 1,4-dioxane contaminated waters using 185 nm radiation: Experimental and CFD modeling. Journal of Water Process Engineering 19, 185–192.

Bagheri, M., Mohseni, M., 2015. A study of enhanced performance of VUV/UV process for the degradation of micropollutants from contaminated water. Journal of Hazardous Materials 294, 1–8.

Bolton, J.R., Stefan, M.I., 2002. Fundamental photochemical approach to the concepts of fluence (UV dose) and electrical energy efficiency in photochemical degradation reactions. Research on Chemical Intermediates 28, 857–870.

Darbyshire, A.G., Mullin, T., 2005. Transition to turbulence in pipe flow. Fluid Mechanics and its Applications 77, 221–231.

De Laat, J., Gallard, H., Ancelin, S., Legube, B., 1999. Comparative study of the oxidation of atrazine and acetone by H2O2/UV, Fe(III)/UV, Fe(III)/H2O2/UV and Fe(II) or Fe(III)/H2O2. Chemosphere 39, 2693–2706.

Heit, G., Neuner, A., Saugy, P.Y., Braun, A.M., 1998. Vacuum-UV (172 nm) actinometry. The quantum yield of the photolysis of water. Journal of Physical Chemistry A 102, 5551–5561.

Imoberdorf, G., Mohseni, M., 2012. Kinetic study and modeling of the vacuum-UV photoinduced degradation of 2,4-D. Chemical Engineering Journal 187, 114–122.

Rahn, R.O., 1997. Potassium Iodide as a Chemical Actinometer for 254 nm Radiation: Use of Iodate as an Electron Scavenger. Photochemistry and Photobiology 66, 450–455.

Sharpless, C.M., Linden, K.G., 2003. Experimental and model comparisons of low- and medium-pressure Hg lamps for the direct and H2O2 assisted UV photodegradation of N-nitrosodimethylamine in simulated drinking water. Environmental Science and Technology 37, 1933–1940.

Siamak, E., Fariborz, T., 2010. Simulation of UV photoreactor for degradation of chemical contaminants: Model development and evaluation. Environmental Science and Technology 44, 2056–2063.

Versteeg, H.K., Malalasekera, W., 2007. An introduction to computational fluid dynamics: the finite volume method.

Wols, B.A., Harmsen, D.J.H., van Remmen, T., Beerendonk, E.F., Hofman-Caris, C.H.M., 2015. Design aspects of UV/H2O2 reactors. Chemical Engineering Science 137, 712–721.

Wols, B.A., Hofman-Caris, C.H.M., 2012. Modelling micropollutant degradation in UV/H 2O

2 systems: Lagrangian versus Eulerian method. Chemical Engineering Journal 210, 289–297.

Wols, B.A., Hofman, J.A.M.H., Beerendonk, E.F., Uijttewaal, W.S.J., van Dijk, J.C., 2011. A systematic approach for the design of UV reactors using computational fluid dynamics. AIChE Journal 57, 193–207.

Xie, P., Yue, S., Ding, J., Wan, Y., Li, X., Ma, J., Wang, Z., 2018. Degradation of organic pollutants by Vacuum-Ultraviolet (VUV): Kinetic model and efficiency. Water Research 133, 69–78.

Chapter 4. The effects of design parameter on the performance of VUV photoreactor - CFD model analysis

4.1 Chapter introduction

In **Chapter 3**, the general conclusions on the operating condition optimization of a given VUV photoreactor were obtained. Based on that, the present chapter further investigated the other aspect with significant effects on VUV process performance, the design parameter. Under continuous flow operation, the design parameter is of paramount importance since the high absorption coefficient of water at VUV limits the degradation in the VUV process to a thin penetration layer (Zoschke et al., 2014). However, experimental investigation of the VUV process was time- and resource-intensive since there were many design parameters associated with continuously operating flow-through VUV photoreactors (Bagheri and Mohseni, 2015).

CFD modeling was supposed to be an effective approach to overcoming pertinent design issues since CFD model simulations have been extensively applied for design exploration studies in the UV processes in the past (Duran et al., 2011; Santoro et al., 2010; Siamak and Fariborz, 2010; Sozzi and Taghipour, 2006; Wols et al., 2015). Among them, Wols' CFD modeling (Wols et al., 2015) has led to improvements in the UV/H_2O_2 system designs.

Bagheri and Mohseni (2015) introduced the CFD model to the VUV photoreactor design parameters analysis. However, their model has simply compared the performances of 8 different design sceneries with different design parameters (i.e. reactor hydraulic diameter, reactor illuminate area, and baffles) and did not systematically investigate them (for each parameter only 3 design sceneries with different operating conditions were discussed). Moreover, the model was developed for the synthetic water that only took into account carbonate/bicarbonate and NOM to assess the effects of water matrices, the other influential ions obsequiously present in natural water (i.e. chloride and nitrate/nitrite discussed in **Chapter 2**) had not been considered. Therefore, their CFD model for the VUV photoreactors implementation is limited.

Based on the above, the main objective of this chapter was to extant the CFD-based model developed in **Chapter 3** to systematically investigate the effect of the design parameters on the

VUV photoreactor performance, and work out the general solutions for design parameters optimization that contribute to the practical implementation of VUV process.

By adopting the CFD-based model simulations of the degradation of 1,4-dioxane in actual groundwater (GW3, Table 2-1, contains chloride and nitrate compared with the synthetic water in Bagheri's research (Bagheri and Mohseni, 2015)), the effects of design parameters (i.e. reactor gap (hydraulic diameter), reactor length, and baffles) on the VUV photoreactor performance were investigated. General conclusions about the effects of design parameters on VUV photoreactor performance were obtained by the simulation results. A model-aid methodology for the optimization and implementation of VUV photoreactor according to the actual requirement for drinking-water treatment was proposed by this research.

It should be mentioned that, for the actual photoreactor, the reactor length is highly limited by the length of the available lamps. The general conclusion on reactor length obtained by the model in this research is a reference for the actual design of the reactor when selecting the specifications of the light source.

4.2 Experimental set-up and procedures

All chemicals were purchased commercially and used without further purification. Reagent solutions for the experiments were prepared with guaranteed reagent grade chemicals and Milli-Q water (18.2 MΩ·cm, Milli-Q Advantage, Millipore Co., Bedford, MA, USA). Three types of water were used for the experiments: natural groundwater (GW3), dechlorinated tap water buffered with carbonate/bicarbonate (DTW_{buffer}), synthetic water (SW), which had already been described in **Chapter 2 Section 2.2.1** and **Chapter 3 Section 3.2.1**.

Experiments were conducted in three flow-through VUV photoreactors (**Table 4-1**). Reactor 1 and reactor 2 were described in **Chapter 2 Section 2.2.2** and **Chapter 3 Section 3.2.3**, respectively. Reactor 3 was made of stainless steel (**Fig. 4-1**) equipped with low-pressure mercury lamps (8W, Heraeus Noblelight GmbH, Hanau, Germany). The internal radius of the reactor and the external radius of the quartz sleeve were 26.8 and 11.5 mm, respectively, resulting in a radial gap of 15.3 mm, which corresponded to a hydraulic diameter of 30.6 mm for the water flowing through the reactor. The lamps provided a 32-cm-long cylindrical radiation zone within the 38-cm photoreactor. The stable VUV photon emissions on the surface

of the quartz sleeve were 16 $W \cdot m^{-2}$, measured by the same radiometer use in **Chapter 2**. Samples were withdrawn from the sampling points (**Fig. 4-1**), and the concentrations of 1,4-dioxane in the samples were measured as described in **Chapter 2.**

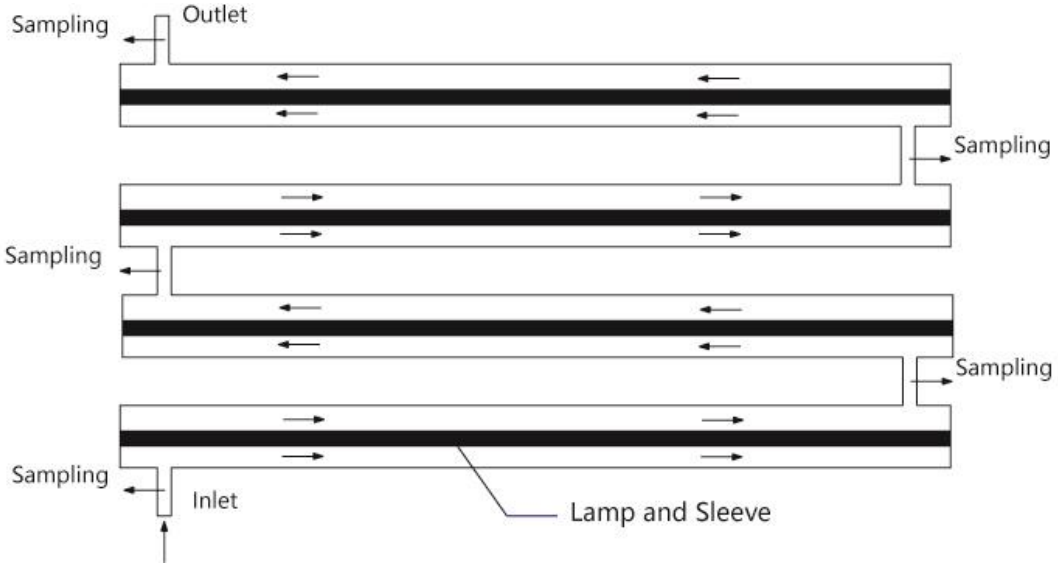

Fig. 4-1 Schematic of the VUV reactor 3.

Table 4-1 Overview of the 1,4-dioxane degradation experiments in VUV reactor with different design parameters.

Reactor	Flow	Radiation exitance on the surface of the sleeve	Water
1	T(5 $L \cdot min^{-1}$)	157 $W \cdot m^{-2}$	GW3
1	T(5 $L \cdot min^{-1}$)	157 $W \cdot m^{-2}$	DTW_{buffer}
2	L (1.5 and 4.5 $L \cdot min^{-1}$) &T(6.96 and 10.5 $L \cdot min^{-1}$)	105 $W \cdot m^{-2}$	GW3
2	T (6.96 $L \cdot min^{-1}$)	7.3, 13.9, 25.6, 40.3, 60.1 and 105 $W \cdot m^{-2}$	DTW_{buffer}
3	L(4.5 $L \cdot min^{-1}$) & T(10 $L \cdot min^{-1}$)	16 $W \cdot m^{-2}$	SW

4.3 CFD modeling

ANSYS® Workbench 2019R was used to build and discretize the three annular photoreactors with different design parameters. The settings in ANSYS® Fluent included viscosity models, radiation field, Lagrangian approach, UDF, and boundary layer were described in **Chapter 3**. VUV radiant exitance on the surface of the sleeve was summarized in **Table 4-1**. The computational domain of reactor 1 was divided into 0.8 million cells constituting an unstructured mesh, reactor 3 was divided into 1.7 million unstructured cells, while the mesh of reactor 2 was using the same mesh in **Chapter 3**.

To investigate the effect of reactor gap (thickness of the water layer, hydraulic radius), virtual annular photoreactors with the same inner radius (11.5 mm), and different outer radii (16.0, 19.0, 21.5, 23.4, 26.8 mm) were set for simulation. To investigate the effect of reactor length, virtual annular photoreactors with a variable length of 0.25 m to 1.5 m were set, the reactor gaps of them were set to two groups of 4.5 mm and 12.4 mm. To ensure accurate results of hydraulics and radiation, a radial division of 30 uniform elements in the water domain was applied. The axial direction was discretized into a uniform distribution of nodes with an interval of 1.0 mm. Mesh dependency studies indicated that the grid was fine enough to give grid-independent results. Radiant exitance was defined as the direct irradiation on the external surface of the quartz sleeve, two values of 20 $W \cdot m^{-2}$ and 100 $W \cdot m^{-2}$ were set, and the whole length of the photoreactor was assumed to be irradiated. Inlet velocity distributions at different flow rates with a given *Re* (fully developed laminar flow *Re* 1000 or turbulent flow *Re* 4000) were set by using the appropriate profile in ANSYS® Fluent.

4.4 Results and discussion

4.4.1 Model validation

To verify and validate the effects of different reactor gaps and lengths on the CFD-based model predictions, a series of experiments (**Table 4-1**) were conducted in the 3 different photoreactors under different operating conditions. The comparison result based on the 1,4-dioxane residual ratio predicted by the CFD-based model simulation against the experimental results obtained at each case was presented in **Fig. 4-2**. As is evident in this figure, the CFD-based model successfully predicted the residual ratio with the different design parameters and the different

operating conditions without further parameter fitting. The good agreement between the CFD-based model prediction and experimental data confirmed the reliability of the model on analyzing the annular photoreactor gap and length.

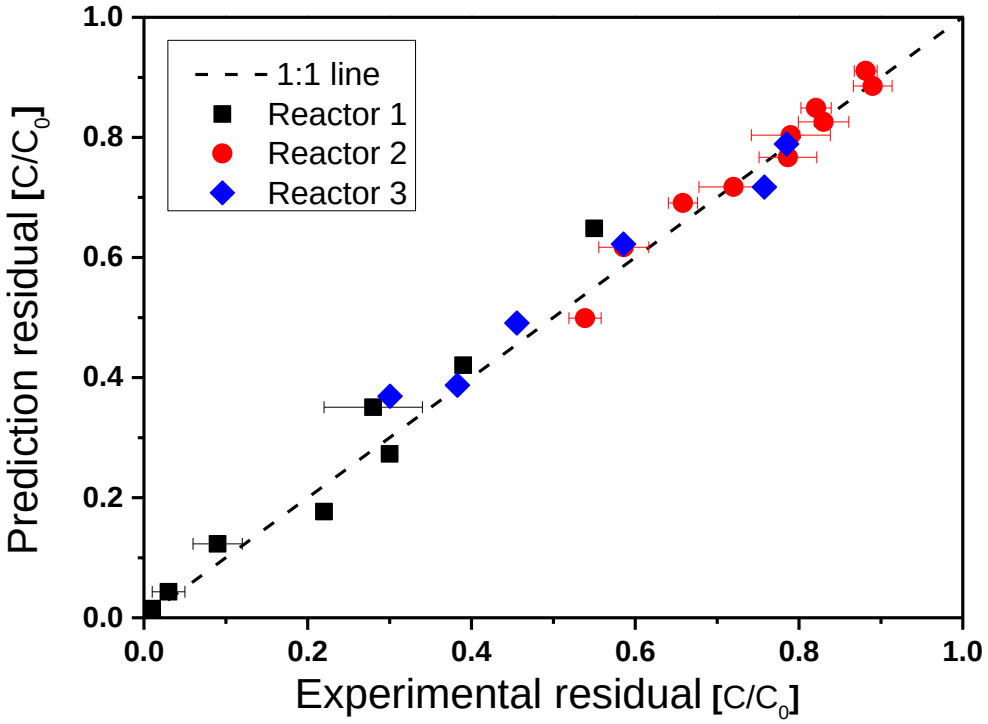

Fig. 4-2 Comparison of CFD model predicted and experimental 1,4-dioxane residual in different reactors. Error bars indicate standard deviations of at least two experiments.

4.4.2 Effects of reactor gap

To investigate the effect of reactor gap on 1,4-dioxane degradation, virtual photoreactors with different reactor gaps from 4.5 mm to 15.3mm and a fixed reactor length of 1 m were built. Simulations using GW3 under laminar flow (*Re* 1000) and turbulent flow (*Re* 4000) were set up in the virtual photoreactors. The radiant exitance was set to 20 $W \cdot m^{-2}$ and 100 $W \cdot m^{-2}$, respectively. The simulated results of 1,4-dioxane degradation in these virtual photoreactors followed the same trend that the degradation ratio of 1,4-dioxane decreased with the increasing reactor gap under both laminar (*Re* 1000) and turbulent flow (*Re* 4000) (**Fig. 4-3**). Increasing the reactor gap for the turbulent flow at the same *Re* increased the flow rate, resulting in the average VUV dose of the water passing through (Eq. 3-13). Therefore, the theoretical maximum

degradation ratio decrease (Eq. 3-7), and the simulation results of the degradation ratio also decrease accordingly.

The decrease was more obvious under laminar flow than turbulent flow due to the different VUV dose distribution of the particles. The VUV radiation field in the photoreactor was non-uniform: the fluence rate decreased exponentially with distance from the lamp increase, and the VUV dose of each particle varied according to its trajectory. Under laminar flow, particles were supposed to migrate in parallel layers, and the VUV fluence rate of the particle did not change along its trajectory. Particles that migrate near the sleeve received the most VUV radiation, while those migrating near the other reactor wall received the least. Therefore, when the reactor gap increased, the added water received less VUV radiation because the distance to the sleeve was greater, which resulted in the least degradation in this part and further the decreasing of the overall degradation. In contrast, under turbulent flow, chaotic changes in pressure and velocity occur while the particles pass through the photoreactor, which allows the particles that are initially far away from the sleeve to approach the sleeve to obtain more VUV irradiation. Increasing the reactor gap for the turbulent flow decreased the average VUV dose but not greatly affected the VUV dose distribution form, thus resulted in the degradation not decrease as significantly as the laminar flow.

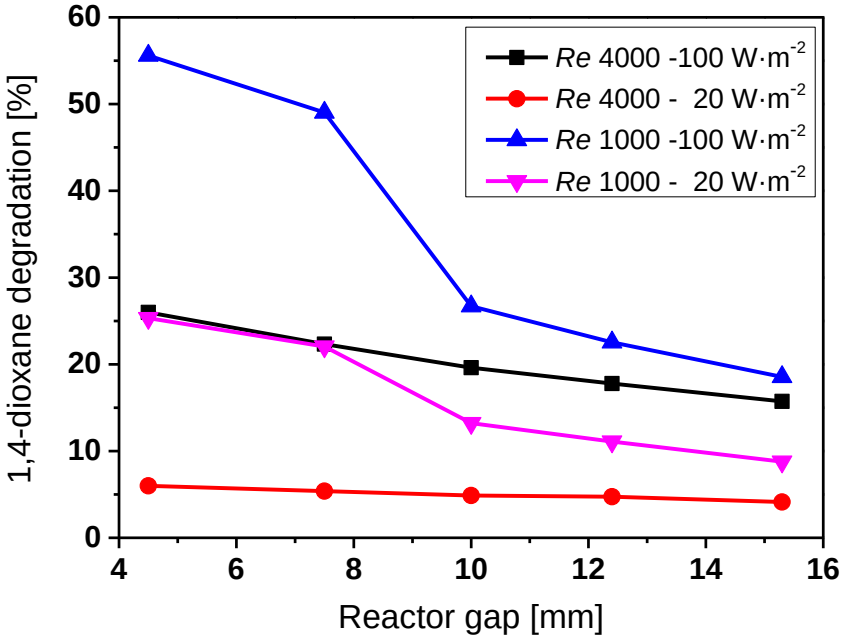

Fig. 4-3 Effect of reactor gap (i.e., water layer thickness) on 1,4-dioxane degradation in the virtual photoreactor.

An obvious decrease of degradation ratio between the reactor gap of 7.5 mm and 10 mm was observed under laminar flow. This is caused by the different ratio of the water flux in the penetration layer (99% of VUV photons were absorbed within the layer, whose thickness was calculated by optical depth) to the water flux in the reactor gap. Radial velocity distribution of a fully developed laminar flow in an annular photoreactor can be calculated by (Munson et al., 2002) :

$$u(r) = \frac{2Q}{\pi(R_{out}^2 - R_{in}^2)} \cdot \frac{1}{(R_{out}^2 + R_{in}^2) - \frac{(R_{out}^2 - R_{in}^2)}{ln\left({R_{out}}/{R_{in}}\right)}} \cdot \left[\frac{ln\left({r}/{R_{in}}\right)}{ln\left({R_{out}}/{R_{in}}\right)} \cdot \left(R_{out}^2 - R_{in}^2\right) - \left(r^2 - R_{in}^2\right)\right] \quad (4\text{-}1)$$

where Q represents the flow rate, R_{in} and R_{out} represent the inner and outer radial of the water layer, respectively. Then the ratio of the water flux in the penetration layer to the water flux in the reactor gap (i.e. flow rate) can be calculated by

$$\mathrm{M} = \frac{\int_{R_{in}}^{R_{in}+h} u(r) \cdot 2\pi r \mathrm{d}r}{Q} \quad (4\text{-}2)$$

where h represents the thickness of the penetration layer (4 mm for GW3). And the calculation results of each reactor gap were shown in **Fig.4-4**.

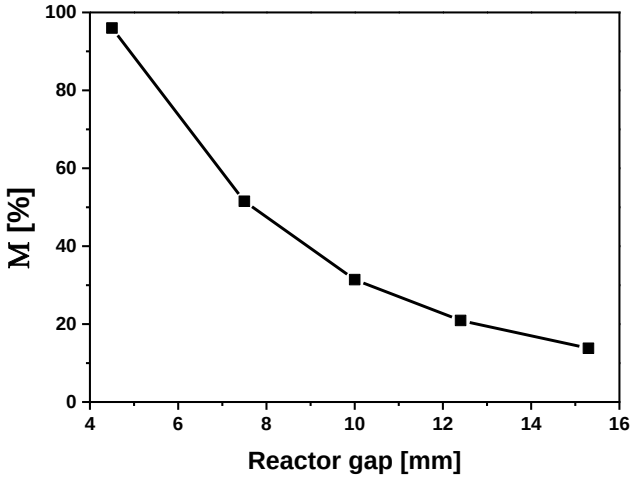

Fig. 4-4 The ratio of the water flux in the penetration layer to the flow rate at different reactor gaps

For the reactor with a 4.5 mm reactor gap, the penetration layer covers most of the entire volume of the reactor, and the water flux of the non-irradiated (VUV dose less than 1% of the total) layer was low, which made it have a comparable performance with the turbulent flow in the same reactor shape and under 100 $W \cdot m^{-2}$ radiant exitances. For the reactor with a 7.5 mm reactor gap, the penetration layer covers the most value of the reactor, the water flux in the penetration layer was predominant though the proportion had declined, which made the overall degradation slightly decreased compared with the 4.5 mm reactor gap. Further increasing the reactor gap, the water flux of the non-irradiated layer gradually dominated the water-through, the overall degradation significantly decreased. The significant decrease was between the reactor gap of 7.5 to 12.4 mm, which is the optical depth for GW3 from 3 to 5.

EEO was found to increase with the increase of the reactor gap (**Fig.4-5**) under both laminar flow and turbulent flow, which means a small reactor gap is more cost-effective. However, a small reactor gap leads to another problem that the flow rate is low, which increases the number of reactors required for the same amount of water within a certain time. At *R*e 4000 and radiant exitance of 100 $W \cdot m^{-2}$, with a similar degradation ratio and EEO, the virtual photoreactor with a reactor gap of 4.5 mm takes 11% more time to treat the same amount of water than the virtual photoreactor with a reactor gap of 7.5 mm.

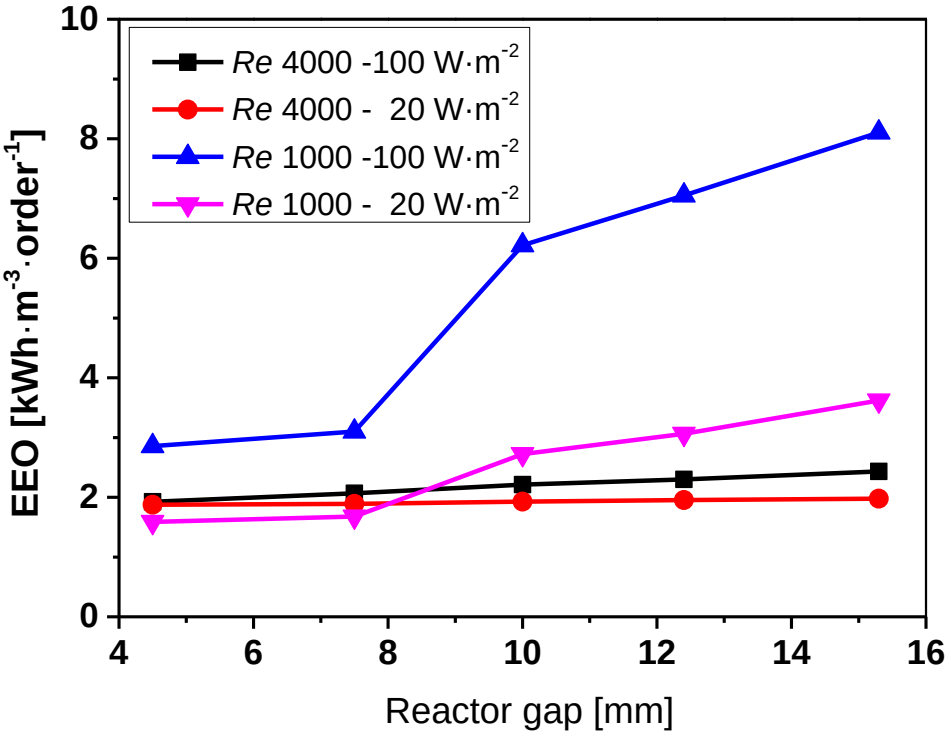

Fig. 4-5 Effect of reactor gap on EEO for 1,4-dioxane degradation in the virtual photoreactor.

Similar to the situation discussed in **Chapter 3 Section 3.5.5**, since the degradation ratio and EEO were not so sensitive to the change of the reactor gap, an acceptable solution for this problem may be solved by increasing the reactor gap within the tolerable range of degradation ratio decrease and EEO increase.

4.4.3 Effects of reactor length

To investigate the effect of reactor length on 1,4-dioxane degradation, virtual photoreactors with different reactor lengths from 0.25 m to 1.5 m with reactor gaps of 4.5 mm and 12.4 mm were built. Simulations using GW3 under laminar flow (*Re* 1000) and turbulent flow (*Re* 4000) were set up in these virtual photoreactors. The radiant exitance was set to 20 $W \cdot m^{-2}$ and 100 $W \cdot m^{-2}$, respectively. The simulated results of 1,4-dioxane degradation in these virtual photoreactors were shown in Fig.4-6. The degradation increased with increasing length under the same reactor gap, which was attributed to the increased total VUV dose due to the longer irradiation time. Under the laminar flow, the amount of the increase in the degradation ratio along with the reactor length increase was gradually smaller, and further increase the reactor length will not significantly increase the degradation. Because the water was supposed to be migrated in parallel layers that do not mix under laminar flow, the 1,4-dioxane in penetration layer received high enough VUV irradiation thus the concentration of 1,4-dioxane was close to zero; while the degradation limitedly occurred in the non-irradiated layer, therefore the overall degradation ratio (D) can be approximately calculated as:

$$D = 1 - \frac{Q_n C_0}{Q_n + Q_p} \tag{4-1}$$

where C_0 is the initial concentration, Q_p and Q_n represented the mass flow of the water in the penetration layer and non-irradiated layer, respectively. It should be mentioned that this calculation was under ideal conditions (i.e. the diffusion between layers in laminar flow was not considered). In practice, the degradation ratio will continue to increase with the increase in reactor length due to the diffusion, but the increase is extremely limited. In contrast, under turbulent flow, the degradation ratio kept increasing with the increase in the reactor length. Mass transfer under turbulent flow is achieved through chaotic changes in pressure and velocity, which attenuated the heterogeneity between the penetration layer and the non-irradiation layer.

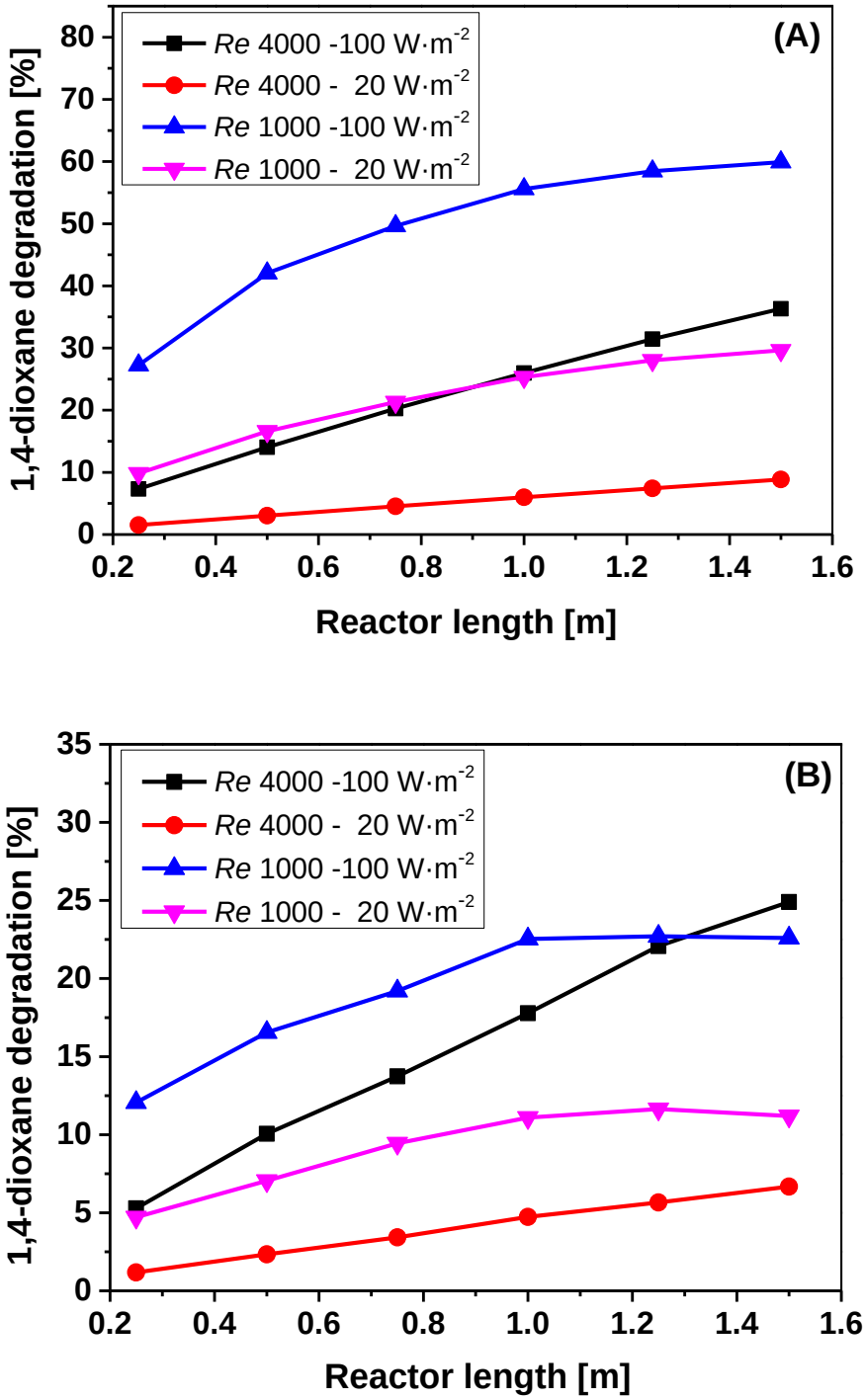

Fig. 4-6 Effect of reactor length on 1,4-dioxane degradation with the reactor gap of (A) 4.5 mm and (B) 12.4 mm

EEO was found to increase with the increase of the reactor gap (**Fig.4-5**) under laminar flow, while there were no significant changes in EEO under turbulent flow. Since increasing the reactor length proportionally increases the retention time of each particle, the VUV doses distribution of all the particles was increased by the same ratio along its trajectory, resulting in

a decrease in radiation efficiency according to Jensen's inequality (**Appendix 3**). Since the VUV dose distribution range of laminar flow is larger than that of turbulent flow (**Fig.3-9**), when the VUV dose of all the particles increases proportionally, the radiation efficiency of laminar flow decreases more significantly than that of turbulent flow. Based on Eq. 3-21, therefore, the EEO of laminar flow increases more obviously than turbulent flow.

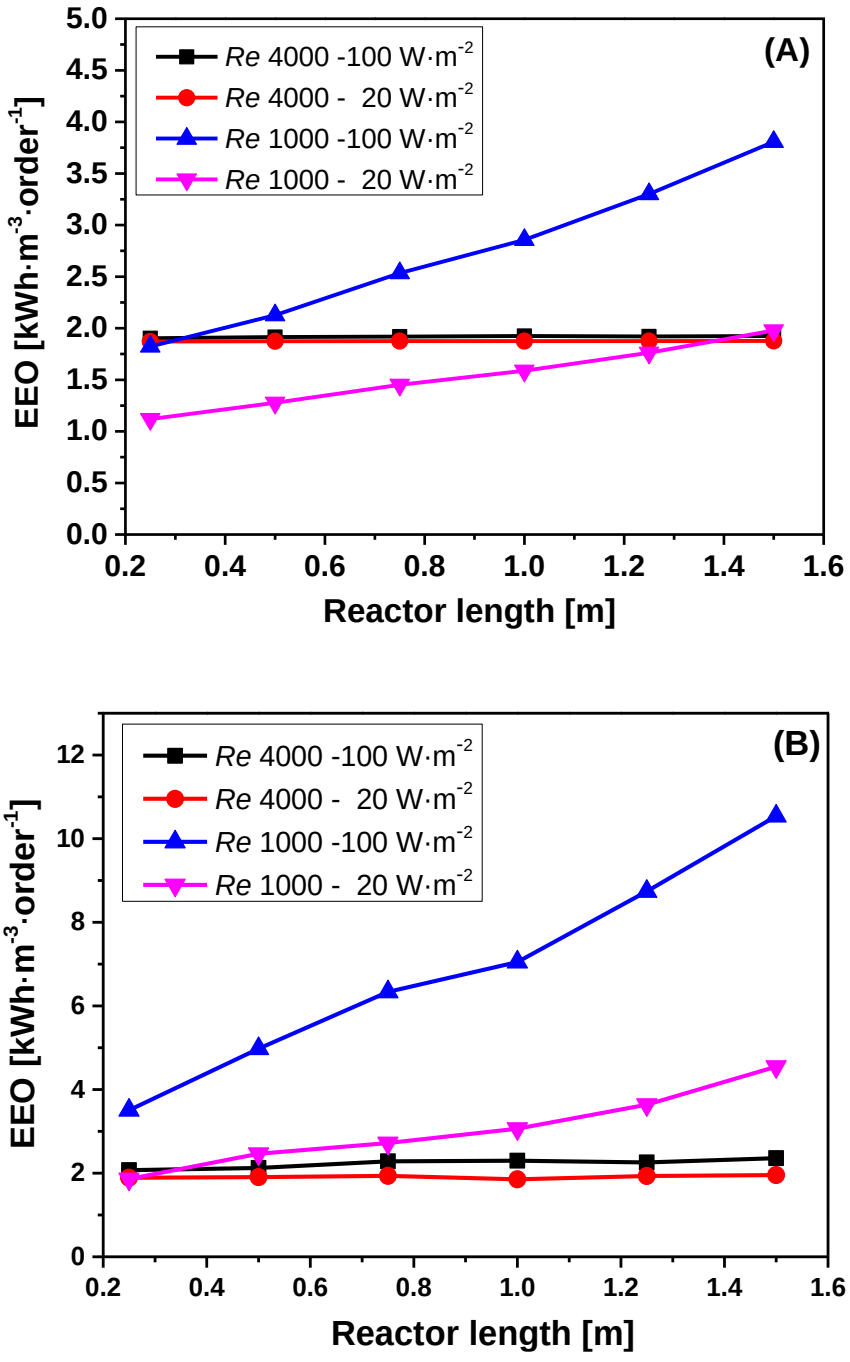

Fig. 4-7 Effect of reactor length on EEO of the 1,4-dioxane degradation with the reactor gap of (A) 4.5 mm and (B) 12.4 mm.

The simulation of the reactors with a thin reactor gap (4.5 mm) and short reactor length (less than 1.0 m) operated under laminar flow with a low VUV radiant exitance achieved the lowest EEO value (the most cost-effective) of all the simulations (**Fig. 4-7** (A) pink). However, compared with the other simulation result, the disadvantage of the low flow rate leads it only applicable to the treatment of the small amount of water (small treatment plant). The simulation of the reactor with a gap of 12.4 mm and 1.5 m in length, operated under turbulent flow and 100W·m^{-2} radiant exitance, achieved the most degradation among other simulations with the same reactor gap, even better than the laminar flow (with four times of the retention time) at the same radiation exitance. The EEO result also demonstrated that the larger-sized reactors operated under turbulent flow are more cost-effective for the treatment of a large amount of water (large treatment plants with centralized water-treatment processing).

4.4.4 Effect of retrofitting baffles

Retrofitting baffles can enhance mass transfer within the UV photoreactor and may thereby improve the performance of the processes (Li et al., 2020). This may be more significant for the VUV photoreactor than the UV photoreactor due to its thin penetration layer of VUV radiation. To evaluate the effect of baffles on the performance of the VUV photoreactors, 1.5-m virtual VUV photoreactors retrofitted with baffles arranged intervals 0.25, 0.50, and 0.75 m were set (**Fig. 4-8**), respectively. Considering the effect of the reactor gap discussed in 4.4.2, reactor gaps were set as 4.5 and 12.4 mm, respectively.

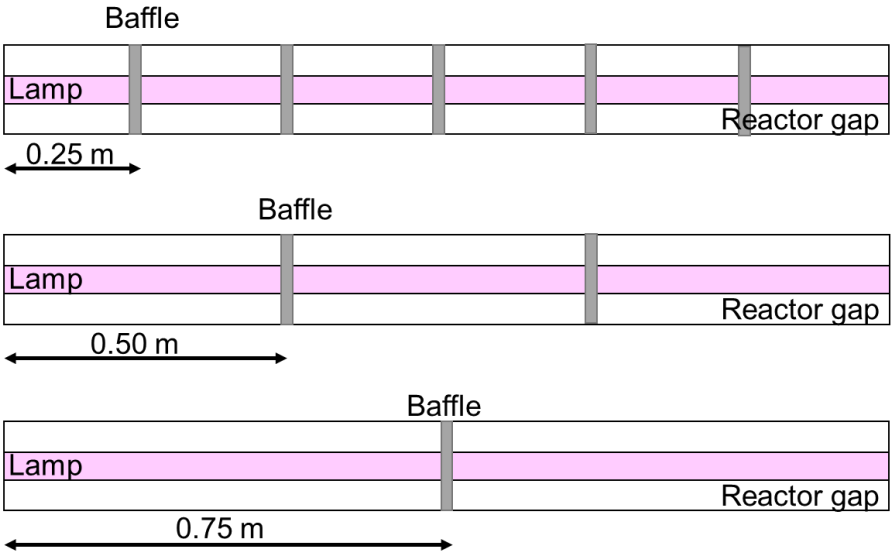

Fig. 4-8 Schematic of retrofitted baffles to the 1.5-m virtual photoreactor.

Due to the limitation of the experimental apparatus in this research that cannot retrofit the actual baffles, the CFD-based model cannot be validated for the effect of the baffle through experiments. Therefore, the discussions here were based on the theoretical max mix performance of the baffles, i.e. assuming the baffle could ideally completely mix the solution at where it was installed.

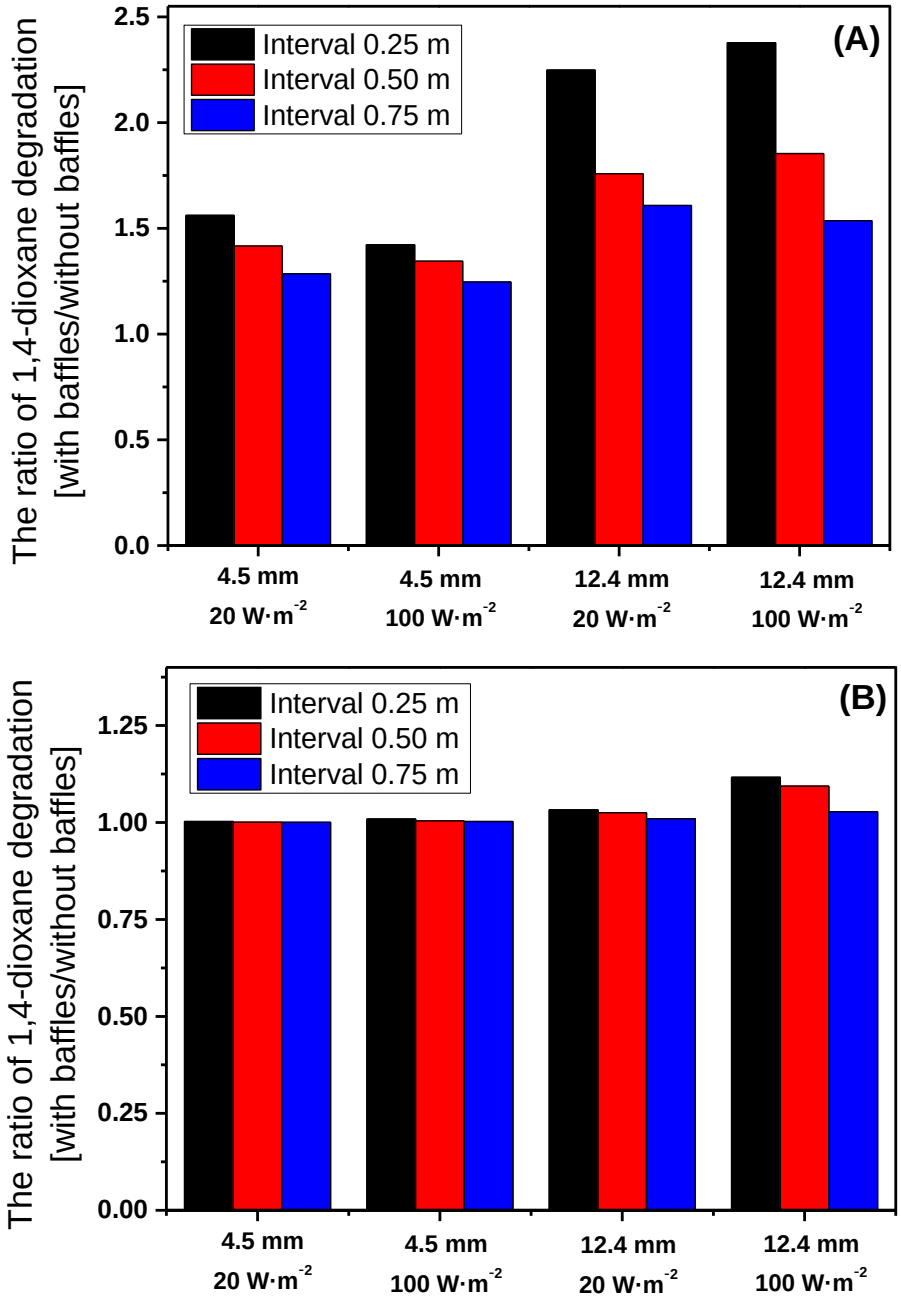

Fig. 4-9 Degradation enhanced by the baffles in the annular reactor under the most ideal conditions: (A) laminar flow and (B) turbulent flow.

The ideal baffles induced increases in 1,4-dioxane degradation under all of the simulations, especially for the long reactor gap (**Fig. 4-9**). Increasing the number of the baffles induced more improvement in degradation under both laminar flow and turbulent flow. The increment of degradation under laminar flow was much more obvious than turbulent flow with the same reactor gap and radiant exitance. Degradation under laminar flow increased around 24% at the minimum, while in contrast, the maximum increase under turbulent flow was around 12%.

Note that the actual degradation improvement would be at least less than the values illustrated in Fig. 4-9, considering that it is very difficult to achieve complete mixing even by incorporating the baffles into actual photoreactors. Therefore, the effect of baffles in the reactor with a short reactor gap under turbulent flow was limited, while for the reactor with a long reactor gap under turbulent flow it may slightly improve the performance. For laminar flow, incorporating baffles was necessary in case of using long reactors. Note that the actual degradation improvement would be at least less than the values illustrated in **Fig. 4-9**, considering that it is very difficult to achieve complete mixing even by incorporating the baffles to actual photoreactors.

4.4.5 Model-aided application scheme for the VUV process

Based on the above, a model-aided scheme of designing the VUV photoreactor according to the actual requirements could be proposed (**Fig. 4-10**). First, raw water was experimentally analyzed to obtain the absorption coefficient of UV and the concentrations of the influential ions (i.e. carbonate/bicarbonate, nitrite/nitrate, and chloride). And then calculate the approximate absorption coefficient of VUV according to Eq. 2-8. Run the kinetic model (or conducted the batch mode degradation experiments in the quasi-collimated apparatus) to get the pseudo-first-order degradation rate constant.

Second, based on the amount of water per day, determine the flow regime for the VUV photoreactor, laminar flow for the small amount of water, while turbulent flow for a large amount of water. Based on the other treatment requirements (e.g. desired removal, EEO, footprint, etc.) and the general conclusions in this chapter to determine the design parameters (or directly using the given photoreactor as the prototype design) and build the virtual photoreactor according to the design parameters. Based on the general conclusions of Chapter 3, determine the operating conditions in the virtual photoreactor.

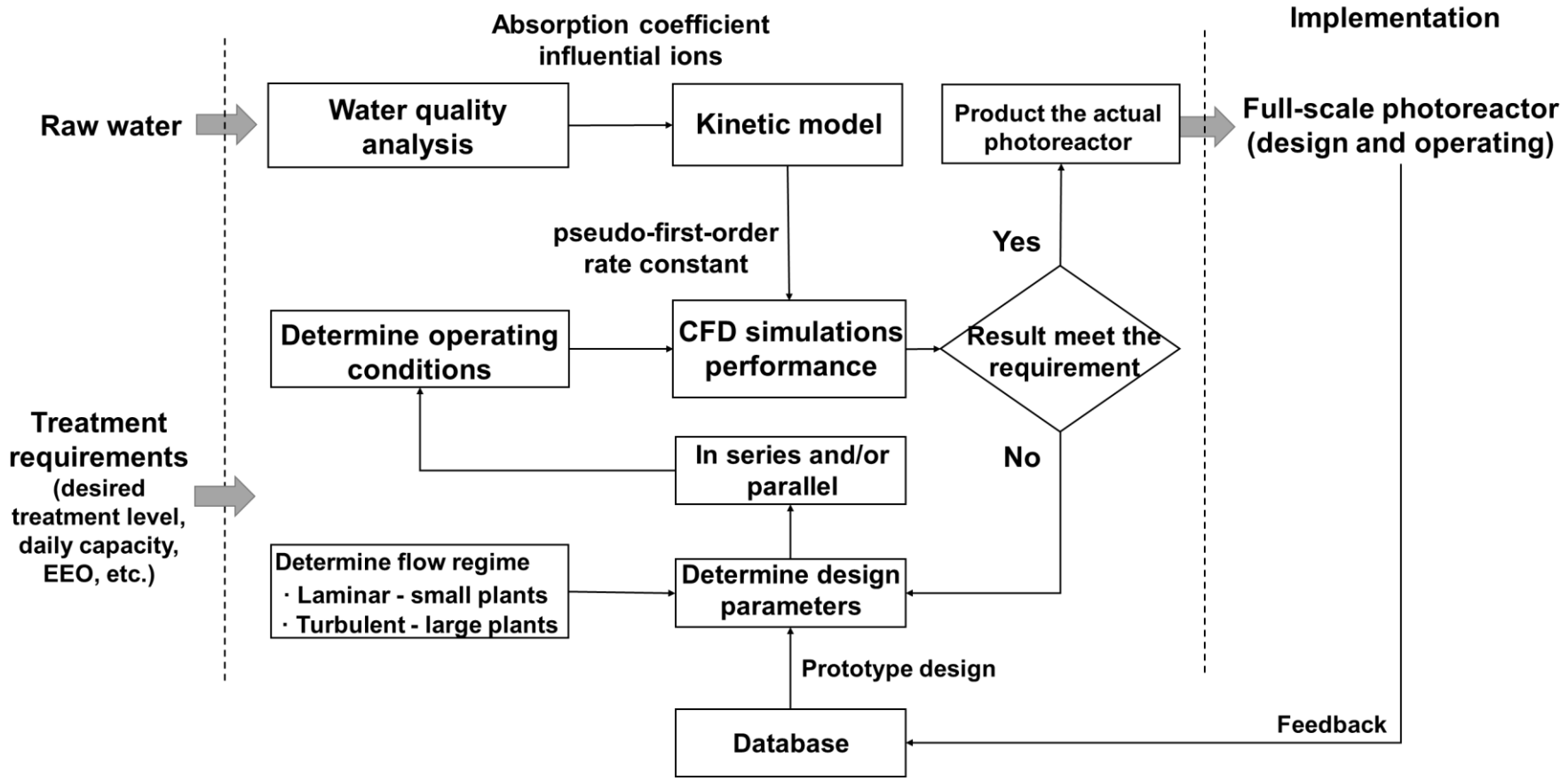

Fig. 4-10 Schematic of the model aided the VUV process implementation

Third, utilize the CFD-based model to simulate the degradation process in the virtual photoreactor and check whether it meets the requirement or not. If not, go back to the previous step, adjust the design parameter and operating conditions, run the simulation, and repeat these steps until the simulation result meets the treatment requirements. After the simulation result meets the treatment requirements, then produce the photoreactor and conduct experiments, then fine-tune the operating conditions to make the actual performance meet the requirements.

Compared with the traditional experimental method that performs the laboratory-scale experiments first and then gradually scale-up by a large number of experiments, the CFD-based model using the simulations replaces most of the experiments and could get an approximate solution, which results in saving time and manufacturing costs.

It should be mentioned that the performance of the produced photoreactor may probably not meet the treatment requirements, although the model had predicted that the produced photoreactor could treat the raw water to meet the requirements under the set operating conditions (i.e. model failure). The reason may be the inappropriate parameters in the model (e.g. the low reaction constant of NOM for RW discussed in **Chapter 2 Section 2.4.3**), defects of the CFD software provided module (e.g. using the *k*-ε model as the viscosity model to the simulation of large-eddy turbulent flow, Wols et al., 2010), etc. To solve the problem, a database that collects the application information is required regardless of the application's success or failure. As the database gradually expanded through the model application, the model would be optimized by data analysis, and then could be modified to make the prediction more accurate. In addition, the design parameters of the photoreactor obtained from a successful application of the model could be a prototype design for the next application, which will further save time in some cases.

4.5 Conclusions

1. The effects of the design parameters, i.e. reactor gap, reactor length, and baffle, on VUV photoreactor performance have been investigated systematically. Simulations with the virtual photoreactors showed that (1) increasing reactor gap and increasing reactor length increased EEO (i.e., decreased the efficiency), and (2) performance was improved by introducing some baffles into the reactor under laminar flows, but was not so obvious under turbulent flows especially for the reactor with a thin reactor gap.

2. For laminar flows, short VUV photoreactors with thin reactor gaps operated in series were recommended. Incorporating baffles was necessary in case of using long reactors. In contrast, for turbulent flows, a long VUV photoreactor with a relatively thin reactor gap was recommended, and the design parameters did not significantly affect the cost-effectiveness.

3. A CFD-based model for the optimization and implementation of VUV photoreactor for drinking-water treatment was developed, and a model-aid application scheme was proposed.

4.6 References:

Bagheri, M., Mohseni, M., 2015. A study of enhanced performance of VUV/UV process for the degradation of micropollutants from contaminated water. J. Hazard. Mater. 294, 1–8.

Duran, J.E., Mohseni, M., Taghipour, F., 2011. Design improvement of immobilized photocatalytic reactors using a CFD-Taguchi combined method. Ind. Eng. Chem. Res. 50, 824–831.

Li, W., Li, M., Qiang, Z., 2020. Improvement of UV disinfection reactor performance by ring baffles: The matching between the hydrodynamics and UV radiation. Chem. Eng. J. 379, 122381.

Munson, B.R., Young, D.F., Okiishi, T.H., 2002. Fundamentals of Fluid Mechanics. John Wiley & Sons, Inc., Hoboken, USA.

Santoro, D., Raisee, M., Moghaddami, M., Ducoste, J., Sasges, M., Liberti, L., Notarnicola, M., 2010. Modeling hydroxyl radical distribution and trialkyl phosphates oxidation in UV - H2O2 photoreactors using computational fluid dynamics. Environ. Sci. Technol. 44, 6233–6241.

Siamak, E., Fariborz, T., 2010. Simulation of UV photoreactor for degradation of chemical contaminants: Model development and evaluation. Environ. Sci. Technol. 44, 2056–2063.

Sozzi, D.A., Taghipour, F., 2006. UV reactor performance modeling by Eulerian and Lagrangian methods. Environ. Sci. Technol. 40, 1609–1615.

Wols, B.A., Harmsen, D.J.H., van Remmen, T., Beerendonk, E.F., Hofman-Caris, C.H.M., 2015. Design aspects of UV/H2O2 reactors. Chem. Eng. Sci. 137, 712–721.

Wols, B.A., Uijttewaal, W.S.J., Hofman, J.A.M.H., Rietveld, L.C., van Dijk, J.C., 2010. The weaknesses of a *k*-ε model compared to a large-eddy simulation for the prediction of UV dose distributions and disinfection. Chem. Eng. J. 162, 528–536.

4.6 References:

Zoschke, K., Börnick, H., Worch, E., 2014. Vacuum-UV radiation at 185nm in water treatment - A review. Water Res. 52, 131–145.

Chapter 5. Conclusions and recommendations

5.1 Conclusions

This dissertation focuses on developing a versatile CFD-based model for optimization and implementation of VUV photoreactor for drinking water treatment. The effects of the operating conditions (i.e. flow rate and radiation exitance) and design parameters (i.e. length, radius, and baffles) were analyzed by the CFD-based model, and the findings and conclusions were presented. 1,4-dioxane was selected as the target pollutant in the research although the methodology could be used for other OMPs.

In Chapter 2, influential ions and elementary reactions during the VUV process for 1,4-dioxane degradation were investigated. Since the performance of the VUV photoreactor is very sensitive to the water quality, it is the first yet important step to establish a comprehensive kinetic model for the CFD-based model aiming at the optimization and implementation of the VUV photoreactor for drinking-water treatment. The influential ions which are found ubiquitously in natural drinking-water sources were identified, namely carbonate/bicarbonate, chloride, and nitrate. Carbonate/bicarbonate and chloride directly suppress the degradation, whereas nitrate becomes influential after it is transformed into nitrite during the VUV process. The order of the extent of suppression per mole is nitrite >> bicarbonate > chloride. A kinetic model, which was set up by a series of ordinary differential equations about the rate of chemical and photochemical reactions in the VUV system, was developed to incorporate the influential ions and predict 1,4-dioxane degradation during the VUV process. The model was verified and validated by batch mode experiments conducted in a quasi-collimated beam photoreactor. By combining the chemical actinometry method, the model successfully predicted the 1,4-dioxane degradation in contaminated natural groundwater in a flow-through photoreactor. This result demonstrated that the model was accurate enough to predict the 1,4-dioxane degradation during VUV treatment of contaminated waters, and can be incorporated into the Lagrangian approach for the CFD-based model.

In Chapter 3, the effects of operating conditions (i.e. flow rate and radiation exitance) on the performance of the VUV photoreactor were investigated. a novel CFD-based model that takes into account the effects of operating conditions was developed based on the kinetic model developed in Chapter 2 to predict 1,4-dioxane degradation during the VUV process with the flow-through photoreactor. To reduce the cost of computational resources, the kinetic model

was simplified as a pseudo-first-order degradation reaction, whose reaction constant is determined in advance for the CFD-based model simulation and can be easily obtained by the kinetic model (or a simple batch experiment conducted in the quasi-collimated beam photoreactor). The CFD-based model was experimentally verified and validated under different operating conditions (i.e. flow rate and radiation exitance) in a flow-through pilot-scale VUV photoreactor, and the results confirmed the reliability of the model. A virtual photoreactor with the same inner and outer diameter as the pilot-scale reactor was set up and simulations with different operating conditions were made by the validated CFD-based model. Simulation results revealed that both increasing flow rate and decreasing radiant exitance increased the radiation efficiency (improved radiant energy efficiency), which agreed with the experimental results. Based on EEO analysis through these simulations, the following operations were finally recommended to be employed in actual drinking water treatment plants: VUV process using low-power lamps and a high flow rate was the most economical set-up. Specifically for the groundwater used in this research, treatment using high-power lamps at a high flow rate was suggested to be the most economical set-up under turbulent flow.

In Chapter 4, the effects of o design parameters (i.e. reactor length, reactor gap, and baffles) on the performance of the VUV photoreactor were investigated. More experiment data were collected from different flow-through VUV photoreactors with different design parameters, by which the CFD-based model developed in Chapter 3 was then validated and improved for analyzing the effects of design parameters. Virtual photoreactors with different design parameters were set up and simulations in these reactors were made by the validated CFD-based model. Simulation results with these virtual photoreactors showed that (1) both increasing reactor gap (the depth of the water path) and increasing radiant reactor length increased EEO (i.e., decreased the efficiency), and (2) performance was improved by introducing some baffles into the reactor under laminar flows, but was not so obvious under turbulent flows. Based on the simulation results, findings were concluded: 1) Operating under laminar flow is more economical for the small treatment plants. Short photoreactors with the thin reactor gap connected in series were recommended (lowest EEO). Incorporating baffles is necessary in the case of using a long photoreactor. 2) Operating under turbulent flow is more economical for large treatment plants. VUV photoreactor with a thin reactor gap is recommended, and other design parameters do not significantly affect the cost-effectiveness under turbulent flow.

Overall the research, a CFD-based model for the optimization and implementation of VUV photoreactor for drinking-water treatment was developed. The model will according to the raw water quality and the treatment requirements, through a few necessary experiments and model

simulations give the suitable design parameters and operating conditions for the full-scale VUV photoreactor. This model-aid methodology reduced the trial and error cost during the VUV photoreactor development from lab-scale to full-scale.

5.2 Recommendations for the future work of this research

From the experience acquired during the completion of this dissertation, the following recommendations can be made for future work:

- The kinetic model was developed based on elementary reactions constants at room temperature (25 ℃). To be closer to the actual processing in drinking-water treatment, extending the model to take into account the effect of temperature has to be considered.

- Compared with the kinetic model developed in Chapter 2, the simplified method of using the pseudo-first-order degradation rate constant for the Lagrangian particles in the CFD-based model may be relatively coarse. To improve the accuracy of the CFD-based model, optimize the algorithm to incorporate the whole kinetic model into the CFD-based model, or find a more accurate approximate method is required.

- In the present research, annular photoreactors with their lamps parallel to the main direction of the flow were investigated. Different geometrical configurations can be explored with the use of CFD (e.g. multi-lamps photoreactor, cross-flow lamps photoreactors). The methodology should be further adapted to search for the optimum (e.g. the best position of the lamps).

Appendix

1. MATLAB code of the kinetic model

```
function f=KM
% function of the kinetic model

T=[0,900];
% Total reaction time

A=xlsread (' E:/Model Input.xlsx ', 'Initial-ions', , 'B1:B36');
% Read initial concentration

options=odeset('AbsTol',1e-30,'RelTol',1e-10);
% Relative and absolute tolerance set to 1e-10 and 1e-30, respectively.

[ts,data] = ode15s(@kinetic,T,A,options);
plot(ts,data(:,36),'g')
legend('1,4-dioxane')
f=[ts,data];

function dmf=kinetic(t,X)
VUVt= xlsread (' E:/Model Input.xlsx ', 'Radiation', , 'B1');
UVt= xlsread (' E:/Model Input.xlsx ', 'Radiation', , 'B2');
% Read VUV and UV photon fluence

%-----------------------------------------------------------
% Species list (7+6+10+10+3, 36 in total)

% Radicals: R1 *OH, R2 *H, R3 *O2H, R4 *Cl, R5 *NO2 , R6 *NO R7 *ONOO

% Radical ions: Ri1 *O-, Ri2 *O-2, Ri3 *O-3, Ri4 *CO-3, Ri5 *OHCl-, Ri6 *Cl-2

% Ions: I1 H+, I2 OH-, I3 e, I4 HO-2, I5 HCO-3, I6 CO2-3, I7 Cl-, I8 NO-3
         I9 NO-2, I10 ONOO-

% Molecules: M1 H2O, M2 H2, M3 H2O2, M4 O2, M5 O3, M6 H2CO3
              M7 N2O4, M8 N2O3, M9 HOONO, M10 OP

% 1,4-dioxane, by-products, NOM
%-----------------------------------------------------------
```

```
R1=X(1);R2=X(2);R3=X(3); R4=X(4);R5=X(5);R6=X(6);R7=X(7)
% Radicals

Ri1=X(8);Ri2=X(9);Ri3=X(10);Ri4=X(11);Ri5=X(12);Ri6=X(13);
% Radical ions

I1=X(14);I2=X(15);I3=X(16);I4=X(17);I5=X(18);I6=X(19);I7=X(20);
I8=X(21);I9=X(22);I10=X(23);
% Ions

M1=X(24);M2=X(25);M3=X(26);M4=X(27);M5=X(28);M6=X(29);
M7=X(30);M8=X(31);M9=X(32);OP=X(33);
% Molecules

byp=X(34); dio=X(35); NOM=X(36);
% by-products, 1,4-dioxane, and NOM

% ----------------------------------------------------
% Radiation calculation

alpH2O=180;ALPh2o=0.1;
% Absorption cofficiect of pure water at 185 and 254 nm,

espHCO=1.1e2;espCO=1.75e2;
% Mole absorption coefficient of bicarbonat/carbonate at 185 nm

ESPo3=295.4;ESPh2o2=1.84;
% Mole absorption coefficient of O3 and H2O2 at 254 nm

espCl=360;espH2O2=28.9;espSO4=18.6;
% Mole absorption coefficient of Chloride, hydrogen peroxide and sulfate at 185 nm

ESPno3=0.398;ESPno2=1.28;
% Mole absorption coefficient of nitrate/nitrite at 254 nm


Abs185=alpH2O+espHCO*I5+espCO*I6+espH2O2*M3+espCl*I7+espSO4*cSO4
% Absorption cofficiect of the solution at 185 nm

Abs254=ALPh2o+ESPo3*M5+ESPh2o2*M3+ESPno3*I8+ESPno2*I9;
% Absorption cofficiect of the solution at 254 nm

VUVw=VUVt*alpH2O/Abs185;
VUVh=VUVt*espH2O2*M3/Abs185;
```

```
VUVcl=VUVt*espCl*I7/Abs185;

UVa=UVt*(1-10^(-Abs254*3.6));
UVo3=UVa*ESPo3*M5/Abs254;
UVh2o2=UVa*ESPh2o2*M3/Abs254;
UVno3=UVa*ESPno3*I8/Abs254;
UVno2=UVa*ESPno2*I9/Abs254;

% ------------------------------------------------
% Photon-induced reactions
K1=0.33;     % Eq. 1          H2O = *H + *OH                hv185
K2=0.045;    % Eq. 2          H2O = H+ + *OH + e            hv185
K3=0.5;      % Eq. 3          H2O2 = 2*OH                   hv185
K4=0.50;     % Eq. 4          H2O2 = 2*OH                   hv254
K5=0.4;      % Eq. 5          Cl- = *Cl + e                 hv185
K6=0.48;     % Eq. 6          O3 + H2O = H2O2 + O2          hv254
K7=0.09;     % Eq. 7          NO-3 = *NO2 + *O-             hv254
K8=0.046;    % Eq. 8          NO-2 = *NO + *O-              hv254
K9=0.001;    % Eq. 9          NO-3 = NO-2 +OP               hv254
% Equilibrium reactions
K10=1.4e8;   % Eq. 10         H+ + OH- = H2O
K10r=1.4;    % Eq. -10        H2O = H+ + OH-
K11=1.0e6;   % Eq. 11         *O2H = H+ + *O-2
K11r=5.7e7;  % Eq. -11        H+ +*O-2 = *O2H
K12=30;      % Eq. 12         H2O2 = H+ + HO-2
K12r=2e7;    % Eq. -12        H+ + HO-2 = H2O2
K13=3.5e6;   % Eq. 13         O2 + *O- = *O-3
K13r=4.3e3;  % Eq. -13        *O-3 = O2 + *O-
K14=5e3;     % Eq. 14         H2CO3 = H+ + HCO-3
K14r=1e7;    % Eq. -14        H+ + HCO-3 = H2CO3
K15=2.5;     % Eq. 15         HCO-3 = H+ + CO2-3
K15r=5e7;    % Eq. -15        H+ + CO2-3 = HCO-3
K16=4.3e6;   % Eq.16          Cl- + *OH = *OHCl-
K16r=6.1e9;  % Eq. -16        *OHCl- = Cl- + *OH
K17=6.5e6;   % Eq. 17         Cl- + *Cl = *Cl-2
K17r=1.1e5;  % Eq. -17        *Cl-2 = Cl- + *Cl
K18=2.1e7;   % Eq. 18         *OHCl- + H+ = *Cl+ H2O
K18r=2.5e8;  % Eq. -18        *Cl + H2O = H+ +*OHCl-
K19=6.9e3;   % Eq. 19         N2O4 = 2*NO2
K19r=4.5e5;  % Eq. -19        2*NO2 = N2O4
K20=3.2e16;  % Eq. 20         HOONO = H+ +ONOO-
K20r=1e7;    % Eq. -20        H+ +ONOO- = HOONO
% Degradation reactions
K21=3.1e6;   % Eq. 21         1,4-dioxane + *OH
```

```
K22=1e6;       % Eq. 22          by-products + *OH
K23=2.0e5;     % Eq. 23          NOM + *OH
% Other involving reactions
K24=3.6e5;     % Eq. 24          *H + OH- = H2O + e
K25=2.1e7;     % Eq. 25          *H + O2 = *O2H
K26=2.0e7;     % Eq. 26          e + O2 = *O-2
K27=6.6e6;     % Eq. 27          *OH + *O2H = H2O + O2
K28=7.0e6;     % Eq. 28          *OH + *O-2 = OH- + O2
K29=4.0e6;     % Eq. 29          2*OH = H2O2
K30=2.6e3;     % Eq. 30          2*O2H = H2O2 + O2
K31=9.7e4;     % Eq. 31          *O-2 + *O2H = O2 + HO-2
K32=6.0e4;     % Eq. 32          H2 + *OH = *H + H2O
K33=7.0e6;     % Eq. 33          *H + *OH = H2O
K34=3.9e5;     % Eq. 34          *OH + OH- = *O- + H2O
K35=2.7e4;     % Eq. 35          *OH + H2O2 = H2O + *O2H
K36=3.0e7;     % Eq.36           e + *OH = OH-
K37=7.5e6;     % Eq. 37          *OH + HO-2 = OH-+ *O2H
K38=2.0e6;     % Eq. 38          *OH + *O- = HO-2
K39=0.55;      % Eq. 39          *H + H2O = *OH + H2
K40=1.0e7;     % Eq. 40          2*H = H2
K41=1.0e7;     % Eq. 41          *H + *O2H = H2O2
K42=2.0e7;     % Eq. 42          *H + *O-2 =HO-2
K43=9.0e4;     % Eq. 43          *H + H2O2 = *OH + H2O
K44=2.3e7;     % Eq. 44           e + H+ = *H
K45=1.1e7;     % Eq. 45           e + H2O2 = *OH + OH-
K46=1.6e-2;    % Eq. 46          *O-2 + H2O2 = *OH + O2 + OH-
K47=7e5;       % Eq. 47          *O- + *O-3 = 2*O-2
K48=3.9e5;     % Eq. 48           CO2-3 + *OH = OH- + *CO2-3
K49=8.5e3;     % Eq. 49           HCO-3 + *OH = H2O + *CO2-3
K50=4.3e2;     % Eq. 50           H2O2 + *CO2-3 = HCO-3 + *O2H
K51=3.0e4;     % Eq. 51           HO-2 + *CO2-3 = CO2-3 + *O2H
K52=7e5;       % Eq. 52          *O-2 + *CO2-3 = CO2-3 + O2
K53=1e7;       % Eq. 53          H+ + *O- =    *OH
K54=6e4;       % Eq. 54          *O-3 + *CO2-3 = O3 + CO2-3
K55=3.6e7;     % Eq. 55          O3 + e = *O-3
K56=3.65e7;    % Eq. 56           O3 + *H = *OH + O2
K57=3e6;       % Eq. 57           *Cl-2 + *O2H = 2Cl- + H+ + O2
K58=1e6;       % Eq. 58           *Cl-2 + *O-2 = 2Cl- + O2
K59=140;       % Eq. 59           *Cl-2 + H2O2 = 2Cl- + *O2H + H+
K60=5e5;       % Eq. 60           *Cl + CO2-3 = Cl- + *CO-3
K61=2.2e5;     % Eq. 61           *Cl + HCO-3 = Cl- + *CO-3 + H+
K62=8e4;       % Eq. 62           *Cl-2 + CO2-3 = 2Cl- + *CO-3
K63=1.6e5;     % Eq. 63           *Cl-2 + HCO-3 = 2Cl- + *CO-3 + H+
K64=1.3e6;     % Eq. 64          *NO2 + *OH = HOONO
```

```
K65=5e6;        % Eq. 65          ONOO- + *OH = *ONOO + OH-
K66=1e10;       % Eq. 66          *ONOO = *NO + O2
K67=1e7;        % Eq. 67          *NO2 + *ONOO + H2O = 2NO-3 + 2H+
K68=6e5;        % Eq. 68          *NO2 + *H = H+ + NO-2
K69=1e7;        % Eq. 69          NO-2 + *OH = *NO2 + OH-
K70=1e3;        % Eq. 70          N2O4 + H2O = NO-3 + NO-2 +2 H+
K71=1e5;        % Eq. 71          *NO2 + *O-2 = O2 + NO-2
K72=1e7;        % Eq. 72          *NO + *OH = NO-2 + H+
K73=4.6e5;      % Eq. 73          *NO2 + e = NO-2
K74=1.1e6;      % Eq. 74          *NO + *NO2 = N2O3
K75=530;        % Eq. 75          N2O3 + H2O = 2NO-2 + 2H+
K76=1e2;        % Eq. 76          NO-3 + *OH = *ONOO +OH-
K77=3e5;        % Eq. 77          NO-3 + OP = NO-2 + O2
K78=3e6;        % Eq. 78          NO-2 + OP = NO-3
%-------------------------------------------------------

%-------------------------------------------------------
% ODEs
dR1=K1*VUVw+K2*VUVw-K27*R1*R3-K28*R1*Ri2-2*K29*R1*R1+...
    2*K3*VUVh+2*K4*UVh2o2...
    -K32*M2*R1-K33*R1*R2-K34*R1*I2-K35*R1*M3-K36*R1*I3...
    -K37*R1*I4-K38*R1*Ri1+K39*R2+K43*R2*M3+K45*I3*M3...
    -K48*I6*R1-K49*R1*I5+AK22*R2*I4+K53*I1*Ri1+K56*M5*R2...
    -K21*dio*R1-K22*byp*R1-K16*R1*I7+K16r*Ri5...
    -K64*R5*R1-K69*I9*R1-K72*R6*R1...
    -K65*R1*I10-K76*I8*R1-K23*R1*NOM;

dR2=K1*VUVw-K25*R2*M4+K32*M2*R1-K33*R1*R2-K39*R2...
    -2*K40*R2*R2-K41*R2*R3...
    -K42*R2*Ri2-K24*R2*I2-K43*R2*M3+K44*I1*I3-AK22*R2*I4-K56*M5*R2...
    -K68*R5*R2;

dR3=K25*R2*M4-K27*R1*R3-2*K30*R3*R3-K31*Ri2*R3+K35*R1*M3+K37*R1*I4...
    -K41*R2*R3+K11r*I1*Ri2-K11*R3+K50*M3*Ri4+K51*Ri4*I4-K57*Ri6*R3...
    +K59*Ri6*M3;

dR4=K5*VUVcl-K17*R4*I7+K17r*Ri6+K18*I1*Ri5-K18r*R4-K60*R4*I6...
    -K61*R4*I5;

dR5=K7*UVno3-K64*R5*R1-K67*R5*R7-K68*R5*R2+K69*I9*R1...
    -2*K19r*R5*R5+2*K19*M7-K71*R5*Ri2-K73*R5*I3-K74*R6*R5;

dR6=K8*UVno2+K66*R7-K72*R6*R1-K74*R6*R5;
```

```
dR7=K65*R1*I10-K66*R7-K67*R5*R7+K76*I8*R1;

dRi1=K34*R1*I2-K38*R1*Ri1-AK16*Ri1*M2-K13*M4*Ri1-K47*Ri1*Ri3+K13r*Ri3...
      -K53*I1*Ri1+ K7*UVno3+K8*UVno2;

dRi2=K26*I3*M4-K2*R1*Ri2-K31*Ri2*R3-K42*R2*Ri2-K11r*I1*Ri2+K11*R3...
      -K46*M3*Ri2+2*K47*Ri1*Ri3-K52*Ri4*Ri2-K58*Ri6*Ri2-K71*R5*Ri2;

dRi3=K13*M4*Ri1-K47*Ri1*Ri3-K13r*Ri3-K54*Ri3*Ri4+K55*I3*M5;

dRi4=K48*I6*R1+K49*R1*I5-K50*M3*Ri4-K51*Ri4*I4-K52*Ri4*Ri2...
      -K54*Ri3*Ri4+K60*R4*I6+K61*R4*I5+K62*Ri6*I6+K63*Ri6*I5;
dRi5=K16*R1*I7-K16r*Ri5-K18*I1*Ri5+K18r*R4;

dRi6=K17*R4*I7-K17r*Ri6-K57*Ri6*R3-K58*Ri6*Ri2-K59*Ri6*M3...
      -K62*Ri6*I6-K63*Ri6*I5;

dI1=K2*VUVw-K44*I1*I3-K10*I1*I2+K10r-K11r*I1*Ri2+K11*R3-K12r*I1*I4...
      +K12*M3+K46*M3*Ri2+K14*M6-K14r*I5*I1+K15*I5-K15r*I1*I6...
      -K53*I1*Ri1-K18*I1*Ri5+K18r*R4+K57*Ri6*R3+K59*Ri6*M3...
      +K61*R4*I5+K63*Ri6*I5+2*K67*R5*R7+K68*R5*R2+2*K70*M7...
      +K72*R6*R1+2*K75*M8+K20*M9-K20r*I1*I10;
dI2=K28*R1*Ri2-K34*R1*I2+K36*R1*I3+K37*R1*I4-K24*R2*I2-K45*I3*M3...
      -K10*I1*I2+K10r+K46*M3*Ri2+K48*I6*R1+AK22*R2*I4...
      +K69*I9*R1+K65*R1*I10+K76*I8*R1;

dI3=K2*VUVw-K26*I3*M4-K36*R1*I3+K24*R2*I2-K44*I1*I3-K45*I3*M3...
      +AK16*Ri1*M2-K55*I3*M5+K5*VUVcl-K73*R5*I3;
dI4=K31*Ri2*R3-K37*R1*I4+K38*R1*Ri1-K12r*I1*I4+K12*M3-K51*Ri4*I4...
      -AK22*R2*I4;

dI5=-K49*R1*I5+K50*M3*Ri4+K14*M6-K14r*I5*I1-K15*I5+K15r*I1*I6...
      -K61*R4*I5-K63*Ri6*I5;

dI6=-K48*I6*R1+K51*Ri4*I4+K15*I5-K15r*I1*I6+K52*Ri4*Ri2+K54*Ri3*Ri4...
      -K60*R4*I6-K62*Ri6*I6;

dI7=-K5*VUVcl-K16*R1*I7+K16r*Ri5-K17*R4*I7+K17r*Ri6+2*K57*Ri6*R3...
      +2*K58*Ri6*Ri2+2*K59*Ri6*M3+K60*R4*I6+K61*R4*I5...
      +2*K62*Ri6*I6+2*K63*Ri6*I5;

dI8= -K7*UVno3+2*K67*R5*R7...
      +K70*M7-K76*I8*R1-KN19*VUVno3-K9*UVno3...
      -K77*I8*OP+K78*I9*OP;
```

```
dI9= -K8*UVno2+K68*R5*R2-K69*I9*R1+K70*M7+K71*R5*Ri2...
     +K72*R6*R1+K73*R5*I3+2*K75*M8+KN19*VUVno3+K9*UVno3...
     +K77*I8*OP-K78*I9*OP;

dI10=K20*M9-K20r*I1*I10-K65*R1*I10;

dM1=0;

dM2=-K32*M2*R1+K39*R2+K40*R2*R2-AK16*Ri1*M2;

dM3=K29*R1*R1+K30*R3*R3-K3*VUVh-K4*UVh2o2...
     -K35*R1*M3+K41*R2*R3-K43*R2*M3-K45*I3*M3+K12r*I1*I4-K12*M3...
     -K46*M3*Ri2-K50*M3*Ri4+K6*UVo3-K59*Ri6*M3;

dM4=-K25*R2*M4-K26*I3*M4+K27*R1*R3+K28*R1*Ri2+K30*R3*R3+K31*Ri2*R3...
     -K13*M4*Ri1+K46*M3*Ri2+K13r*Ri3+K52*Ri4*Ri2+K6*UVo3+K56*M5*R2...
     +K57*Ri6*R3+K58*Ri6*Ri2...
     +K66*R7+K71*R5*Ri2+K77*I8*OP;

dM5=K54*Ri3*Ri4-K55*I3*M5-K6*UVo3-K56*M5*R2;

dM6=-K14*M6+K14r*I5*I1;

dM7=K19r*R5*R5-K19*M7-K70*M7;

dM8=K74*R6*R5-K75*M8;

dM9=K64*R5*R1-K20*M9+K20r*I1*I10;

dOP=KN19*VUVno3+K9*UVno3-K77*I8*OP-K78*I9*OP;

dbyp=K21*dio*R1-K22*byp*R1;

ddio=-K21*dio*R1;

dNOM=-K23*R1*NOM;

dmf=[dR1;dR2;dR3;dR4;dR5;dR6;dR7;...
     dRi1;dRi2;dRi3;dRi4;dRi5;dRi6;...
     dI1;dI2;dI3;dI4;dI5;dI6;dI7;dI8;dI9;dI10;...
     dM1;dM2;dM3;dM4;dM5;dM6;dM7;dM8;dM9;dOP;...
     dbyp;ddio;dNOM];
```

2. C code implemented in ANSYS Fluent to calculate the VUV dose

```
/*UDF for computing the VUV dose along a particle trajectory */
#include "udf.h"
#include "dpm.h"
#include "sg_disco.h"

#define C_dose(c,t)C_STORAGE_R_XV(c,t,SV_DO_IRRAD,0)

static real vuv_intensity_0;
static real x0, y00, z0;

DEFINE_DPM_SCALAR_UPDATE(vuv_dosage, cell, thread, initialize, p)
{
   cphase_state_t *c = &(p->cphase);
   if (initialize)
      {
         p->user[0] = 0.;
         vuv_intensity_0 = C_dose(cell,thread);
         x0=p->state.pos[0];
         y00=p->state.pos[1];
         z0=p->state.pos[2];
      }
   else
      {
         p->user[0] += P_DT(p) * .5 * (vuv_intensity_0 + C_dose(cell,thread));
         vuv_intensity_0 = C_dose(cell,thread);
      }
}

DEFINE_DPM_OUTPUT(vuv_output, header, fp, p, thread, plane)
{

char name[100];

if (header)
   {
      if (NNULLP(thread))

par_fprintf_head(fp,"(%s %d)\n",THREAD_HEAD(thread)->dpm_summary.sort_file_name,14);
      else
        par_fprintf_head(fp,"(%s %d)\n",plane->sort_file_name,14);

                par_fprintf_head(fp,"(%10s %10s    %10s    %10s    %10s    %10s    %10s"
```

```
                        " %10s    %10s    %10s    %10s %10s    %10s    %10s %s)\n",
                          "X0","Y0","Z0",
                          "X","Y","Z","U","V","W","diameter","T","mass-flow",
                          "time","VUV-Dosage","name");
            }
else
{
  sprintf(name,"%s:%lld",p->injection->name,p->part_id);
#if PARALLEL
        par_fprintf(fp,"%d %d ((%10.6g    %10.6g    %10.6g    %10.6g    %10.6g    %10.6g    "
            "%10.6g    %10.6g    %10.6g    %10.6g %10.6g %10.6g    %10.6g %10.6g) %s)\n",
                p->injection->try_id,p->part_id,
                x0,y00,z0,
                p->state.pos[0], p->state.pos[1], p->state.pos[2],
                p->state.V[0], p->state.V[1], p->state.V[2],
                p->state.diam, p->state.temp, p->flow_rate, p->state.time,
                p->user[0], name);
#else
        par_fprintf(fp,
                "((%10.6g    %10.6g    %10.6g    %10.6g    %10.6g    %10.6g    "
                "%10.6g    %10.6g    %10.6g    %10.6g %10.6g %10.6g    %10.6g %10.6g) %s)\n",
                x0,y00,z0,
                p->state.pos[0], p->state.pos[1], p->state.pos[2],
                p->state.V[0], p->state.V[1], p->state.V[2],
                p->state.diam, p->state.temp, p->flow_rate, p->state.time,
                p->user[0], name);
#endif
}
}
```

3. Convex function, Jensen's inequality

In mathematics, a real-valued function is said to be convex if the line segment between any two points on the graph of the function lies above or on the graph. For a real convex function (φ), if numbers $x_1, x_2, \cdots, x_n$ are in its domain and of positive weight (w_i), Jensen's inequality can be stated as:

$$\varphi\left(\frac{\sum w_i x_i}{\sum w_i}\right) \leq \frac{\sum w_i \cdot \varphi(x_i)}{\sum w_i}$$

in which equality holds if and only if $x_1 = x_2 = \cdots = x_n$.

In the present study, Eq. 8

$$C_i = C_0 \cdot \exp(-k \cdot D_i)$$

where C_i is a convex function of D_i, and w_i ($\sum w_i = 1$) is the mass-flux weight, then the mass-flux weight averaged concentration calculated by Eq. 9 has a minimum value:

$$\bar{C} = \sum(w_i C_0 \exp(-kD_i)) \geq C_0 \exp(-k \cdot \sum w_i D_i) = C_{min}$$

Equality holds if and only if $D_1 = D_2 = \cdots = D_n$, in other words, no variation in VUV dose among the particles.

Giving the same decrement ratio (*m*, from 0 to 1) in vacuum ultraviolet (VUV) dose to all of the particles, then

$$D_i' = (1 - m) \cdot D_i$$

$$\bar{D}' = (1 - m) \cdot \bar{D}$$

$$\ln\left(\frac{C'_{min}}{C_0}\right) = -k \cdot \sum w_i D_i' = -k \cdot \bar{D}' = -k \cdot (1 - m) \cdot \bar{D} > -k \cdot \bar{D}$$

$$\ln\left(\frac{\bar{C}'}{C_0}\right) = \ln\left(\sum\left(w_i \cdot \exp\left(-kD_i'\right)\right)\right) = \ln\left(\sum(w_i \cdot \exp(-k(1 - m) \cdot D_i))\right)$$

$$> \ln(\sum(w_i \cdot \exp(-k \cdot D_i)))$$

$$\eta' = \frac{\ln\left(\frac{\bar{C}'}{C_0}\right)}{\ln\left(\frac{C'_{min}}{C_0}\right)} = -\frac{\ln(\sum(w_i \cdot \exp(-k(1-m) \cdot D_i)))}{k \cdot (1-m) \cdot \bar{D}}$$

Since $0 < \eta, \eta' < 1$, $\ln\left(\frac{\bar{C}'}{C_0}\right) < 0$

$$\eta' = -\frac{\ln(\sum(w_i \cdot \exp(-k(1 - m) \cdot D_i)))}{k \cdot (1 - m) \cdot \bar{D}} > -\frac{\ln(\sum(w_i \cdot \exp(-k(1 - m) \cdot D_i)))}{k \cdot \bar{D}}$$

$$> -\frac{\ln(\sum(w_i \cdot \exp(-k \cdot D_i)))}{k \cdot \bar{D}} = \eta$$

As a result, reducing the VUV dose to all of the particles by the same ratio leads to an increase in radiation efficiency.